Università degli Studi di Cagliari
Dipartimento di Fisica

PhD Degree in Physics
Cycle: XXXI

The ReD experiment in DarkSide's Program: nuclear recoils for Dark Matter studies

Scientific Disciplinary Sector: Fis/01

PhD Candidate Mauro Caravati

Coordinator of the PhD program Prof Paolo Ruggerone

Supervisors Dr Corrado Cicaló
Prof Giuliana Fiorillo

Final exam. Academic Year 2017-2018.
Thesis defence: January-February 2019 Session

INTRODUCTION

> Il principio dominante nel cosmo è la cecità. Proprio essa rende possibile la presenza, l'una accanto all'altra, di tante cose che non potrebbero coesistere se si potessero vedere reciprocamente.
>
> ---
>
> *Auto da fé* - Elias Canetti

While there is strong astrophysical and cosmological evidence for dark matter (DM), its precise nature is one of the most significant open questions in modern physics. Weakly interacting massive particles (WIMPs) are a particularly compelling class of dark matter candidates with masses up to about 10 TeV and couplings to ordinary matter at the weak scale. Direct detection experiments are aiming to observe the low energy ($<$150 keV) scattering of dark matter off normal matter. No conclusive signal has yet been observed.

The DarkSide Program aims at direct WIMP dark matter detection using dual-phase (liquid and vapor) Liquid Argon Time Projection Chambers (LAr TPCs). The program is staged with detectors of increasing mass and sensibility, installed at Laboratori Nazionali del Gran Sasso (LNGS) in Italy. Inside the DarkSide program the DarkSide-50 experiment is currently operating with an active mass of about 50 kg of Underground Argon (UAr), which is greatly reduced in radioactive ^{39}Ar. From the analysis of DarkSide-50 data, the DarkSide Collaboration, among others, has published background-free WIMP search results, that is less than 0.1 background events expected and no one observed in the

search region. This leads to the expectation that a result free from instrumental background could be obtained from a much larger exposure with a multi-tonne detector. The next step in this program is then the DarkSide-20k experiment, with a fiducial mass of 20 t for a total exposure of 100 t yr to be accumulated in a run of 5 yr. With this exposure and beyond, at which the onset of ν-induced nuclear recoils have to be considered, sensitivity to the direction of the nuclear recoils originating from WIMP scatter would be a very highly desirable capability for a direct dark matter detection experiment.

Inside DarkSide Program the Recoil Directionality (ReD) experiment first aims to reveal directionality signature in energy nuclear recoils of the order of expected WIMP-Ar scattering recoils. Also, a more systematic study on nuclear recoil is needed down to very low energy recoil ($\sim \mathcal{O}(1\,\mathrm{keV_{NR}})$). In order to have directional experiment with controlled recoil energy, it is necessary the use of low energy and as mono-energetic as possible neutrons in a closed kinematics approach. To this purpose ReD is now installed (at the moment of writing even running) at Laboratori Nazionali del Sud (LNS) in Catania, Italy, where neutrons are produced via $p(^7\mathrm{Li}, n)^7\mathrm{Be}$ reaction using their Tandem accelerator. Moreover, in the ReD experiment more potential DarkSide-20k future solutions are implemented, so that ReD is also part of DarkSide-20k R&D specific program.

In the first part of this work, after an introduction on the importance to study and observe Dark Matter to explain some cosmological phenomena that vice versa would remain without explanation, a description on LAr TPCs operating principle is delineated, together with a short description on the DarkSide program. Particular attention is reserved to argon physics in those parts that have impact on TPCs technology or potentially on ReD experimental results.

ReD is an ongoing experiment, more in the commissioning than in the data taking phase. Or, as we could better say, we can say in the transition phase between the two phases. Like in each R&D activity on small experiments, I had the opportunity to face almost every aspect of this research, from alternative experimental setup studies, to the hardware, going through Monte Carlo simulations and finally to the data analysis. In this thesis, I decided to focus the attention on the last experimental configuration used, although some details on the alternative ones are also reported. Therefore, in the second part of this work I describe in detail the ReD experiment and all its constituents in the LNS configuration. Finally, in the last chapter, I report some preliminary results on the data taken during the first two technical beam times, in June and July, 2018. At the time of writing (September, 2018) a third data taking is ongoing, and the results will be soon available.

CONTENTS

LIST OF FIGURES

LIST OF TABLES

1. THE WIMP SOLUTION TO THE DARK MATTER'S PUZZLE

The Dark Matter (DM) puzzle can be traced back to at least the 1930s, when the astronomer Fritz Zwicky found the velocity dispersion of members of the Coma cluster of galaxies to be so high that, to keep the system stable, the average mass density in the system would have to be much higher than that deduced from observed visible matter; he attributed this behavior to the presence of *dark matter* [1]. Early candidates for dark matter were baryonic in form. Non-luminous stellar remnants such as white dwarfs and neutron stars, often referred to as MAssive Compact Halo Objects (MACHOs), were proposed to populate galactic halos [2]. These objects can just be searched for via microlensing observations (see section 1.1.2), where the dark object passes in the line of sight of a distant luminous background object, inducing a transient change in brightness due to gravitational lensing. The microlensing results indicate that MACHOs can account for no more than 20% of what would be needed to account for all dark matter in the galactic halo [3].

Today the existence of Dark Matter is widely accepted and confirmed also on the cosmological scale. At the moment the most precise measurement of the Cosmic Microwave Background (CMB), combined with the results from large-scale structure observations, indicates that dark matter and dark energy contribute respectively to 26.2% and 68.9% of the mass/energy density of the Universe leaving

only 4.9% to the ordinary matter [4, Planck 2018 results][1].

Among a wide range of possible theories and dark matter candidates one of the most popular hypothesis is that the galactic halo could be permeated of so called Weakly Interactive Massive Particles (WIMP), that broadly speaking is a new -yet undiscovered- big-bang relic particle that interacts via gravity and any other force, possibly also not included in the Standard Model (SM), which is as weak or weaker than the weak nuclear SM force. WIMPs could in principle be detected through their collisions with ordinary nuclei in an instrumented target, producing low-energy nuclear recoils with very low interaction rates [7]. Then to directly detect WIMPs, target masses up to several tons may be required, and ultra-low background must be achieved by a combination of methods, including cosmic ray suppression by locating the experiments deep underground, selection of materials for low radioactivity, and detector technologies that can reject residual radioactive backgrounds in favor of nuclear recoil events.

1.1 The Dark Matter's puzzle

Although dark matter has not been directly detected, its existence is supported by macroscopic evidence from its gravitational influence on luminous astrophysical matter; these evidences can be classified into three different classes: Kinematics of Clusters and Galaxies - Gravitational Lensing - Cosmological evidence.

[1] The possibility that observations can be explained by a modified law of gravity (MOdified Newtonian Dynamics - MOND) was first considered by Milgrom [5], however relativistic extensions of MOND still do not reproduce the features of large scale structure, CMB and more importantly the Bullet Cluster behaviour [sec. 1.1.2] with the same success as ΛCDM [6] [sec. 1.1.3].

1.1.1 Kinematics of Clusters and Galaxies

The first evidence for a missing matter component in the universe comes from Fritz Zwicky[8], who in the 1930s, calculated the velocity dispersion of galaxies in the Coma cluster by measuring their red shift and applied the virial theorem to estimate the average mass of each galaxy. Combining his results with average luminosity measurements gave a mass-to-luminosity ratio M/L (normalized to solar mass and solar luminosity) several hundred times larger than the expectation of order 1. Despite the initial skepticism, further studies revealed that the Coma cluster was not unusual.

In the 1970s Vera Rubin *et al.* [9] firmly established the need for a dark matter component when she measured the rotation curves of a host of galaxies. Rubin measured rotation curves by selecting edge-on galaxies and comparing the redshift of the 21 cm line from stars on opposite sides (approaching and receding). From Newtonian dynamics, one expects that the velocity of stars and gas in circular orbit should follow $v(r) \propto \sqrt{M(r)/r}$, where $M(r)$ is the mass internal to radius r from the galactic center. Beyond the optical disk, where the bulk of the luminous matter of the galaxy resides, $v(r)$ should have a $1/\sqrt{r}$ dependence.

Instead Rubin found that the rotation curves were constant well beyond the optical disk for many galaxies, suggesting a spherical dark matter halo with mass density $\rho(r) \propto 1/r^2$, Fig 1.1. The density will have to fall off faster at some point in order to keep the total mass of the galaxy finite, and the extent of the dark matter halo is still not well known, but the constant profile of rotation curves remains among the strongest evidence for the existence of dark matter.

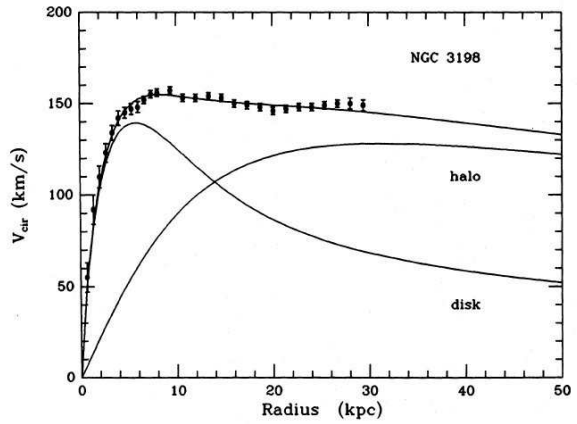

Fig. 1.1: Rotation curve for galaxy NGC 3198 with the individual contributions from luminous components and dark matter halo. From Ref. [10].

1.1.2 Gravitational Lensing

Gravitational lensing provides another powerful tool for establishing the existence of dark matter. One of the consequences of General Relativity is that massive objects, such as galaxies or galaxy clusters, distort their surrounding space-time. In gravitational lensing, light from a distant source object behind the massive object is bent, or lensed, on its way to Earth. The image of the source object can be multiplied, amplified, and distorted into arcs or rings. Survey telescopes have observed lensed objects around numerous galaxies and galaxy clusters and the inferred masses have consistently indicated that the M/L values are large, 10 to 20 for galaxies and 100 to 300 for galaxy clusters [11] and require the existence of large amounts of matter in non luminous form.

Lensing has also been used to study the properties of dark matter itself, meaning that it cannot be accounted for by ordinary baryonic matter. This can be achieved observing the so-called Bullet Cluster (1E0657−558), a system of two galaxy clusters that recently (on cosmological time-scale) collided [12]. An X-ray and optical (visible) light picture of such an event is shown in Fig. 1.2. The major-

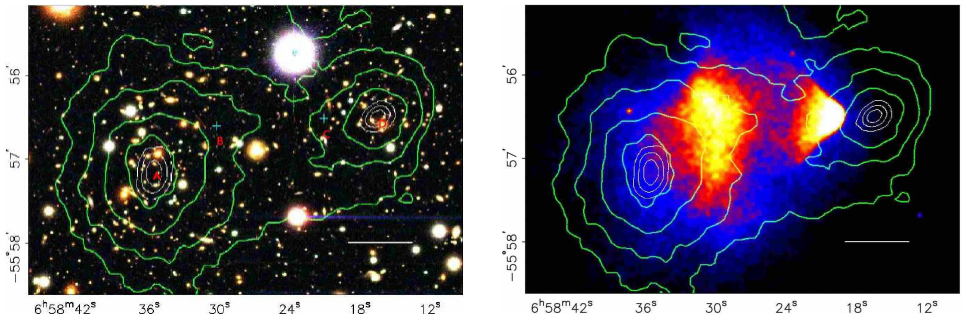

Fig. 1.2: Left: A image from the Magellan images of the merging cluster 1E0657−558 (white bar 200 kpc at the distance of the cluster). *Righ*: A 500 ks Chandra-X image. Green contours the weak lensing reconstruction. From Ref. [13]

ity of the light coming from the Bullet Cluster comes from hot X-ray emitting gas: during the collision the baryonic gas particles interact with each other through both gravity and electrostatic forces, slowing and shocking one another. The dark matter particles, however, only interact through gravity (and/or through a weak force) and can pass through each other unimpeded by electrostatic interactions. So the X-ray emitting gas lags behind the dark matter as the two clusters escape the collision, causing the observed offset in the mass distribution which is a very strong indication for the presence of a far more weakly interacting form of matter than baryonic matter.

1.1.3 Cosmological evidence

Dark matter evidences are such that the most recognized model that summarizes our understanding about the origin of the Universe -the Lambda Cold Dark Matter (ΛCDM) model- includes dark matter as a key component, where Λ refers to the cosmological constant (i.e. the energy density or Dark Energy of the vacuum) and "Cold Dark Matter" stands for slowly moving particles that account for the variety of cosmological observations that imply the presence of *missing mass*. Developed in the late 1990s, this model is the simplest parametrization of the Big Bang cosmological model that is broadly consistent with several observations, namely

the existence and properties of the Cosmic Microwave Background (CMB), the large-scale structure in the distribution of galaxies, the abundances of hydrogen (including deuterium), helium, and lithium and the accelerating expansion of the universe observed in the light from distant galaxies and supernovae.

According to this model, the structures that emerged in the early Universe are caused by the clustering of a non-interacting, slow moving and yet undetected matter component [14], usually referred to as Cold Dark Matter. The fact that DM interacts only gravitationally (or very weakly) means that it begins to collapse gravitationally earlier in cosmic time than baryonic matter. After decoupling, baryons then fall into the gravitational wells produced by the infalling DM structures. Without DM, the baryonic matter in the Universe could not have had enough time to collapse to form the range of gravitationally bound structures we see today [15, 14].

A particularly sensitive probe for determining the dark matter contribution to the energy budget of the Universe is the measurement of the temperature anisotropies of CMB photons (the electromagnetic radiation left over from an early stage of the universe in Big Bang cosmology),observed today with a mean temperature of $2.726 \pm 0.010\,\mathrm{K}$. While the CMB is mostly isotropic, showing that the universe is largely homogeneous, small anisotropies are present due almost entirely to the temperature fluctuations in the early universe that were caused by the under- and over-densities in different regions as particles began to freeze out at different times. The intensity and size of these fluctuations depend entirely on the different components and species present at the time, making the CMB sensitive to the amount of dark matter present in the early universe. The Planck experiment measured the angular power spectrum of these CMB temperature

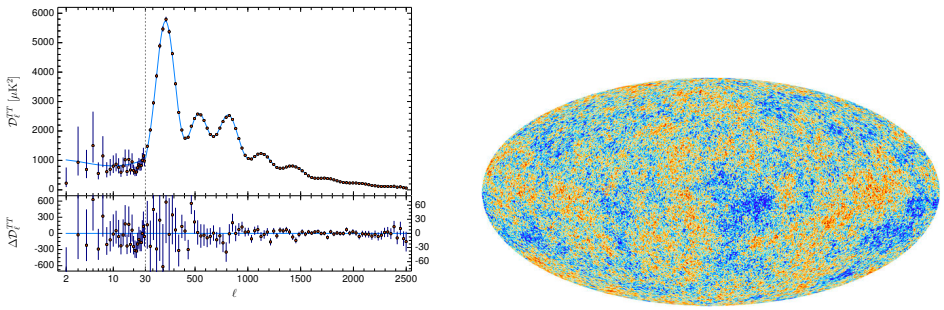

Fig. 1.3: Left: Angular power spectrum of CMB temperature anisotropies as measured by the Planck satellite (2018). Data are shown as blue points with the best fit ΛCDM cosmological model shown as a red line. *Right:* Cosmic Microwave Background as observed by the Planck satellite. Figures from Ref. [4] and references therein.

anisotropies: the amplitude of the power spectrum at various values of l, the angular size (π/l) of a given spherical harmonic, gives a quantitative measurement of the anisotropies in the CMB, which allows to determine the relative abundance of different kinds of particles in the universe after the freeze out, as well as many other properties (figure 1.3 shows the last -2018- results of these measurements, as well as the best fit using the six parameters ΛCDM model while in Tab. 1.1 the obtained Cosmological parameters - see Ref. [4, Planck 2018 results]).

Parameter	68% limits
$H_0[\,\mathrm{km\ s^{-1}Mpc^{-1}}]$	67.66 ± 0.42
Ω_Λ	0.6889 ± 0.0056
Ω_m	0.3111 ± 0.0056
$\Omega_b h^2$	0.02242 ± 0.00014
$\Omega_c h^2$	0.11933 ± 0.00091

Tab. 1.1: Density parameters (Ω_-) of dark energy/cosmological constant (Λ), baryonic (b) and cold dark matter (c) components with Hubble parameter as $h = H_0/(100\,\mathrm{km\ s^{-1}Mpc^{-1}})$; Planck Collaboration (2018 results) [4, Table 2.].

The success of the ΛCDM paradigm is also due to the results coming from so-called N-body simulations, computer simulations that involve a large number of particles interacting according to basic physical laws and are used to track the evolution of structure in the Universe: millions of particles are configured accord-

ing to an initial density distribution and are allowed to interact following the laws of gravity. The simulation can track the growth of structures in the model system. Depending on the initial density distribution and cosmological parameters selected, different structures appear at different stages of evolution. Consistent picture has emerged from several N-body simulations: galaxies distribution observed in large scale structures matches that predicted by N-body simulations over a huge range of distance scales [16]. In addition, simulations have begun to accurately reproduce the observed populations of elliptical and spiral galaxies [17], as well as obtaining Milky Way-like simulated galaxies [18]. This ability of simulations containing DM to reproduce structures observed in the Universe is a further strong evidence in support of the DM paradigm.

While not a measurement of the dark matter density, Big Bang Nucleosynthesis (BBN) provides further incontrovertible evidence that baryonic matter constitutes only $\sim 5\%$ of the Universe. BBN describes the production of light nuclei in the first few minutes after the Big Bang. By solving a set of coupled Boltzmann equations describing the nuclear reactions of protons, neutrons and light nuclei, we can obtain the primordial abundances of these light nuclei and compare them with the found values [19]. Significantly, these abundances depend strongly on the baryon to photon ratio η and therefore the total baryon density. Fits to data lead to the result $\Omega_b h^2 = 0.017 - 0.024$ [20], independent of the value obtained from CMB measurements (Table 1.1). Thus, the baryonic matter can make up only a fraction of the total matter density of the Universe. This provides further evidence that particle dark matter must consist of some non-baryonic particle.

The results of BBN are also very sensitive to light new species, which can alter the number of relativistic degrees of freedom in the early Universe and therefore

affect the expansion rate. These include, for example, gravitinos [21] and right-handed neutrinos [22]. BBN therefore provides strong constraints on models in which these particles play the role of DM. In addition, the decay of dark matter particles into electromagnetic or hadronic showers during nucleosynthesis can drastically change the primordial abundances of the light elements. BBN can therefore be used to constrain models in which dark matter decays promptly (or in which dark matter is produced by the decays of heavier particles) [23].

1.2 The WIMP solution

The most popular class of dark matter candidates is the Weakly Interacting Massive Particle (χ). They are just as the name describes: massive particles, typically in the GeV to TeV range, that interact with ordinary matter at the weak scale or below. WIMPs are particularly interesting because they arise naturally in a variety of beyond-Standard-Model theories and they naturally have the correct relic density to account for all the dark matter in the universe.

These particles would have been produced like other particles in thermal equilibrium in the Big Bang, and their abundance today would be determined by their annihilation cross-section to SM quark and lepton pairs, e.g. $\chi\overline{\chi} \to q\overline{q}$. The standard scenario for the production of dark matter is referred to as thermal freeze-out [14], in which scenario DM particles remain in kinetic and chemical equilibrium with SM particles in the very early Universe through scattering and annihilation processes. Their number density n follows a Maxwell-Boltzmann distribution

$$n \sim (M_\chi/T)^{3/2} \exp(-M_\chi/T)\,, \tag{1.1}$$

for a particle mass M_χ and temperature T. As the Universe expands the particles

become diluted, reducing the interaction rate until eventually the DM particles become decoupled from the SM particles and are "frozen-out". They are then left with the abundance they had when they decoupled, which is further diluted by the expansion of the Universe to become the abundance we have today. The exact relic abundance depends on $\langle \sigma_{\rm ann} v \rangle$, the average annihilation cross section of the DM particles weighted by the DM relative speed. The resulting relic abundance for GeV-scale DM is given approximately by [14]:

$$\Omega_c h^2 \approx \frac{3 \times 10^{-27}\ \mathrm{cm}^3\ \mathrm{s}^{-1}}{\langle \sigma_{\rm ann} v \rangle}\,. \tag{1.2}$$

This leads to a canonical value of around $\langle \sigma_{\rm ann} v \rangle \approx 3 \times 10^{-26}\ \mathrm{cm}^3\ \mathrm{s}^{-1}$ for the annihilation cross section. This coincides well with the value expected for particles with SM weak-scale interactions, leading to refer to this argument as the *WIMP miracle*. So Big Bang relic population of weakly interacting particles, with mass in the $10 - 10^3$ GeV range, would naturally have the correct present density.

1.2.1 WIMPs's detection strategies

We observe DM through its gravitational effects, but how can we search for WIMPs other than through their gravitational interactions? There are generally three different approaches: collider searches, indirect detection, and direct detection [Fig. 1.4]. In collider searches, one tries to produce dark matter by col-

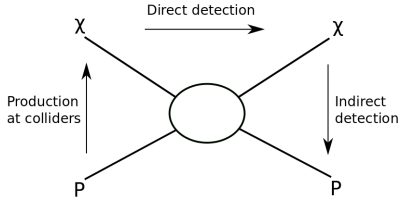

Fig. 1.4: Schematic diagram of different strategies to detect dark matter particles χ (P particle of ordinary matter).

liding Standard Model particles together at very high energy in such accelerators as the Large Hadron Collider (LHC). Dark matter will be produced in particle-antiparticle pairs which will escape detection. The signature for dark matter in collider searches is missing energy/momentum.

In indirect detection, one looks for Standard Model particles as products of WIMP annihilation. The exact annihilation process depends on the specifics of the dark matter model, but in many theories WIMPs are Majorana particles and will therefore annihilate with each other. Frequently, experiments look for annihilation products such as gamma rays, neutrinos, and antimatter. The signature for dark matter in indirect detection is an excess of Standard Model particles.

The DarkSide Program is based on direct detection, so below a dedicate section on this topic.

1.3 WIMPs Direct Detection

The idea that particle DM may be observed in terrestrial detectors via direct detection was first proposed by Goodman and Witten in 1985 [24] and by Drukier, Freese and Spergel in 1986 [25]: if DM can interact with particles of the SM, the flux and the interaction cross section of DM from the halo of the Milky Way may be large enough to cause measurable scattering from nuclei. So in direct detection experiments the aim is to detect -or set limits on -nuclear recoils produced by the collisions between WIMPs and detector target nuclei [2].

In the standard hypothesis the WIMP-nucleus interaction is modeled as a non relativistic elastic scatter, so the energy E_R of the recoiling nucleus of mass m_A

[2] Recently some experiments are looking for WIMP interactions with electrons as target too. DarkSide Collaboration has just published a work on constraints on sub-GeV dark-matter particles, looking in recoil spectra for dark matter-electron scattering in argon. Ref.[26].

from a WIMP of mass m_χ is given by:

$$E_R = 4\frac{m_\chi m_A}{(m_\chi + m_A)^2}\frac{m_\chi v^2}{2}\cos^2\theta_r \tag{1.3}$$

where v is the speed of the WIMP relative to the nucleus and θ_r is the nucleus recoiling angle in the laboratory frame with respect to the incident direction of the WIMP[3].

It is immediate to see that for WIMP mass in $(1-10^3)$ GeV range, and velocity $v \sim 10^{-3}$ c (expected mean WIMP-velocity), the recoil energy is in the $(10^{-2} - 10^2)$ keV range ($m_A \sim 10^2$ GeV). These are relatively low energy deposits that WIMP direct detection experiments, which are based on ionization, scintillation, low temperature phonon techniques (see sec. 1.3.2), must be able to observe.

1.3.1 Event rate

Due to the expected low cross section for such interactions, the predicted rate in direct detection is very small and depends on several factors: the local dark matter halo density and velocity distribution, the WIMP mass, and obviously the cross section on the target nuclei. The differential recoil rate per unit detector mass, typically given in units of counts/kg/day/keV, can be written as [27]:

$$\frac{dR}{dE}(E,t) = \frac{\rho_0}{m_\chi m_A}\int v f(\mathbf{v},t)\frac{d\sigma}{dE}(E,v)\ \mathrm{d}^3v, \tag{1.5}$$

where $\frac{d\sigma}{dE}(E,v)$ is the differential cross-section, ρ_0 is the local dark matter density and $f(\mathbf{v},t)$ accounts for the WIMP velocity distribution in the detector reference

[3] It is usually reported in terms of the WIMP's scattering angle in the center of mass frame $\phi*$, where eq. 1.3 becomes

$$E_R = 4\frac{m_\chi m_A}{(m_\chi + m_A)^2}\frac{m_\chi v^2}{2}\frac{(1-\cos\phi^*)}{2} \tag{1.4}$$

frame, which is time dependent due to the revolution of the Earth around the Sun; this modulation is expected to be a percent-level effect (see below) and we consider for now only the time averaged distribution. The lower limit of the integration over WIMP speeds is given by the minimum WIMP speed which can cause a recoil of energy E_R:, from eq. 1.3: $v_{\min} = \sqrt{(m_A E_R)/(2\mu^2_{(\chi;A)})}$ [4]. The upper limit is formally infinite, however it must be considered the local escape speed $v_{\rm esc}$, the maximum speed in the Galactic rest frame for WIMPs which are gravitationally bound to the Milky Way.

In the Standard Halo Model (SHM) local dark matter density is conventionally set at $\rho_0 \simeq 0.3\,{\rm GeV/cm^3}$, however depending on the profile model used for the halo, a density range $(0.2 - 0.6)\,{\rm GeV/cm^3}$ can be derived (see Refs. [28, 29] and references therein). Moreover in the SHM WIMPs are considered to be an isothermal sphere with an isotropic, Maxwellian velocity distribution

$$f(\mathbf{v}) = \frac{1}{(2\pi\sigma^2)^{3/2}} \cdot \exp\left(- \frac{|\mathbf{v}|^2}{2\sigma^2}\right), \tag{1.6}$$

truncated at velocities exceeding $v_{\rm esc}$. Here, the dispersion velocity σ is related to the circular speed, the sun's speed around the center of the Milky Way v_c, via $\sigma = \sqrt{3/2}\, v_c$. A standard value of $v_c = 220\,{\rm km/s}$ is used for the local circular speed. This value results from an average of values found in different analyses [30]. More recent studies using additional data and/or different methods, find velocities ranging from $(200 \pm 20)\,{\rm km/s}$ to $(279 \pm 33)\,{\rm km/s}$ [31]. The escape velocity defines a cut-off in the description of the standard halo profile. The commonly used value of 544 km/s is the likelihood median calculated using data from the RAVE

[4] In general $\mu_{(1;2)}$ refers to the reduced mass among m_1 and m_2: in this case $\mu_{(\chi;A)} := \frac{m_\chi m_A}{(m_\chi + m_A)}$.

survey [32]. The 90% confidence interval contains velocities from 498 km/s to 608 km/s.

These large ranges of possible values for the dark matter density, circular speed and escape velocity illustrate that the uncertainties in the halo modelling are significant [29]. Nevertheless direct detection experiments, for reasons of simplicity and uniformity in confronting different experimental exclusion curves, generally use the common assumption of an isotropic Maxwell-Boltzmann distribution, using values for astrophysical parameters as introduced above.

Accordingly the differential recoil rate eq. 1.5 can be written as (Ref. [7]):

$$\frac{dR}{dE_R} = \frac{\sigma(q)\rho_\chi}{2\mu^2_{(\chi;A)} m_\chi} \int_{v_{min}}^{v_{esc}} \frac{f(v)}{v} dv \tag{1.7}$$

where $q = \sqrt{2m_A E_R}$ is the nuclear recoil momentum and $\sigma(q)$ is the WIMP-nucleus interaction cross section. The cross section can be factored as

$$\sigma(q) = \sigma_0 F^2(q) \tag{1.8}$$

where σ_0 is the cross section at zero momentum transfer and $F(q)$ is the nuclear form factor, which accounts for the finite size of the target nucleus, depends principally on the nuclear radius and recoil energy, and may differ for spin-dependent and spin-independent interactions. The cross section depends on the number of protons and neutrons in the nucleus [33]:

$$\sigma_0 = \sigma_N \left(Z \frac{f_p}{f_n} + (A - Z) \right)^2 \frac{\mu^2_{(\chi;A)}}{\mu^2_{(\chi;N)}}, \tag{1.9}$$

where σ_N is the WIMP-Nucleon cross section, Z is the number of protons, A is

the atomic mass number, f_p and f_n are the WIMP couplings to the proton and neutron, and $\mu_{(\chi;N)}$ is the WIMP-Nucleon reduced mass (treating the neutron and proton masses as equal). Furthermore it is typical to assume that WIMP couplings to proton and neutrons are the same[5], so taking $f_p = f_n$ and putting together equations 1.7, 1.8, 1.9 we finally obtain

$$\frac{dR}{dE_R} = \frac{\sigma_N \rho_\chi}{2\mu_N^2 m_\chi} A^2 F^2(q) \int_{v_{min}=\sqrt{(m_A E_R)/(2\mu^2_{(\chi;A)})}}^{v_{esc}} \frac{f(v)}{v} dv \tag{1.10}$$

Eqn. 1.10 has an A^2 dependence which means, neglecting dependence on the nuclear form factor $F(q)$, that heavier elements can expect higher event rates, at least in the low-recoil-energy regime where scattering is coherent.

According to Lewin and Smith [7], the velocity integral can be worked out and eq. 1.10 can be approximated by:

$$\frac{dR}{dE_R}(E_R) \approx \left(\frac{dR}{dE}\right)_0 F^2(E_R) \exp\left(-\frac{E_R}{E_c}\right) \tag{1.11}$$

where $\left(\frac{dR}{dE}\right)_0$ is the event rate at zero momentum transfer and E_c is a constant parameterizing a characteristic energy scale which depends on the dark matter mass and target nucleus. Hence, the signal is dominated at low recoil energies by the exponential function. The most common approach in direct detection experiments is the attempt to measure the exponential decreasing energy dependence of dark matter interactions. Figure 1.5 shows scattering rates above detection threshold for several noble gas elements and for germanium, a competitive cryogenic bolometer material.

Calculations must take into account the weak nuclear form factor, which de-

[5] i.e. isospin conservation - see Ref. [34] for a recent isospin-violating dark matter study.

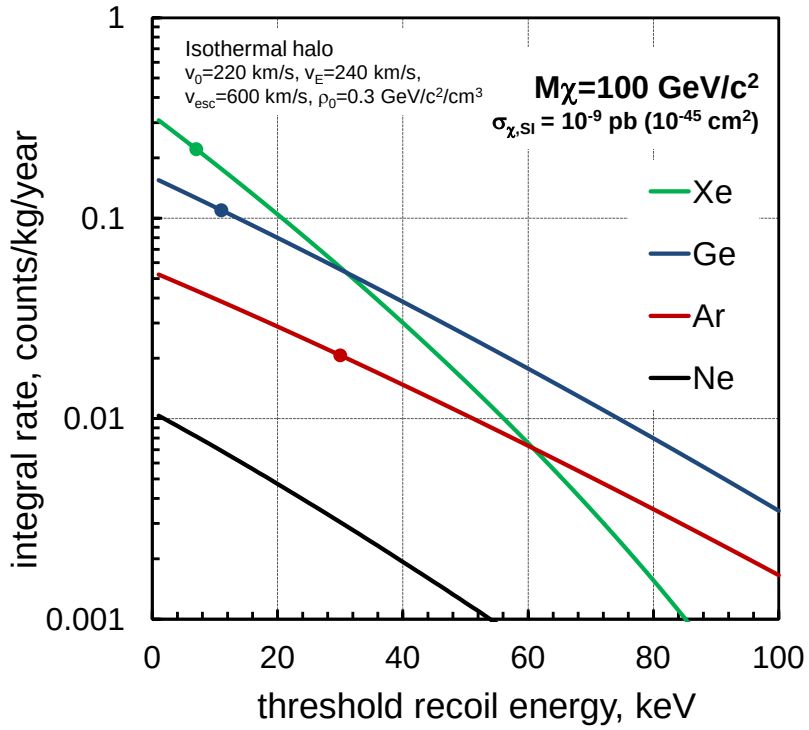

Fig. 1.5: Predicted integral spectra for WIMP elastic scattering for Xe, Ge, Ar and Ne (in order of decreasing rate at zero threshold). Plot assume perfect energy resolution. Dark matter rates are for a 100 GeV/c^2 WIMP with 10^{-45}cm^2 interaction cross section per nucleon; the markers indicate typical WIMP-search thresholds for each technology (From [35]).

creases with transferred momentum much more rapidly for xenon than for argon. The Xe form factor drops practically to zero for recoil energies of 100 keV, while it is still ≈0.5 for argon recoils of that energy; this behavior is apparent in Figure 1.5, where the full calculations following Lewin and Smith [7] are presented. Such low scattering rates justify why dark matter search experiments require large detector masses, with tonne-scale experiments being built at present. Moreover rates mentioned above are *scattering* rates. Actual *detection* rates will also depend on detector efficiency (and energy resolution) as a function of recoil energy.

A possible different dark matter signature is the so-called "annual modulation". As a consequence of the Earth rotation around the Sun, the speed of the dark matter particles in the Milky Way halo relative to the Earth is largest around

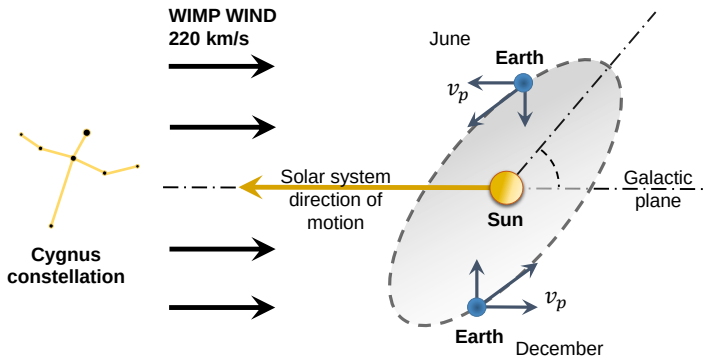

Fig. 1.6: Schematic diagram to explain the annual modulation of dark matter direct detection signal.

June 2nd and smallest in December, Fig. 1.6. Consequently, the amount of particles able to produce nuclear recoils above the detectors energy threshold is also largest in June [36]. As the amplitude of the variation is expected to be small, the temporal variation of the differential event rate can be written, following Freese, Lisanti, and Savage [37], as:

$$\begin{cases} \frac{dR}{dE}(E,t) \approx S_0(E) + S_m(E) \cdot \cos\left(\frac{2\pi(t-t_0)}{T}\right) \\ S_m(E) \ll S_0(E) \end{cases} \tag{1.12}$$

where t_0 is the phase which is expected at about 150 days and T is the expected period of one year. The time-averaged event rate is denoted by S_0, whereas the modulation amplitude is given by S_m. A rate modulation would, in principle, enhance the ability to discriminate against background and help to confirm a dark matter detection. The DAMA/LIBRA experiment [38] operating at the Laboratori Nazionali del Gran Sasso (LNGS) laboratory in Italy, for two decades

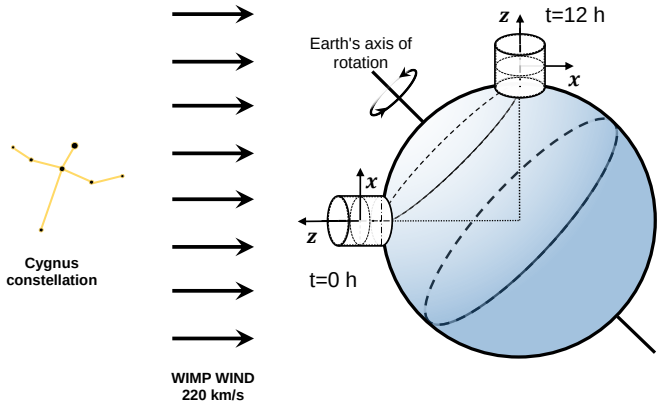

Fig. 1.7: Schematic diagram that shows the change in orientation of the coordinate axes attached to a terrestrial dark matter detection laboratory due to the rotation of Earth around its own axis.

has been reporting to see an annually modulated DM-like signal, which currently has a significance at the level of 9.5σ in the energy region (1-6) keV, up to 12.9σ in the energy region (2-6) keV [39].

Directionality is another dark-matter signature which can be employed for detection as the direction of the nuclear recoils resulting from WIMP interactions has a strong angular dependence [40]. This dependence can be seen in the differential rate equation when it is explicitly written as a function of the angle γ, defined by the direction of the nuclear recoil relative to the mean direction of the solar motion

$$\frac{dR}{dE\ d\cos\gamma} \propto \exp\left[\frac{-[(v_E + v_\odot)\cos\gamma - v_{min}]^2}{v_c^2}\right]. \tag{1.13}$$

In equation 1.13, v_E represents the Earth's motion, $v_\odot$ the velocity of the Sun around the galactic centre and v_c the halo circular velocity $v_c = \sqrt{3/2}v_\odot$. The integrated rate of events scattering in the forward direction will, therefore, exceed the rate for backwards scattering events by an order of magnitude [40]. An oscillation of the mean direction of recoils over a sidereal day is also expected due to

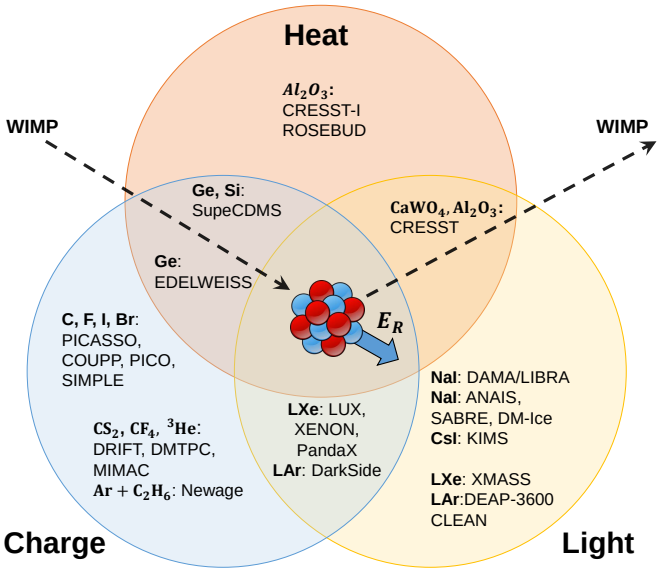

Fig. 1.8: Direct dark matter detection experiments organised by energy deposition channel(s) used.

the rotation of the Earth and if the detector is placed at an appropriate latitude, Fig 1.7.

This directional signature allows to discriminate potential backgrounds [41]. A detector able to determine the direction of the WIMP-induced nuclear recoil would provide a powerful tool to confirm the measurement of dark matter particles. In this context the Recoil Directionally -ReD- experiment founded its motivations.

1.3.2 Detection methods

Scatterings of DM particles off nuclei can be detected via produced light (scintillation photons from excitation and later de-excitation of nuclei), charge (ionization of atoms in a target material) or heat (phonons in crystal detectors); see Fig. 1.8 for a summary scheme.

In direct detection methods electron recoils constitute the prime background of an experiment and can come from e.g.γ-radiation from natural radioactivity or β-decays, that take place in the detector surrounding materials, on its surface or even

inside the detector. Using one or a combination of two above mentioned techniques is now often employed to disentangle potential often employed to disentangle nuclear recoils (potential generated by WIMPs) from background electron-like recoils. This is possible due to usually different signals behaviors between nuclear recoils and electron-like recoils.

Other sources of background, e.g.neutrons or α-decays, may produce nuclear recoils so mimic the WIMP signal. Therefore they need to be either screened out or rejected at the level of signal analysis (e.g. for α-decays from wall materials using cuts in interacting positions, as in dual-phase TPC technology). As pointed out by Freedman [42] a particularly challenging type of such a background that will be very important for future detectors, especially for DM mass below 10 GeV, comes from coherent elastic neutrino-nucleus scatterings, the so-called coherent neutrino background [43, 44].

Depending on the choice of signal detection technique a variety of target materials can be employed in DD searches. Light signal from DM-nucleus scattering can be collected, e.g., by using scintillating crystals. Crystal scintillator experiments such as DAMA/LIBRA [38, 45] use crystals of Thallium-doped Sodium Iodide, NaI(Tl), while KIMS [46] uses Thallium-doped Cesium Iodide, CsI(Tl), as the detector material. In the case of DAMA/LIBRA, electron-nuclear recoil discrimination is not employed. In other cases, such as NAIAD [47], pulse shape discrimination has been used to distinguish nuclear and electron recoils.

Cryogenic experiments, such as CDMS [49], CRESST [50], CoGeNT [51, 52] and EDELWEISS [53], use cryogenic crystals of materials such as germanium or silicon as target materials. When a WIMP recoils from a target nucleus, phonons are generated in the crystal along with ionization signal. Noble liquid experiments

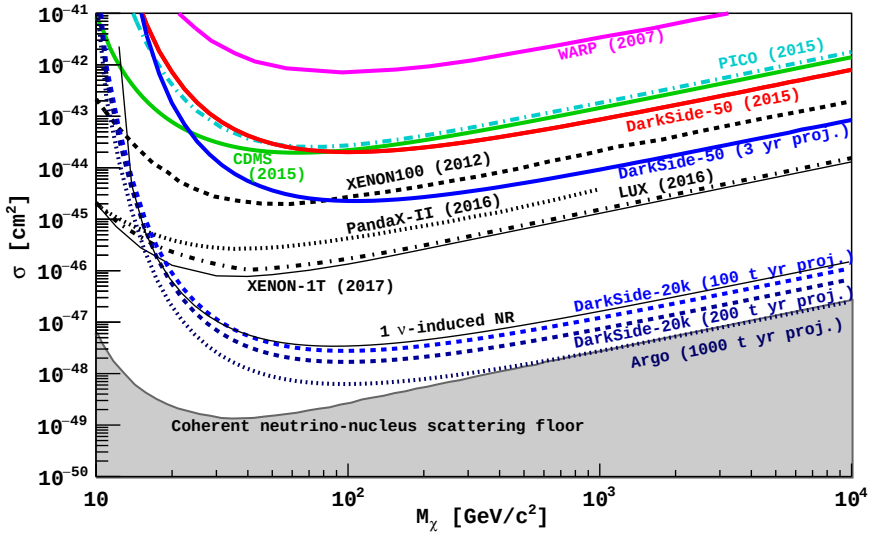

Fig. 1.9: Current results of direct dark matter search experiments, adapted to include the most recent results from references cited elsewhere in this section. The mean exclusion sensitivities for the full exposure of DarkSide-50, for DarkSide-20k, and for Argo are shown (see sec. 2.1 for more details). For comparison, the mean exclusion sensitivity for a generic argon-based experiment with a 30 keV threshold, 100 % acceptance for nuclear recoils, and expectation of one coherent ν-nucleus scatter during the lifetime of the experiment is also shown ("1ν-induced NR"). The grey shaded region is bounded from above by the "coherent neutrino-nucleus scattering floor", the ultimate experimental reach for a xenon based experiment with arbitrary exposure, see ref. [44]. Fig. from [48].

use liquid (or dual-phase) noble elements such as xenon and argon as target materials. Completed or operational xenon detectors include XENON1T [54], LUX [55] and PandaX-II [56]. In dual-phase xenon/argon time projection chambers a fiducial volume can be defined, so only events inside this volume are considered in data analysis. This allows liquid noble detectors to be self-shielding; the fiducial volume is in fact shielded by the remaining detector volume. The xenon technology has been used earlier in comparing to that of argon, on the other hands argon have a more powerful discrimination of electron-like vs nuclear-like events. The pioneer experiment utilizing argon has been the WARP experiment [57]. Within the DarkSide Program the DarkSide-50 experiment, at LNGS, is currently operating as a dual-phase Liquid Argon Time Projection Chamber (LAr TPC) using timing of the scintillation signal (pulse shape discrimination) as a discriminant

against background from electron recoils.

DM-nuclei scatterings also can be detected via thermodynamics micro-transitions in experiments based on superheated fluids used as a target material. DM particle passing through a detector can then be visualized thanks to an initiated process of bubble creation. Superheated liquid detectors such as COUPP [58], SIMPLE [59] and PICASSO [60] use a detector volume filled with droplets of superheated liquid such as C_4F_{10}. Due to the light targets such as fluorine used by these experiments, they are typically more sensitive to light WIMPs with SD interactions.

Recent results from some of these experiment are shown in Fig 1.9.

A final class of direct detection experiments are known as "directional" direct detection experiments. These aim to measure not only the energy deposited by WIMP scattering events but also the direction of the nuclear recoils. It is hoped that a recoil spectrum peaked in the direction opposite to the Earth's motion will provide strong evidence for a DM origin for the recoils. One possibility for this is the use of specialized gas Time Projection Chambers (TPCs), which allow measurable track lengths from which the recoil direction can be determined. Unfortunately, this kind of detectors are limited in mass, so in exposure. Another possibility is to exploit the so-called columnar recombination effect [61] in dual-phase liquid noble TPC, which is the principal motivation for ReD experiment, exactly based on a LAr dual-phase TPC detector.

2. THE DARKSIDE PROGRAM: DUAL-PHASE LIQUID ARGON TPCS WIMP'S DETECTORS

2.1 The DarkSide Program

The DarkSide Program aims at direct dark matter detection using dual phase (liquid and vapor) Argon TPCs. The program is staged, with detectors of increasing mass and sensibility, and installed at LNGS. The 1400 metre-rock thickness above the laboratory, corresponding to 3800 m.w.e., represents a natural coverage that provides a cosmic ray flux reduction by $\sim 10^6$ times with an effective muon flux of the order of 1.1 muons/(m^2hr) [62]; moreover, the flux of radiogenic neutrons in the underground halls is about $\sim 10^3$ times less than on the surface due to the very small amount of uranium and thorium of the Dolomite calcareous rock of the mountain.

Among the variety of detector technologies, the DarkSide Program opted for liquid argon (LAr) dual-phase TPCs which, detecting both the scintillation light and the ionization electrons produced by impinging radiation (see sec. 2.2), have significant advantages for direct dark matter searches. This technology ensures the precise determination of event positions in all three dimensions inside the active volume of the TPC. A fiducial volume can be defined within the detector so that only events inside this volume can be considered in data analysis. Moreover, for LAr the powerful discrimination against background using the time-development of the primary scintillation signal (pulse-shape discrimination or PSD), and the

effectiveness of chemical and cryogenic purification have all been demonstrated (see Refs. [63, 64] and references cited therein).

The first step of DarkSide Program consisted of a 10 kg active mass prototype detector, DarkSide-10, which allowed for optimization of the scintillation light yield, a critically important parameter for such devices[63]. The second step, DarkSide-50 now running at LNGS, has an active mass of about 50 kg now of Underground Argon (UAr), instead of Atmospheric Argon (AAr) initially used, to reduce up to 1.4×10^3 the β/γ background from ^{39}Ar β decay. From the analysis af DarkSide-50 data the DarkSide Collaboration has published background-free WIMP search results (< 0.1 events of background expected and no observed events in the search region) first from an exposure of $1422 \pm 67\,\mathrm{kg\,day}$ with atmospheric argon (AAr) [64], and then from a exposure of $16\,660 \pm 270\,\mathrm{kg\,day}$ with underground argon (UAr) [65].

The combined result of the AAr and UAr data analysis leads to the expectation that a result free from instrumental background can also be obtained from a much larger exposure with a multi-tonne detector. For the direct-detection searches, the ability to build experiments able to operate in a background-free mode will be crucial for a possible discovery of dark matter.

In December 2015, the DarkSide Collaboration submitted a proposal to Istituto Nazionale di Fisica Nucleare (INFN) and to the National Science Foundation (NSF) for the funding of the DarkSide-20k experiment aiming at a significant improvement in the sensitivity for the direct detection of WIMPs, reaching $1.2 \times 10^{-47}\,\mathrm{cm}^2$ for WIMPs of $1\,\mathrm{TeV}\,c^{-2}$ mass. It is proposed to achieve this goal with a LAr TPC experiment with an fiducial mass of 20 t, for a total exposure of 100 t yr to be accumulated in a run of 5 yr. Thanks to its exceptionally low

instrumental background, DarkSide-20k could extend its operation to a decade, increasing the exposure to 200 t yr and reaching a sensitivity of 7.4×10^{-48} cm^2.

It should be noted here that if it is defined the "one neutrino isoevent curve" for argon as the mean exclusion sensitivity for a generic argon-based experiment with a 30 keV threshold (100 % acceptance for nuclear recoils), and expectation of one coherent ν-nucleus scatter during the lifetime of the experiment, ν-induced background is expected even for the DarkSide-20k 5 yr run time planned exposure, as shown in Fig 1.9 (more in [66]). So all future LAr based DM search experiment will have to take into account the ν-induced background[1].

In the longer term, the plan of the DarkSide collaboration is to develop a path towards a dark matter experiment, called Argo, conceived to accumulate an exposure of 1000 t yr, free of background other than that induced by coherent scattering of neutrinos.

With dark matter interactions very rare and the onset of ν-induced nuclear recoils for exposures of 100 t yr and beyond, sensitivity to the direction of the nuclear recoils originating from WIMP scatters would be a very highly desirable capability for a direct dark matter detection experiment. A directional detector would have the capacity of breaking through the neutrino background and, if DM in form of WIMPs will be discovered, begin the era of "WIMP astronomy" (see [67] and references therein).

ReD experiment first aim to reveals directionality signature in energy nuclear recoils of the order of expected WIMP-Ar scattering recoils.

In the next sections a summary of the fundamental properties of liquid argon as radiation detection medium and dual-phase TPC's principles are presented.

[1] Also for xenon, even if with a different behavior versus WIMP mass.

Property	**Value**
Atomic number Z	18
Mean atomic weight	39.948 ± 0.001 u
Isotopes of interest ([68])	^{36}Ar(0.34%), Stable ^{37}Ar($Trace$), EC - $t_{1\backslash 2}$ 35 d ^{38}Ar(0.06%), Stable ^{39}Ar($Trace$), β^- - $t_{1\backslash 2}$ 269 yr ^{40}Ar(99.6%), Stable
Boiling point at 1 atm abs, T_b	87.26 K
Density	$\rho_{liquid} = 1399\,\mathrm{kg}\cdot\mathrm{m}^{-3}$ at T_b $\rho_{gas} = 1.761\,\mathrm{kg}\cdot\mathrm{m}^{-3}$ at 273 K, 1 atm
Dielectric constant	$\epsilon_{liquid} = 1.53$ at T_b [69] $\epsilon_{gas} = 1.00$ at 273 K, 1 atm [70]

Tab. 2.1: Some physical Properties of Argon (Atmospheric Argon)

2.2 Argon properties for particle detection

An important feature of LAr (in Tab. 2.1 some useful properties) is the production of both charge carriers and prompt scintillation photons in response to radiation (as well as heat).

The "dual-phase" technology has the main advantage to provide simultaneous access to the ionization and to scintillation signals. The prompt scintillation light (the so-called S1) is produced by de-excitation of excited dimers formed during the passage of radiation (see below), while ionization electrons escaping recombination are collected by applying an electric field (the "drift field") to the liquid-vapor interface, where they are extracted into the vapor by a stronger electric field (the "extraction field"). Once in vapor, electrons are ultimately collected to the anode and detected by observing the proportional scintillation light (the so-called S2) produced as they are accelerated through the vapor by a "multiplication field" (also called "electroluminescence field"). The time delay between S1 and S2, due to the uniform drift, and the hit pattern of the S2 signal allow for a 3D position

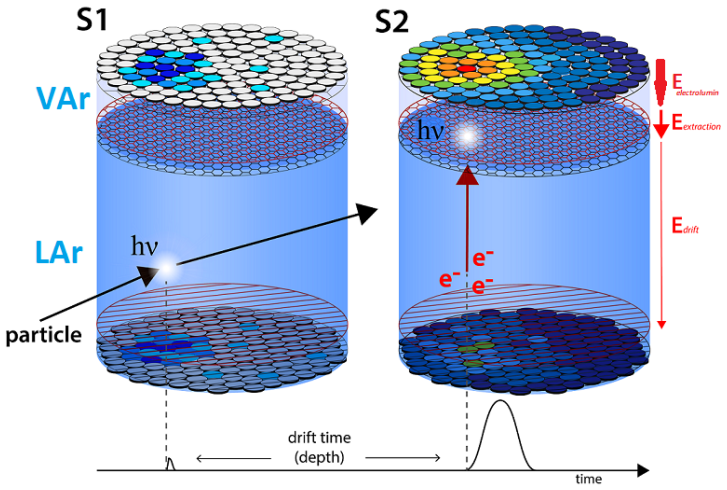

Fig. 2.1: Cartoon drawing of a double-phase argon TPC working principle. The black arrow indicates an incoming particle which interaction induces primary scintillation (S1) and ionization. Ionization electrons are drifted up into a region of vapor argon where produce a secondary proportional scintillation signal (S2). The two scintillation signals are detected by photosensor arrays.

determination (In Fig. 2.1 a cartoon drawing of a double-phase TPC working principle). These charge and light signals are highly complementary and anti-correlated (more in sec. 2.2.4).

2.2.1 Origin of scintillation

In the so-called recombination scintillation model, the origin of scintillation produced by radiation in LAr is attributed to the excitons (Ar^*) and electron-ion pairs ($Ar^+ + e^-$) created along the interacting particle track, which in a different way first form excited dimers to finally decay radiatively [71]. Free primary excitons directly form excited dimers (excimers - Ar_2^*) through the *self-trapping* process within a few picoseconds [72]:

i) Ar^*

$$Ar^* + Ar + Ar \rightarrow Ar_2^* + Ar \qquad \textit{(Self-trapping)} \tag{2.1}$$

For electron-ion pairs the process is a little more complex: while free ions form molecular ions Ar_2^+, also within a few picoseconds [72], emitted electrons lose their kinetic energy through production of excitons and electron-ion pairs till when they are thermalized through phonon interaction. Therefore a part of the thermalized electrons and molecular ions recombine and form excimers through deexcitation processes[2]:

ii) Ar^+

$$\begin{aligned} Ar^+ + Ar &\rightarrow Ar_2^+, \\ Ar_2^+ + e^- &\rightarrow Ar^{**} + Ar \qquad \textit{(Recombination)} \\ Ar^{**} &\rightarrow Ar^* + \text{heat} \\ Ar^* + Ar + Ar &\rightarrow Ar_2^* + Ar, \qquad \textit{(Self-trapping)} \end{aligned} \tag{2.2}$$

where the process "$Ar^{**} \rightarrow Ar^* + \text{heat}$" corresponds to a non-radiative transition. As mentioned above, excimers then decay radiatively from the lowest-excited molecular states via:

iii) Ar_2^*

$$Ar_2^* \rightarrow 2Ar + h\nu. \tag{2.3}$$

where $h\nu$ denotes a single photon.

In LAr emitted photons are in the so called second continuum, the vacuum ultraviolet (VUV) region with a wavelength peaked around 128 nm and width of approximately 10 nm[3] [75].

[2] A recent study has provided evidence of a static recombination, taking place for a limited fraction of electron-ion pairs on a time scale shorter than that of thermalization [73]. However this static recombination can be seen as a rescaling of the total initial charge.

[3] Some Infra Red (IR) radiation is also emitted [74], with total energy emitted as IR photons

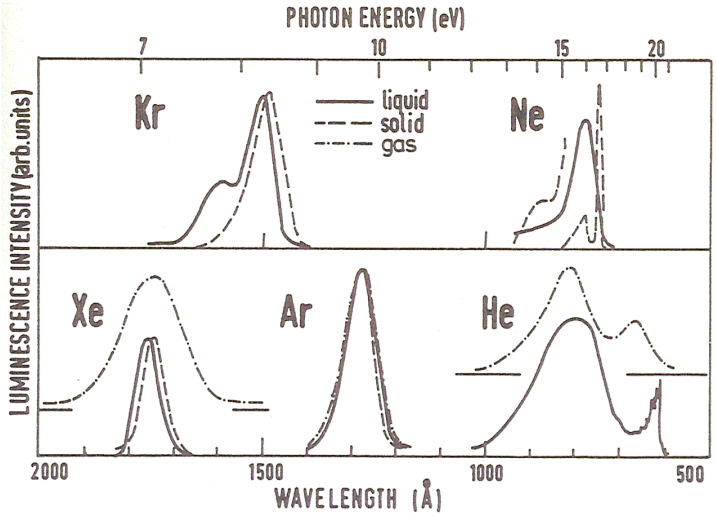

Fig. 2.2: Emission bands in liquid rare gases, together with solid- and high-pressure gas-phase spectra (Fig. from [70]).

In low density argon gas (on the order of almost a few mbar, see sec.2.2.7 for more details), inefficient argon atom collisions in the *self-trapping* process, which is a three body process, could lead to photon emission from high vibrational states of the lowest electronic energy level in diatomic argon molecules, giving rise to the first continuum with a wavelength around 110nm [76]. In high pressure gas or in the condensed phases as in vapor (see Fig. 2.2), excited diatomic molecules quickly relax to the lowest vibrational states and the second continuum dominates the emission spectrum[4].

The lowest electronic energy level of excimer that finally decays radiatively via (2.3), can have two spin states: a spin singlet state $^1\Sigma_u$ and a spin triplet state $^3\Sigma_u$. The energies of the two states are very close and can not be resolved in the emitted light. The singlet state (allowed) quickly decays to the ground state with lifetime $\simeq 7\,\text{ns}$. The decay of the triplet state to the ground state is nominally "forbidden" by spin selection rules, but can happen at a much larger

estimated in liquid $\sim 0.2\,\text{keV/MeV}$ [75], then negligible at least to the first-order.

[4] Third continuum emission is also reported in argon gas with wavelength around 200nm and lifetime from nanoseconds to hundred nanoseconds depending on the gas pressure [77].

time scale, so the triplet lifetime is found to be $\simeq 1.6\mu$s in liquid argon, about three orders of magnitude larger than singlet lifetime. The two decay components are usually referred to as the prompt component (τ_p or τ_S from Singlet) and the late component (τ_l or τ_T from Triplet). It is interesting to note that in LXe the singlet state has a lifetime $\tau_S \simeq 4$ ns while the triplet state lifetime is $\tau_T \simeq 21$ ns, so only one order of magnitude separates them. As will be clarified in section sec. 2.2.2, this implies a strong difference in the background rejection capability between LAr and LXe technologies.

Given that primary excitons and electron-ion pairs both form excimers through different mechanisms, in particular the excited electron from the exciton channel necessarily has the same spin as the promoted electron, while the recombination electron will have a spin largely uncorrelated with that of the ionized electron, both channels form triplet and singlet states with different probabilities. For example Hitachi *et al.* [72] reported the intensity ratio I_S/I_T of the singlet-to-triplet states as 0.3, 1.3, and 3 for electron, α-particle and for fission fragments excitation, respectively, which shows an enhancement of triplet states formation in lower deposited energy density. Electron recoils (ERs) and nuclear recoils (NRs) lose energy in atomic excitation and ionization through different mechanisms, in particular NRs with higher deposited energy density $\Big((I_S/I_T)_{NR} > (I_S/I_T)_{ER}\Big)$. Thus NR scintillation is more prompt with respect to ER scintillation. Accordingly, in LAr discrimination between ERs and NRs is primarily done using pulse shape discrimination (PSD) based on the timing of S1 scintillation light ([78]).

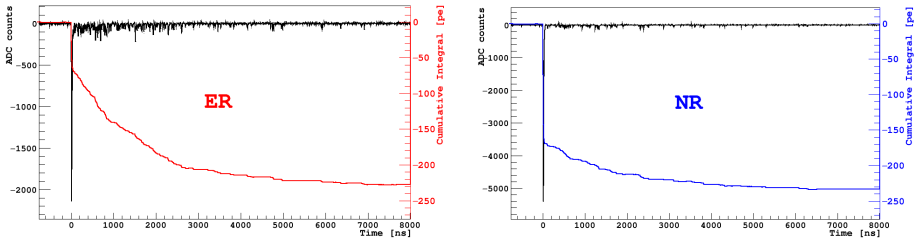

Fig. 2.3: Time evolution of a typical electron recoil (left) and nuclear recoil (right) events with a similar number of photons. The red/blue line indicates the cumulative charge distribution. Around the first 100 ns the value of the charge integral is very different for the two categories of recoils. Fig. from [80]

2.2.2 f_{prompt}: a simple parameter to do PSD

Following Lippincott *et al.* [79] a convenient way to do time based PSD is to classify events on the base of their fraction of light emitted in a prompt temporal window (t_{prompt}) with respect to the total scintillation time (t_{tot}):

$$f_{prompt} = \frac{\int_{t_0}^{t_{prompt}} S1(t)dt}{\int_{t_0}^{t_{tot}} S1(t)dt} \tag{2.4}$$

where t_0 corresponds to the arrival time of the first S1 scintillation photon. Fig. 2.3 shows the time evolution of a typical DarkSide-50 electron recoil (left) and nuclear recoil (right) events with a similar number of photons. As seen, around the first 100 ns the value of the charge integral is very different for the two categories of recoil. In DarkSide-50 a parameter called f_{90}, coherently defined as the fraction of the pulse integral of the S1 signal in the first 90 ns, is used for this pulse shape discrimination. With $t_{prompt} = 90$ ns DarkSide-50 maximizes the separation among the distributions of ERs and NRs. Fig. 2.4 shows the DarkSide-50 f_{90} distribution as a function of the S1 intensity during a calibration run with an Americium-Berillium (AmBe) neutron source. The events cluster in two distinct distributions: the lower one with a f_{90} average value of 0.3 is due to β-like events,

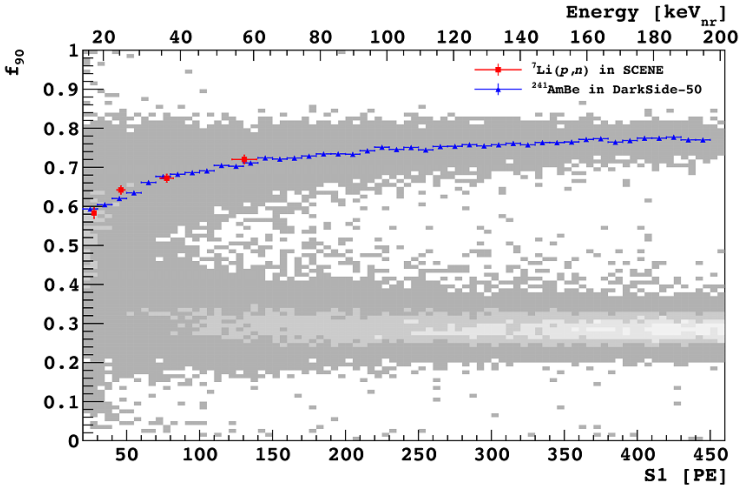

Fig. 2.4: f90 distribution as function of the S1 intensity during a calibration run with an Americium-Berillium (AmBe) neutron source. NR cluster around $f_{90} = 0.7$, while ER are in the $f_{90} = 0.3$ band. The blue dots show the medians of the NR branch as extracted from data. Red points represent values collected in SCENE experiment [82]. Fig. from [80]

the upper one, due to neutron scattering, has mean value around 0.7. The two classes of events are well separated at high S1 values, while at low energies their mean values converge towards 0.5 and their variances increase.

In Ref. [81] the DarkSide Collaboration showed that f_{90} based PSD rejected the single-sited ER events from ^{39}Ar decay to a level of one in 1.5×10^7.

It is worth noting that f_{prompt} power of separation between the distributions of ERs and NRs not only depends on LAr -or LXe- physical properties (τ_S vs τ_T). For instance f_{prompt} power of separation depends also on the range of the travel time of photons in the TPC before striking a device used to collect scintillation photons, then by TPC dimensions. Also the decay time of the wave-length shifter used in LAr TPCs has to be considered in the t_{prompt} choice. Segreto *et al.* [83] have reported that tetraphenyl-butadiene (TPB), usually used as wave-length shifter in LAr technology, shows a response function to 128 nm photons with a prompt exponential component by $\tau_{prompt} < 10$ ns and about 60% relative abundance, but also a longer exponential tail mainly consisting of $\tau \simeq 50$ ns and about 30%

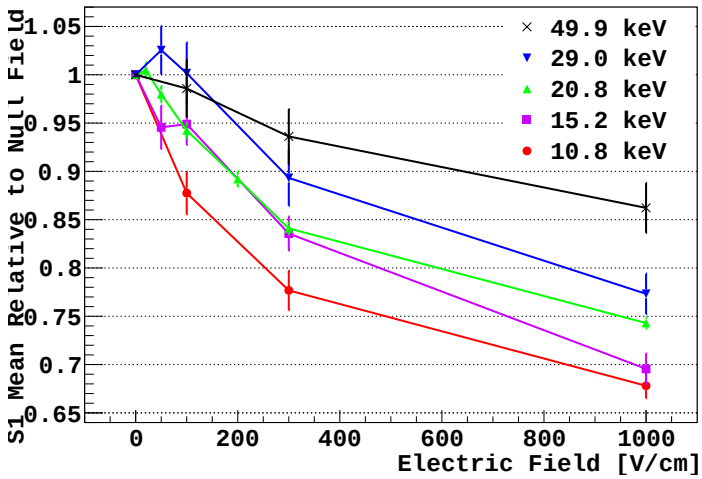

Fig. 2.5: Variation of the S1 scintillation yield for 10.8 to 49.9 keV nuclear recoils as a function of drift field normalized to the value at null field. Fig. from [82]

relative abundance (and other minor components). Finally, the response function of the devices used to collect photons can have a big impact on f_{prompt}: the greater is the recovery time of devices the lower become the discrimination power of the detector. In DarkSide-50 the photomultiplier tubes (PMTs) used to collect S1 and S2 photons produce signals of ~ 6 ns recovery time ([84]), more than fast enough for using $t_{prompt} = 90$ ns.

For the sake of completeness, I report another handle on ER/NR discrimination which comes from ERs and NRs S2/S1 ratio distributions. Indeed, as explained below, ERs are more ionizing with respect to NRs, so for the same S1 ERs show higher S2/S1 mean ratio. Thanks to much higher PSD ER rejection power with respect to S2/S1 ratio, in DarkSide-50 S2/S1 is not used for ERs vs NRs discrimination (instead it is used for example to discriminate α-background events in the TPB-coated PTFE walls).

Nuclear recoil energy [keV]	Scintillation efficiency $\mathcal{L}_{\mathrm{eff},\,^{83\mathrm{m}}\mathrm{Kr}}$
10.3	0.235 ± 0.011
14.8	0.239 ± 0.013
16.9	0.234 ± 0.010
20.5	0.257 ± 0.010
25.4	0.251 ± 0.011
28.7	0.264 ± 0.009
36.1	0.278 ± 0.010
49.7	0.291 ± 0.009
57.3	0.295 ± 0.010

Tab. 2.2: Scintillation efficiency of nuclear recoils relative to that of electron recoils from 83mKr at zero field (from [85]).

2.2.3 Quenching factors

Recombination increases the number of S1 photons. In the presence of an electric field, a part of electrons coming from ionization are collected and, consequently, recombination decreases. The S1 light quenching in LAr, introduced by the presence of a drift field for NRs, was first discovered and then precisely measured by the SCENE experiment (Fig. 2.5), which results were then applied to DarkSide-50 experiment to optimize S1 and S2 signals.

Moreover, it is well know that noble liquid scintillators have reduced scintillation yield for NRs compared to ERs. Only a fraction of the energy loss results in ionization and atomic excitation. Data in Tab. 2.2 are values measured from SCENE of the scintillation efficiency of nuclear recoils relative to that of electron recoils $\mathcal{L}_{\mathrm{eff},\,^{83\mathrm{m}}\mathrm{Kr}}$,

$$\mathcal{L}_{\mathrm{eff},\ ^{83m}\mathrm{Kr}}\left(E_{\mathrm{nr}},\,\mathcal{E}_{\mathrm{d}}\right)=\frac{S1_{\mathrm{nr}}\left(E_{\mathrm{nr}},\,\mathcal{E}_{\mathrm{d}}\right)/E_{\mathrm{nr}}}{S1_{\mathrm{Kr}}\left(\mathcal{E}_{\mathrm{d}}=0\right)/E_{\mathrm{Kr}}},\tag{2.5}$$

where the scintillation efficiency is relative to ERs from ^{83m}Kr at zero field, with $E_{\mathrm{Kr}} = 41.5$ keV E_{drift} is the drift electric field and E_{nr} is the recoil energy [85].

To keep clear the NR quenching factor respect to ER, it is common to use units of "keV electron equivalent" or keVee which express the energy an electron would need to have to produce some amount of scintillation light, while keVnr or $\mathrm{keV_{rec}}$ etc refers to nuclear recoil energy.

As proposed by Hitachi *et al.* [72] scintillation light can be suppressed (in NR, but not only) by competing processes that allow excitons or excimers to decay non-radiatively. The rate of these processes is proportional to the square of the exciton density, therefore suppresses more scintillation at higher densities. Biexcitonic quenching, photo-ionization, and the Penning process allow argon excitons or excimers to non-radiatively de-excite through the following three mechanisms, respectively:

$$\begin{aligned} \mathrm{Ar}^* + \mathrm{Ar}^* &\rightarrow \mathrm{Ar} + \mathrm{Ar} + \mathrm{e}^- \qquad \textit{(Biexcitonic collisions)} \\ \mathrm{Ar}^* + \mathrm{Ar}_2^* &\rightarrow \mathrm{Ar} + \mathrm{Ar}_2^+ + \mathrm{e}^- \qquad \textit{(Photo-ionization)} \\ \mathrm{Ar}_2^* + \mathrm{Ar}_2^* &\rightarrow 2\mathrm{Ar} + \mathrm{Ar}_2^+ + \mathrm{e}^- \qquad \textit{(Penning process)} \end{aligned} \tag{2.6}$$

In a more global view Mei *et al.* [86] attributed reduction of scintillation efficiency in nuclear recoils, respect to β/γ-like recoils, to two major mechanisms:

- energy loss due to nuclear collisions, determining a relative quenching factor $f_L(E_{rec})$ (Lindhard's theory [87])
- scintillation quenching due to hight ionization and excitation density induced by nuclear recoils, determining a relative quenching factor $f_B(E_{rec})$ (Birks's saturation law [88]),

where E_{rec} is the nuclear recoil energy.

SCENE has shown that considering independent the two effect (as suggested

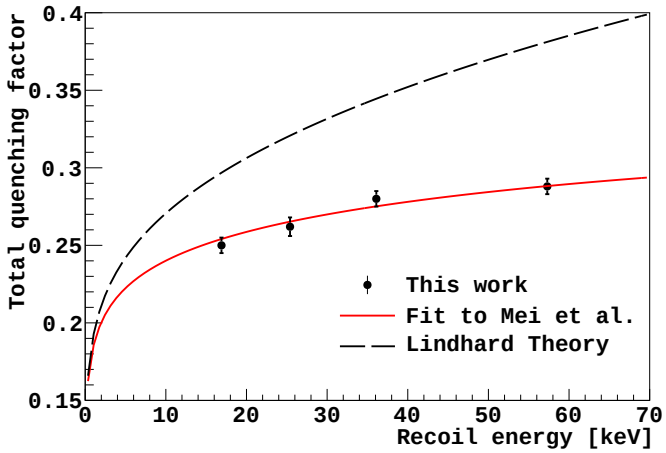

Fig. 2.6: Fig. from SCENE Collaboration - "This work" is referred to [85]. The- nuclear-total quenching factor is here relative to ^{83m}Kr.

by Mei *et al.* [86]), a global Lindhard-Birks quenching factor given by $f_{LB} = f_L \cdot f_B$ describes the scintillation of neutron-^{40}Ar recoils well (fig. 2.6 from Cao *et al.* [85]).

2.2.4 Correlation between Ionization and Scintillation signals

As said, the energy E_0 transferred by a particle interacting in LAr is split between three channels: ionization, excitation and heat. A general relation can be written:

$$E_0 = N_i E_i + N_{ex} E_{ex} + heat, \tag{2.7}$$

where E_i and E_{ex} are the mean energies spend to ionize or to excite an atom, while N_i and N_{ex} are the mean numbers of electron-ion pairs $Ar^+ + e^-$ and excited atoms Ar^*, respectively.

A complete picture of the energy transfer mechanism, as well as energy sharing between different channels for energy in the DM searches range, is still missing, both for nuclear an β-like recoil. However it is well established that the distribu-

tion of N_i with respect to N_{ex}, is different for the two interactions. Moreover, in the case of nuclear recoil a significant fraction of the particle energy is spend in nuclear collision, so the *heat* terms in 2.7 is proportionally bigger, with respect to β-like case, at the same incident energy (part of the quenching factor previously discussed).

The recombination scintillation model previously illustrated allow to explain the relationship between the number of excitons, $N_{\rm ex}$, and electron-ion pairs, $N_{\rm i}$, produced by ionizing radiation, and the S1 and S2 signals in a liquid noble gas TPC. The total number of scintillation photons can be written as,

$$N_{\rm ph} = \eta_{\rm ex} N_{\rm ex} + \eta_{\rm i} r N_{\rm i}, \tag{2.8}$$

where r is the fraction of ions that recombine (which depend on an applied electric field), and $\eta_{\rm ex}$ and $\eta_{\rm i}$ are the efficiencies with which direct excitons and recombined ions produce scintillation photons respectively. If Penning or Hitachi quenching processes are not included in the definition of $\eta_{\rm ex}$ and $\eta_{\rm i}$, instead assuming these processes affect $N_{\rm ex}$ and $N_{\rm i}$ directly[5], we expect $\eta_{\rm ex}$ and $\eta_{\rm i}$ to both be unity, so

$$N_{\rm ph} = N_{\rm ex} + r N_{\rm i}. \tag{2.9}$$

Defined the S1 and S2 measurement gains g_1 and g_2 such that

$$\begin{aligned} S1 &= g_1 N_{\rm ph} = N_{\rm ex} + r N_{\rm i} \\ S2 &= g_2 \left(1 - r\right) N_{\rm i}, \end{aligned} \tag{2.10}$$

[5] Note that as defined $N_{\rm ex}$ and $N_{\rm i}$ are the numbers of excitons and ions remaining after any track-dependent quenching processes, such as the ones in 2.7.

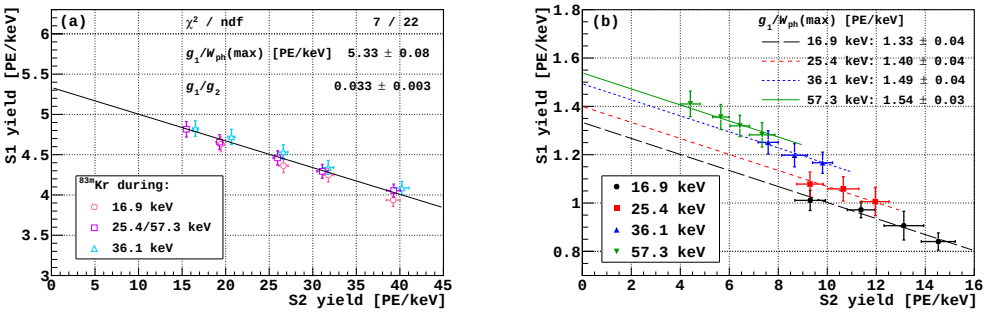

Fig. 2.7: Right S1 yield vs. S2 yield for ^{83m}Kr. The best fit results for Eq. (2.13) are shown for SCENE experiment configuration. *Left* S1 yield vs. S2 yield for nuclear recoils. Fig. from [85]

(as said $S1$ and $S2$ are the scintillation and ionization signals) it is reasonable to expect that g_1 and g_2 are detector properties, hence remain constant from electron recoils to nuclear recoils. Putting together equations 2.10, you can write

$$\frac{S1}{g_1} + \frac{S2}{g_2} = N_{\rm ex} + N_{\rm i}, \tag{2.11}$$

which highlights the inherent S1-S2 anticorrelation. Considering the average energy required for the production of a single photon in the limit $r \to 1$, $W_{\rm ph}(\max)$,

$$W_{\rm ph}(\max) = \frac{E_0}{N_{\rm ex} + N_{\rm i}}, \tag{2.12}$$

the inherent S1-S2 anticorrelation in the recombination scintillation model can now be expressed as:

$$\frac{S1}{E_0} = \frac{g_1}{W_{\rm ph}(\max)} - \frac{g_1}{g_2}\frac{S2}{E_0}. \tag{2.13}$$

$W_{\rm ph}(\max)$ has been measured by Doke *et al.* [75], with a value of 19.5 ± 1.0 eV, using ^{207}Bi conversion electrons, from measured LAr scintillation efficiency ($\sim$ 50 photons/keV for 1 MeV β-like recoils). Fitting with eq. 2.13 data taken at different drift field and nuclear energy recoils, SCENE found that y-intercept

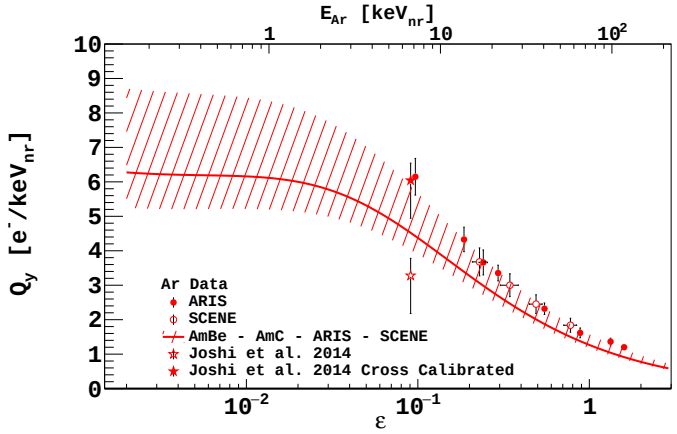

Fig. 2.8: Measured ionization yield, Q_y, for nuclear recoils in LAr as a function of alternatively E_{nr} in top axis and the so-called reduced energy parameter ϵ in bottom axis (in argon $\epsilon = 13.57 \times 10^{-3}\,\mathrm{keV}^{-1}$). Also shown is the Bezrukov model fit to ^{241}AmBe and $^{241}\mathrm{Am13}^{\mathrm{C}}$ data taken with DarkSide-50. Fig. from [89], for more details see text and references therein.

$[g_1/W_{\mathrm{ph}}(\mathrm{max})]$ increases with increasing nuclear recoil energy, implying that $W_{\mathrm{ph}}(\mathrm{max})$ decreases and scintillation efficiency increases with energy recoil (Fig. 2.7).

If now we consider the average energy required for an electron-ion pair production, the so-called W-value [6] we can write:

$$W_{\mathrm{ph}}(\mathrm{max}) = \frac{W}{1 + N_{\mathrm{ex}}/N_{\mathrm{i}}}. \tag{2.14}$$

In conclusion $N_{\mathrm{ex}}/N_{\mathrm{i}}$ increases when nuclear energy recoil decreases. Moreover if we consider the ionization yield for nuclear recoil, Q_y, it can be found that it varies from $\sim 1.5\,e^-/\,\mathrm{keV_{nr}}$ for $E_{rec}\,\mathscr{O}(100\,\mathrm{keV_{nr}})$ up to $\sim 6.5\,e^-/\,\mathrm{keV_{nr}}$ for $E_{rec}\,\mathscr{O}(10\,\mathrm{keV_{nr}})$, as shown in Fig.2.8.

[6] W $= E_0/N_i = E_i + E_{ex}(N_{ex}/N_i) + (heat/N_i)$; so W $> E_i$ counts for the energy loss in excitation of atoms and heat. Instead $E_i >$ I (ionization potential) counts for the fact that some ionized atoms can be excited or double charged. The usually used value is W = 23.6±0.3 eV from ^{207}Bi conversion electrons. See Doke *et al.* [75] and references therein.

2.2.5 Electric field, tracks and effects on recombination

Applied electric fields are known to modify the recombination of electron-ion pairs in ionizing radiation tracks, effect due to the action of electric fields on the fraction of ions that recombine r (see eq. 2.10). In the so called Columnar Recombination (CR) model Jaffé [61] suggests that the magnitude of these effects should vary with the angle between the field and the track direction. The CR model assumes a cylindrical symmetrical distribution of ions along the average path of the recoiling nucleus, depending on the recoiling particle and its energy. The idea is that when the ionized *column* along the average direction of the straggling recoil nucleus is parallel to the electric field, the electrons drifting along this column, where the density of ions is high, have an increase in the probability of recombination, while when the ionized *column* is orthogonal to the electric field, electrons drift away from it and the chance of escaping without recombining increases. Thus the probability of recombination decreases when the electric field component orthogonal to the track $\mathcal{E}_\perp = \mathcal{E}\sin\theta_r$ increases ($\mathcal{E}$ is the electric field and θ_r the angle between track and electric field). Therefore, at fixed recoil energy S_2 is expected to increases, while S1 decreases, with $\sin\theta_r$. So an accurate measurement of the sum (S1 + S2) and the ratio (S1/S2) of the two signals may provide an indication on the track direction.

In a non exhaustive manner, with assumptions generally valid (in particular for electric field $\mathcal{O}$(kV/cm)) the fraction that survive recombination $\mathscr{R}_J$ in Jaffe theory can be write:

$$\mathscr{R}_J = [1 + k_c(dE/dx)/(\mathcal{E}\sin\theta_r)]^{-1}, \tag{2.15}$$

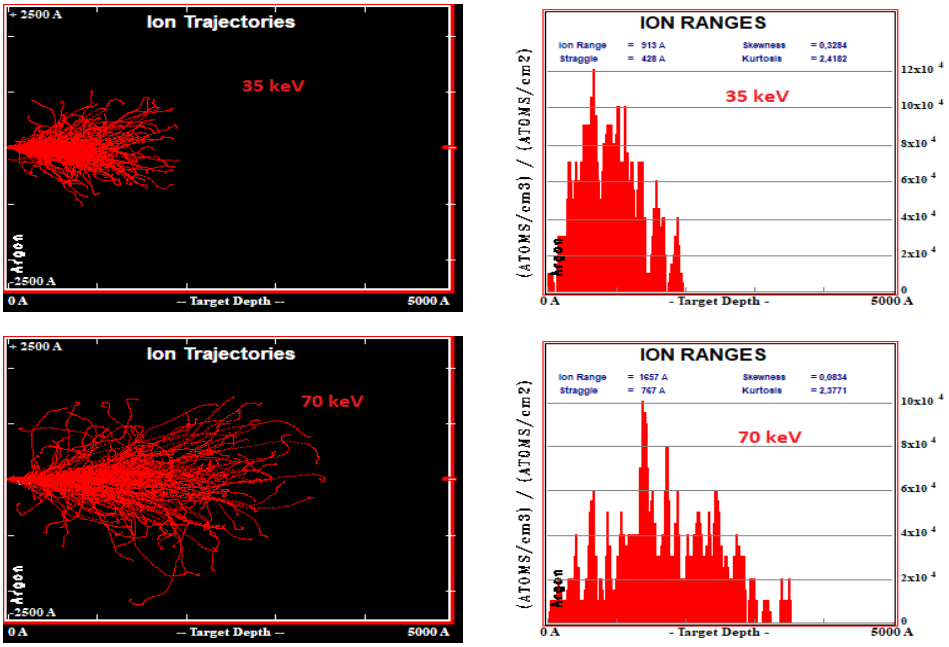

Fig. 2.9: Superposition of 200 tracks argon ions (viewed as the recoiling nuclei) in LAr, evaluated using (SRIM) [90]. Ions are originates in the same position and with a momentum whose initial direction is "horizontal " ($A \equiv Angstrom$). *Top panels* Argon ions energy $E_R = 35\,\mathrm{keV}$. *Bottom panels* Argon ions energy $E_R = 70\,\mathrm{keV}$.

where k_c is a constant that is assumed to be specific to liquid argon, (dE/dx) is the particle stopping power (and "$_J$" stay for Jaffé). As expected the angular dependence is on $\sin\theta_r$.

In a recent work Cataudella *et al.* [91] derived a new model describing the recombination of electron-ion pairs in ionizing tracks in the presence of a drift field. This new model describes the initial distribution of the electron ion cloud as that of an elongated ellipsoid, with R as single adimensional parameter accounting for elongation. By proper tuning of the parameter, this model is brought to coincide with the Jaffé model in the limit $R \to \infty$. By solving the equations describing the evolution of the electron-ion cloud, they determined that the dependence of the recombination fraction upon the angle between track and drift field is described by the function $f(\theta_r, R) = \sqrt{\sin^2\theta_r + \cos^2\theta_r/R^2}$. The model successfully reproduces the hight energy proton ($\mathcal{O}(10e2)\,\mathrm{MeV}$) ArgoNeuT data [92] for a specific choice of

the parameter R, extracted from data. Nevertheless the portability of this study for WIMPs- or neutrons-induced nuclear recoils in the energy range of interest is quite hard.

In order to produce a direction-sensitive response, the ionizing particle must has enough energy (range) to form a track with a definite direction. Following the arguments of [93], one might expect such a response to start for nuclear recoils above the energy where the length of the track exceeds the Onsager radius, $r_O = e^2/4\pi\epsilon K$, which is the distance between a positive ion and a free electron for which the potential energy of the electrostatic field, $e^2/4\pi\epsilon r_O$, is equal to the kinetic energy of a thermal electron, $K = 3kT/2$. In liquid argon ($T = 87\,\mathrm{K}$, $\epsilon = 1.5$) $r_O \simeq 80\,\mathrm{nm}$. The range of argon recoils in liquid argon can be roughly evaluated using J. Ziegler's tool "Stopping and Range of Ions in Matter" (SRIM) [90] with which you get that the mean range is about 90 nm at 35 keV E_R, it increases at about 140 nm at 57.3 keV E_R (substantially exceeding the r_O), up to about 160 nm at 70 keV E_R (Fig 2.9).

Such directional effects have been reported from experiments using tracks in liquid argon from α particles [94] and, as mentioned, protons [95]. SCENE too gave a hint for the same directional signature in S1 signal of nuclear recoils of $E_R = 57.3\,\mathrm{keV}$, the energy at which, following SRIM, one might expect the ion range to be sufficient to form a track with a definite direction with respect to the Onsager radius (140 nm vs 80 nm, as saw above). However, the corresponding S2 signal measured by SCENE did not show the same hint for a directional effect, Fig 2.10.

ReD experiment aim to has more clear results to understand at which recoil energy it can be said that tracks have detectable directions in a dual-phase LAr

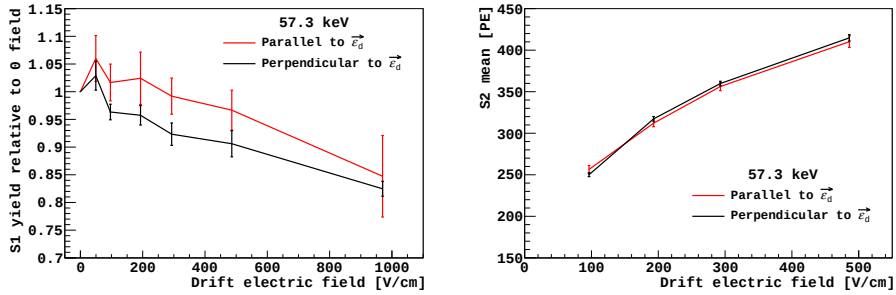

Fig. 2.10: *Left* S1 yield wrt drift field relative to null field. *Right* Electroluminescence (S2) yield wrt drift field. Fig. from [85].

TPC. If confirmed, the recoil directionality in LAr will provide an extraordinary and unique signature for the direct dark matter searches.

It is important to stress that the nuclear recoil direction is not accessible in liquid xenon in the dark matter search energy region of interest, because of the too short nuclear track lengths. D. R. Nygren stated in [93] that: "No electrostatic sense of directionality remains in LXe for nuclear recoils of interest, and directional sensing is beyond hope". Indeed in LXe the Onsager radius is 54 nm, not exceedable by nuclear recoil tracks in the energy range of interest.

2.2.6 Electron emission from liquid to gas

The fact that excess electrons (e.g. generated from ionizing radiation) can cross, under moderate electric field (so-called "extraction field"), the solid-vapor and liquid-vapor boundary in Ar has been known for 70 years [96].

In LAr the ground state of energy V_0 of a free electron is somewhat lower than in vacuum (or gas or vapor), by ~ 0.21 eV relative to the vacuum (while ~ 0.67 eV in xenon). Therefore, it is energetically advantageous for electrons to remain in the liquid phase. However electrons in LAr can exist in a quasi-free state with almost 100% probability [97]. Behavior of quasi-free electrons near the interface of non-polar dielectrics like Ar, can be described in terms of a one-dimensional

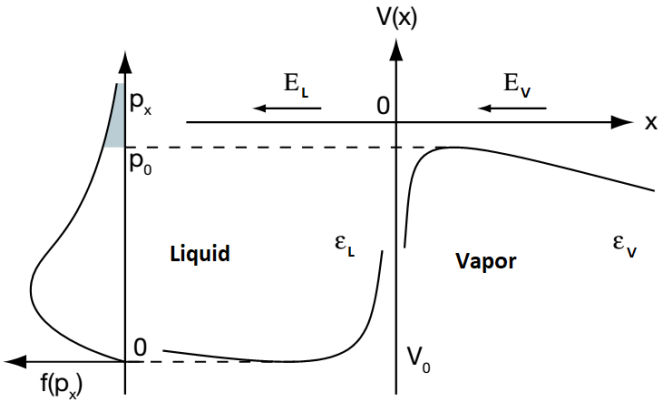

Fig. 2.11: Sketch of potential energy distribution of quasi-free electrons near the interface Liquid-Vapor. Also the Maxwell-Boltzmann distribution of momentum component perpendicular to the interface p_x is presented.

potential energy distribution (L an V subscripts for Liquid an Vapor):

$$\begin{aligned} V_L(x) &= V_0 - e\mathcal{E}_L x + A_L, \qquad x < 0 \\ V_V(x) &= -e\mathcal{E}_V x + A_V, \qquad x > 0 \\ A_{L,V} &= -\frac{e^2}{4\epsilon_{L,V}(x + \beta\frac{x}{|x|})} \cdot \frac{(\epsilon_L - \epsilon_V)}{(\epsilon_L + \epsilon_V)} \end{aligned} \tag{2.16}$$

where $\mathcal{E}_{L,V}$ are the electric fields[7], $\epsilon_{L,V}$ are the dielectric constants and $A_{L,V}$ are obtained by applying the so-called Schottky model, which essentially describes the barrier effect as an interaction between the electron and its dielectric image (for details see [98] and [99]). The value of a cutting parameter β (which avoids divergences for $x \to 0$) is about the thickness of the liquid-vapor transition layer, which it can assumed be a few times the liquid inter-atom distance. Then the potential barrier is the sum of two components: the potential step of height V_0 and the image potential of a charge placed above the liquid surface. An immediately effect of the external field, is some reduction of the height of the potential barrier at the liquid-vapor interface.

[7] $\mathcal{E}_{L,V}$ are in general relate, e.g. in a TPC $\mathcal{E}_V = \frac{\epsilon_L}{\epsilon_V}\mathcal{E}_L$ (See sec. 2.3)

In the so-called "thermo-electron emission" model, only those electrons which have a x-projection p_x of momentum $\vec{p}$ exceeding a threshold value $p_0 \approx \sqrt{2m_e|V_0|}$ can be emitted (Fig.2.11). According to this model, a drifting ionization electron, once reached the interface, could follow two different destinies: depends on p_x value vs p_0 it could overcome the barrier or be backscattered to liquid[8].

In absence of electric field the spontaneous emission from liquid argon at $\sim$ 87 K is strongly suppressed since the potential barrier V_0 is much higher than the mean thermal energy kT of free electrons ($V_0/\,\mathrm{kT_{LAr}} \sim 30$ in LAr and $V_0/\,\mathrm{kT_{LXe}} \sim 70$ in LXe). However even a weak electric field forcing electrons to approach the surface can ensure that some electrons, in the upper tail of the Maxwellian momentum distribution, can directly overcome the barrier. These directly emitted electrons represent the so called "hot" electrons, since they possess a mean energy that is higher than thermal energy $\sim$ kT. These electrons are emitted very fast. With increasing drift field strength a higher average value of the electron velocity distribution is obtained, hence the tail with $p_x > p_0$ becomes more populated. So, the so-called "hot" component increases with the electric field strength. Another effect of the external field is that the distance at which the resulting potential curve in the vapor reaches its maximum also depends on the field strength. The maximum approaches the liquid surface with increasing field, thus reducing the probability of the electron back-scattering into the liquid.

Many electrons, however, do not cross the surface barrier at the first attempt. They are reflected back into the bulk of the liquid and, after a number of scatterings, return to the surface guided by the field. Again, those which do have $p_x > p_0$

[8] There a third possibility: the backscattering of emitted electrons from the vapor atoms-molecules to the liquid, followed by electron cooling. In this context that process can be included in the backscattering on the potential barrier.

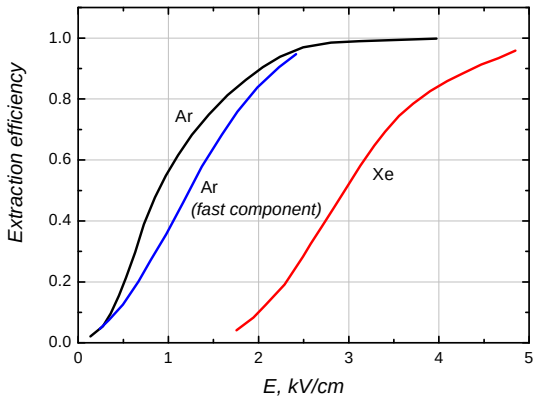

Fig. 2.12: Efficiency of electron extraction for Ar an Xe from liquid to gas as a function of electric field. Fig. from [35].

cross it, but the remainder return to the bulk and so forth. This process is similar to thermal evaporation from the tail of a Maxwell-Boltzmann distribution, hence the name "thermal emission" for this second mechanism. Note, however, that the mean energy of these electrons is not necessarily equal to the thermal value, while depends on electric field in LAr.

Coherently with the "thermo-electron emission" model, two very distinct time constants have been observed in LAr for the emission time: a fast component, of the order of 1 ns or less, and a very slow emission, up to ∼1 ms at $E \sim 100$ V/cm. The time constant of the slow component depends on the field as $1/E$, as suggested by the thermal emission model. In figure Fig. 2.12 emission efficiency of LAr and LXe are presented as a function of electric field (as expected due to the high surface barrier, in liquid xenon there isn't a distinguishable contribution from thermal emission). Note that around 3 kV/cm the extraction efficiency approaches 100% for argon [98].

2.2.7 *Electroluminescence in vapor*

Once in vapor, electrons can easily be accelerated by the applied electric field $\mathcal{E}_V$ to sufficient energies to excite atoms and thus produce S2, the secondary

scintillation. The electric field has to be strong enough for excitation but not for ionization of the gas atoms, to avoid cascades of secondary electrons (avalanche) and preserve a proportional behavior.

The mechanism of secondary scintillation depends on the number density n of atoms in gas. Atoms are initially excited by electron impact to one of the lowest excited states. At low number density (less than a few mbar for gas), collisions between atoms are rare, so excited atoms have enough time to decay to the ground state with emission of VUV photons, with wavelengths of about 107 nm. As the number density increases, the collision frequency also increases and formation of diatomic excimers Ar_2^*, through the *Self-trapping* mechanism (described in 2.1), can starts. In gas phase and pressures of 1 bar or above, the atomic lines are very much suppressed, so that the emission spectrum shows only the *second continuum*, as said in sec. 2.2.1. Anyway, in pressure and $\mathcal{E}_\mathcal{V}$ ranges of interest for dual-phase detectors, vapor meets certainly the number density necessary to consider the emission only in the *second continuum*.

As first showed by Conde, Ferreira, and Ferreira [100] for xenon, but also valid for argon, for values of pressure and field normally used in dual-phase detectors, the "reduced light output", i.e. the number of photons produced by a single electron traversing the unit of distance, divided by the gas pressure, depends only on the reduced electric field respect the gas pressure, but not on the alone gas pressure valor. The correct way to take into account microphysics of the electroluminescence, is to express the above-mentioned relation through the number density [101]:

$$\frac{1}{n}\frac{dN_{ph}}{dx} = \alpha\frac{\mathcal{E}_\mathcal{V}}{n} - b \quad [\text{photons}\cdot\text{cm}^2/e]\,, \tag{2.17}$$

where, as said, $\mathcal{E}_\mathcal{V}$ is the field strength (in kV/cm) and n is the number density (in

Constant(Unit)	Value
α (kV^{-1})	81.3
b (cm^2)	1.90×10^{-18}
β ($bar^{-1}{\cdot}cm^{-1}$)	148.3
γ (cm^{-1})	14.6

Tab. 2.3: Secondary scintillation coefficients in equations (2.17) and (2.18); a and b data from [35] while for β and γ see text.

atoms per cm^3 - related to the gas density ρ through $n = (N_A/M) \cdot \rho$, being N_A Avogadro's number and M the molar mass); α and b are gas-specific empirical coefficients (in Tab. 2.3 values for argon are listed).

Secondary scintillation is a threshold process, requiring a minimum reduced field $\mathcal{E}_\mathcal{V}/n \approx (4\pm1) \cdot 10^{-17}$ V·cm^2/atom.

For practical purposes, a more convenient parameterization of the light yield, as a function of field strength and gas pressure, can be used:

$$\frac{dN_{ph}}{dx} = \alpha\mathcal{E}_\mathcal{V} - \beta P - \gamma \quad [\text{photons}/(e{\cdot}\text{cm})]\,, \tag{2.18}$$

with P in bar. It takes into account the fact that the density of the saturated vapor is described with really good approximation, up to at least 10 bar, by a linear function of pressure. In Fig. 2.13, on the left we can see a fit, with $\rho(P) = mP+q$, on density vs pressure data, with P from triple point pressure (0.6889 bar) up to 1.6 bar, a standard pressure range for LAr dual-phase TPCs. The β and γ values in Tab. 2.3 come from this fit (data for fit from [102]). Finally, in Fig. 2.13 on the right the number of photons generated by one electron over a distance of 1 cm is plotted as a function of E, at different pressure values.

In terms of pressure, the minimum field required to have electroluminescence is $\mathcal{E}_\mathcal{V}/P \approx 1.0 \pm 0.3$ kV/cm/bar at room temperature ($T \simeq 300\,\text{K}$). If

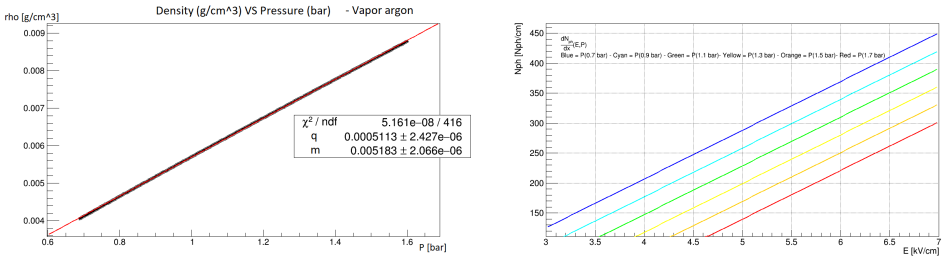

Fig. 2.13: Left Fit on density vs pressure with $\rho(P) = mP + q$ and P from triple point pressure (0.6889 bar) up to 1.6 bar. Data from [102]. *Right* Number of secondary scintillation (electroluminescence) photons generated by an electron traveling 1 cm in vapor, at different vapor pressure, as a function of electric field (eq. 2.18). Blue(0.7 bar) - Cyan(0.9 bar) - Green(1.1 bar) - Yellow(1.3 bar) - Orange(1.5 bar) - Red(1.7 bar).

the temperature is different, P should be treated as the equivalent pressure at room temperature for the same gas density. For instance, for vapor argon at $T = 87.5K$ we find $\rho(P = 1\,\text{bar}; T = 87.5\,\text{K}) \simeq 5.7 \times 10^{-3}\,\text{gcm}^{-3}$ and $P(T \simeq 300\,\text{K}; \rho \simeq 5.7 \times 10^{-3}\,\text{gcm}^{-3}) \simeq 3.5\,\text{bar}$ (data from [102]). So we get, for argon vapor in the working "standard condition" of a TPC, that the minimum field required to get electroluminescence is around $\mathcal{E}_\mathcal{V}/P \approx 3.5$ kV/cm/bar.

2.2.8 *Drifting electrons: "lifetime" and "attenuation length"*

In double phase LAr TPC technology it is important to take care on LAr purity. Indeed both electronegative or not, impurities could modify either primary scintillation (S1) and ionizations (S2) signals, or via electrons attachment or via additional non radiative quenching factor. For instance, ionization electrons survived recombination could eventually suffer from electronegative impurities attachment, so S2 signal could have a reduced relative intensity. Because recombination accounts for primary scintillation signal, also S1 could suffer for relative intensity reductions due to electronegative impurities, but in far lower way with respect to S2. By the way, while S1 relative intensity reduction do not depends on interaction vertex inside LAr active mass, but only on impurities concentration, S2

relative intensity reductions depends also on interaction position, since electrons could be captured during their drift to the grid. Moreover S1 and S2 relative intensity reductions are also function of the applied electric drift field, since the capture cross section depends on electron velocity.

In the usually verified condition for which numeric density of impurities is lower than that of free electrons, the equation

$$N_e(t) = N_e(0) \exp(-\frac{t}{\tau_l}) \tag{2.19}$$

describes the time dependence of the numeric density of free electrons $N_e(t)$. Here τ_l is the so called *lifetime*, which depends on type and numeric density of impurities (as well as on electric field, as said).

As S2 depends linearly on N_e (see sec. 2.2.7), in TPC technology a simple way to check for τ_l is to measure S2 intensity, from a source diffuse in the volume, versus t_{drift}, which is the time that electrons spend to drift towards the grid.

Another way to describe N_e reduction is using the so called *attenuation length* $\lambda = v_d \tau_l$, where v_d is the electrons drift velocity (which as well depends on electric field), and represents the distance traveled after which the number of survived electrons reduces by a factor $1/e$.

It is worth noting that a feature depending on impurities is S1 pulse shape, which can be modified because of reduced recombination and triplet-to-singlet ratio consequent modification. Therefore impurities, causing S1 pulse shape modification, can affect f_{prompt} separation power among ERs and NRs distributions (see sec. 2.2.2).

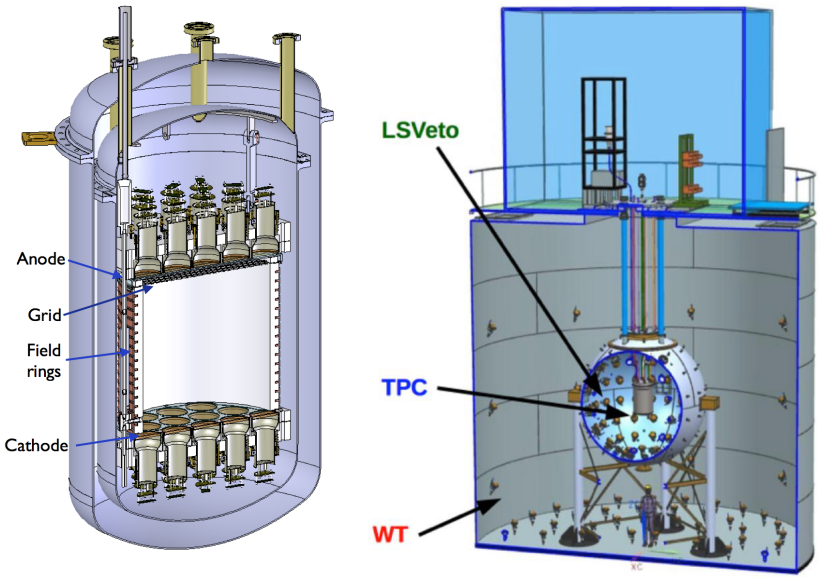

Fig. 2.14: The nested detector system of DarkSide-50. *Left* The TPC in the stainless steel cryostat. *Righ* The LAr TPC cryostat inside the LSV (the sphere), inside the WCD (the cylinder).

2.3 Principle of operation of a dual-phase LAr TPC: the DS50's TPC

As a case of study, in this paragraph is described the DS50's TPC, with some additional details regarding principles of working of a dual-phase TPC.

The DarkSide-50 TPC is contained in a stainless steel cryostat, which is nested in two other detectors (Fig. 2.14 right), the Liquid Scintillator Veto (LSV - serving as shielding and as anti-coincidence for radiogenic and cosmogenic neutrons, γ-ray, and cosmic muons), and the Water Cherenkov Detector (WCT - serving as shielding and as anti-coincidence for cosmic muons).

The active LAr, bounded by cylindrical 2.54 cm-thick PTFE-reflector wall (fabricated with a modified annealing cycle to increase its reflectivity), a fused silica cathode window, and a stainless steel grid, is viewed by 38 Hamamatsu R11065 3" low-background, high-quantum-efficiency PMTs, nineteen each on the top and the bottom. A cut-away view of of the TPC is given in Fig. 2.15. When warm, the cylindrical region is 35.6 cm in diameter and 35.6 cm in height (h_{drift}).

Thanks to LAr density of $\rho_{LAr} = 1394\,\mathrm{kg}\cdot\mathrm{m}^{-3}$ (data from [102]) this gives an active mass when cold of $46.4 \pm 0.7\,\mathrm{kg}$, where the uncertainty is primarily in the thermal contraction of the PTFE.

All the 38 PMTs are submerged in liquid argon and view the active mass through fused-silica windows, which are coated on both faces with transparent conductive indium tin oxide (ITO) films 15 nm thick. This allows the inner window faces to serve as the grounded anode (top) and the above-mentioned −HV cathode (bottom) of the TPC, while maintaining their outer faces at the average PMT photocathode potential.

The fused silica anode window has a cylindrical rim extending downward to form the "diving bell" that holds the 1 cm-thick vapor layer (H_{elect}), produced by boiling argon within the cryostat (outside the TPC active volume) and delivering the gas to the diving bell. The vapor then exits the bell via a bubbler that maintains the LAr/vapor interface at the desired height. The grid, 5 mm (H_{extr}) below the liquid surface from which can be extract electrons, is a hexagonal mesh etched from a 50 µm-thick stainless steel foil and has an optical transparency of 95 % at normal incidence.

The electron drift system consists of the ITO cathode and anode planes, a field cage, and the grid that separates the drift and electron extraction regions. A voltage V_{drift} is applied between the cathode and grid to produce the drift field E_{drift}, which nominal value is merely:

$$E_{drift} = V_{drift}/H_{drift} \tag{2.20}$$

Outside the cylindrical PTFE wall, copper rings at graded potentials keep

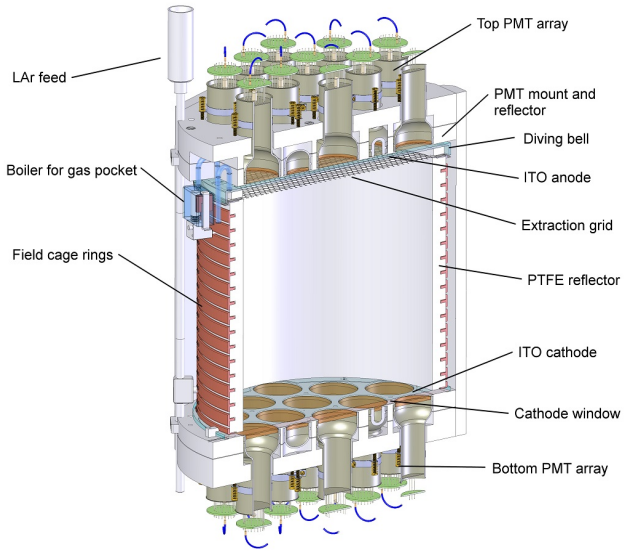

Fig. 2.15: The DarkSide-50 Liquid Argon Time Projection Chamber.

the drift field uniform throughout the active volume. The relative voltages on the individual rings are determined by resistors connecting each adjacent ring, forming a large voltage divider chain. After the results of the SCENE experiment which, as saw in sec.2.2.1, uncovered a drift-field-induced quenching of the S1 light yield for nuclear recoils, the standard fields configuration was set with a $-12.7\,\mathrm{kV}$ cathode potential and a $-5.6\,\mathrm{kV}$ grid potential, giving nominal drift electric fields of $200\,\mathrm{V\,cm^{-1}}$[9]. With these values the maximum drift time in the active volume is $373\,\mu\mathrm{s}$, and the measured value of the drift speed is $0.93 \pm 0.01\,\mathrm{mm\,\mu s^{-1}}$.

An independently-adjustable potential between the grid and anode creates the extraction and electroluminescent fields. The extraction field E_{extr}, the electroluminescent field E_{elect} and the potential V_0 between the grid and anode are related

[9] The graded potentials of the field cage rings were chosen to produce a uniform field with 1000 V/cm drift field and 2.8 kV/cm extraction field. With the 200 V/cm drift field, the field cage is no longer optimized and the stream lines are "pushed" inward at the top of the TPC due to leakage of the extraction field through the grid. However, due to charge buildup on the PTFE walls, the drift field is likely uniform throughout[103].

via:

$$\begin{cases} E_{extr} = \frac{\epsilon_{vap}}{\epsilon_{liq} H_{elect} + \epsilon_{vap} H_{extr}} \cdot V_0 \\ E_{elect} = \frac{\epsilon_{liq}}{\epsilon_{liq} H_{elect} + \epsilon_{vap} H_{extr}} \cdot V_0 \end{cases}, \tag{2.21}$$

where $\epsilon_{rel} = \epsilon_{liq}/\epsilon_{vap}$ and ϵ_{liq}, ϵ_{vap} are the dielectric constants of liquid and vapor argon respectively[10]. From eq. 2.21 we can write:

$$E_{elect} = \epsilon_{rel} \cdot E_{extr}. \tag{2.22}$$

As reported in Tab. 2.1 the dielectric constant of liquid argon ϵ_{liq} is 1.53 at T_b, while for gaseous argon ϵ_{gas} is 1.00 at 273 K and at standard atmospheric pressure. Although under different temperature and pressure, ϵ_{vap} in vapor is believed to still be extremely close to one, so ϵ_{rel} is commonly written as $\epsilon_{rel} = \epsilon_{liq}/\epsilon_{vap} \sim 1.5$, and also:

$$E_{elect} = 1.5 \cdot E_{extr}. \tag{2.23}$$

With the above reported potentials and distances the extraction and electroluminescence fields are $2.8\,\mathrm{kV\,cm^{-1}}$ and $4.2\,\mathrm{kV\,cm^{-1}}$, respectively.

The grid and cathode voltages are transferred from DC high voltage power supplies, in a cleanroom above the WCD, to inside the detector via custom made feedthroughs. The basic design of each HV feedthrough is a stainless steel conductor press fitted into a UHMW polyethylene tube, which is surrounded by a grounded stainless steel shield tube. The feedthrough must be able to hold HV while holding ultra high vacuum. The leak tight seal between the polyethylene

[10] It is worth noting that these relations are obtained by considering the grid as a perfect conductor, so that the system composed by the grid, the liquid-vapor interface and the cathode could be considered as made by two in series capacitors. This approximation depends on mesh size of the grid and on relative applied potentials, and also affect E_{drift}.

and outer ground shield is achieved by a "cryofit" procedure. The grounded tube extends from the cyostat flange through the gaseous argon to below the liquid surface. The ground tube keeps the electric fields due to the HV conductor well contained and prevents charge buildup on any surfaces in the gaseous argon, which has a low breakdown point. On the other hands the liquid has a high breakdown point (hundreds of kV/cm [104]), so it can tolerate much higher electric fields.

The reflector and the windows at the top and bottom of the cylinder are coated with TPB wavelength shifter, that absorbs the 128 nm scintillation photons emitted by liquid argon and re-emits visible photons (peak wavelength 420 nm) that are reflected, transmitted, and finally detected with high efficiency by PMTs.

Cooling of the cryostat is done using an external circulation loop. The loop cooling power is controlled to maintain a stable pressure in the cryostat around the set point of 1080 mbar ($\sim$ 15.66 psi).

3. THE RED -RECOIL DIRECTIONALITY- EXPERIMENT

ReD (Recoil Directionality) is an experiment within the DarkSide Collaboration. The main aim is to study nuclear recoils in liquid argon by detecting neutron-nucleus interactions in the recoil energy range expected in WIMP-Ar interactions (from $\mathcal{O}(1\,\mathrm{keV_{NR}})$ up to about $120\,\mathrm{keV_{NR}}$). As already mentioned a specific task is to explore the possible directional dependence as suggested by the SCENE experiment (see sec. 2.2.5). Moreover in ReD are implemented more of DarkSide-20k TPC future solutions, as the non cylindrical form, the Silicon Photomultiplier instead of PMT or acrylic windows instead of fused silica and again. So ReD is also part of DarkSide-20k R&D program.

The ReD experiment was located at Laboratori Nazionali del Sud (LNS), Catania, in the "80 deg" beamline, since June 2018. It consists of a rather complex experimental apparatus that can be conceptually divided into three parts. The first part includes everything related to the production of neutrons via $p(^7\mathrm{Li}, n)^7\mathrm{Be}$ reaction in CH_2 targets and the tagging of the associated charge particle (^{7}Be), tanks to a double Si detector coupled in a ΔE/E telescope. The second part, the heart of the experiment, consists of an almost cubic LAr TPC, of $125\,\mathrm{cm}^3$ active volume, able to detect and discriminate the argon recoils generated by produced neutrons, and the ancillary cryogenic system for the argon liquefaction and recirculation. Finally, the third part is a n-spectrometer with nine 3"x3" liquid scintillator cells (LiSci) coupled to 3" photomultipliers (PMTs). Eight

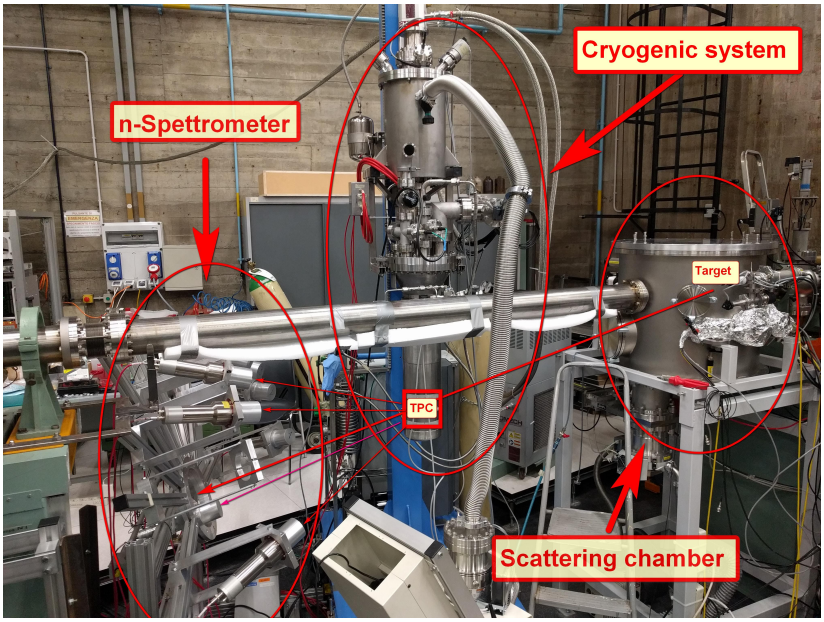

Fig. 3.1: Photo of the "80 deg" beamline at LNS, after the deployment and alignment of ReD. The targets and the Si telescope are hosted inside the vacuum scattering chamber while the LAr TPC is inside the dewar.

LiSCis are placed to tag recoiling nuclei having the same energy, i.e. the same scattering angle with respect to the incident neutron, but different angle with respect to the drift field of the LAr TPC, thus allowing to search for a possible directional response. The ninth LiSCi is placed in a position to tag low energy Ar recoils with $E_R \sim \mathcal{O}(1\,\mathrm{keV_{NR}})$. More details on this topics will be given in the following sections.

All these parts are positioned according to a precise geometry, necessary to tag energy and angular recoil conditions. In Fig. 3.1 a lateral view of the whole apparatus at LNS is shown after the deployment and alignment.

3.1 Geometry

ReD geometry is studied to intercept diffused neutrons which produce argon recoiling nuclei at specific recoil energy and specific angle of argon with respect to the drift electric field, θ_R. In Fig. 3.2 a sketch of the conceptual geometry of the

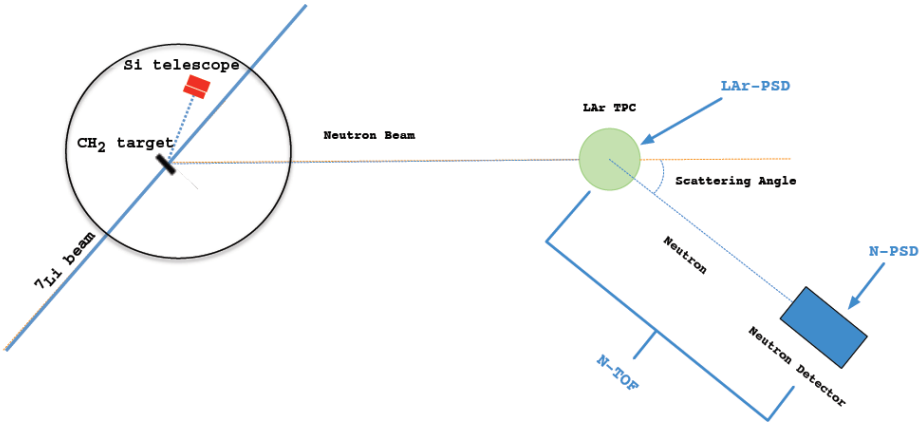

Fig. 3.2: A simple conceptual sketch of the geometry of the experiment.

experiment is represented.

In order to achieve argon scattering parallel to the drift field ($\theta_R = 0°$), a vertical dislocation between the CH_2 target, where neutrons are generated, and TPC is necessary. Moreover, clearance around the ^{7}Li beam was a constraint for the cryogenic apparatus and the n-spectrometer too. Finally, the LiSci angular aperture can compromise energy and angular resolution (see sec. 3.6.1 for more details). As an optimal compromise between clearance, acceptance and resolution we chose:

- distance from CH_2 target to TPC: $D_{(CH_2\,|\,\mathrm{TPC})} = 150\,\mathrm{cm}$
- distance from TPC to LiSCi: $D_{(\mathrm{TPC}\,|\,\mathrm{LiSCi})} = 80\,\mathrm{cm}$
- angle between the vector from CH_2 target to TPC and an horizontal plane: $\theta_{\mathrm{TPC}} = 18.4°$ (note that θ_{TPC} puts the TPC under the horizontal plane containing the ^{7}Li beam line)
- angle between the vector from CH_2 target to TPC and the vertical plane containing ^{7}Li beam line: $\phi_{\mathrm{TPC}} = 12.8°$

With $\theta_{\mathrm{TPC}} = 18.4°$ and $\phi_{\mathrm{TPC}} = 12.8°$, the angle between the vector from

CH_2 target to TPC and ^{7}Li beam direction becomes $\theta_n \simeq 22.3°$. It is worth noting that θ_n is the mean angle of the emerging neutron with respect to the ^{7}Li beam in the $p(^7\mathrm{Li}, n)^7\mathrm{Be}$ reaction. If the ^{7}Li beam energy is defined, the neutron energy depends only by θ_n.

Moreover with $\theta_{\mathrm{TPC}} = 18.4°$ from kinematics constraints the only angle at which we can obtain argon scattered parallel to the drift field ($\theta_R = 0°$) is

$$\theta_3 = 36.8° \tag{3.1}$$

This is the angle at which eight of the nine LiSCis are located with respect to target-to-TPC direction. In Fig. 3.3 a sketch of vertical and horizontal views is shown.

As reported in sec 3.6.1, if the neutron energy is fixed then the "scattering angle" θ_3 defines the energy of the recoiling nuclei. The ninth and final LiSCi has $\theta_3 = \theta_{3 Low E_R}$[1]

$$\theta_{3 Low E_R} = (4.3 \pm 0.1)° \tag{3.2}$$

to tag low energy scattering recoiling nuclei, with $E_R \sim \mathscr{O}(1\,\mathrm{keV_{NR}})$ (for more details see sec. 3.6.1).

3.2 The Neutron Beam at LNS: $p(^7\mathrm{Li}, \mathrm{n})^7\mathrm{Be}$ reaction and ^{7}Be tagging

To produce neutrons at LNS we chose the planar reaction:

$$^7\mathrm{Li} + \mathrm{p} \rightarrow ^7\mathrm{Be} + \mathrm{n} \qquad (\mathrm{Q} = -1.644\,\mathrm{MeV} - \mathrm{Threshold} = 13.098\,\mathrm{MeV}) \tag{3.3}$$

[1] This angle is not kinematically calculated, like the other angles in this section. It is obtained from measures.

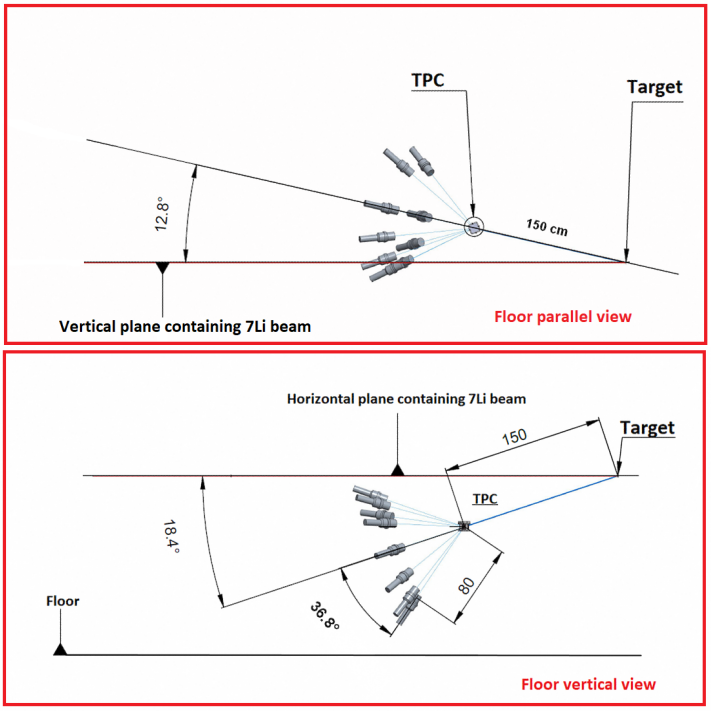

Fig. 3.3: Sketch of vertical and horizontal views.

With a reaction in inverse kinematics, where the projectile is much heavier than the target, as ^{7}Li with respect to p, it is possible to have a natural collimation of the produced neutrons [105]. At the LNS, using the Tandem accelerator, it is possible to produce a ^{7}Li primary beam with energies up to 56 MeV. This allows to have neutrons of different mean energies. At these high energies new outgoing channels can be obtained, such as the production of the recoil ^{7}Be nucleus in its first excited state ^{7}Be* at 0.429 MeV and ^{7}Li beam at an energy threshold at only 16.513 MeV. During June, July and September 2018 data taking the ^{7}Li energy was 28 MeV, and we plan in the future not to go beyond 35 MeV. In table 3.1 information on the open reaction channels for ^{7}Li beam energy up to 50 MeV are given.

The ^{7}Li beam produced by Tandem is collimated and send to the scattering chamber, where it hits a CH_2 target to produce neutrons . The chamber contains a plate holder that can be moved from outside without breaking the void. This

Exit channel	Q-value [MeV]	Threshold energy [MeV]	Primary 0° n-energy [MeV]
$n_0 + {}^7_4\mathrm{Be}$	-1.644	13.098	1.44
$n_1 + {}^7_4\mathrm{Be} * (0.429\mathrm{MeV})$	-2.073	16.513	3.84
$n_2 + {}^3_2\mathrm{He} + {}^4_2\mathrm{He}$	-3.230	25.726	8.18
$n_3 + {}^7_4\mathrm{Be} * (4.57\mathrm{MeV})$	-6.214	49.489	18.79

Tab. 3.1: Main characteristics of the $p({}^7\mathrm{Li}, n){}^7\mathrm{Be}$ reaction. Neutrons produced in each channel are labeled n_i to indicate they are produced with different kinematics. Data from [105]

allows to change the type and thickness of the target. During June and July data taking we used a series of CH_2 targets with surface density from $\rho_{Surf} = 172\mu g/cm^2$ up to $\rho_{Surf} = 244\mu g/cm^2$, and a gold target to use elastic ${}^7\mathrm{Li}/{}^{77}\mathrm{Au}$ scattering reaction for possible Si $\Delta E/E$ telescope calibration (Fig. 3.5 to the left). The intensity of the ${}^7\mathrm{Li}$ beam impinging on the target after the collimator is measured by a Faraday Cup installed at the far end of the beam pipe.

As the Tandem cannot be operated in pulse mode, produced neutrons must be tagged event by event using kinematics. This can be done by detecting the angle and the energy of ${}^7\mathrm{Be}$ produced along with the neutron in the reaction. Moreover the detection of ${}^7\mathrm{Be}$ provides the start for a time-of-flight measurement of the scattered neutron. With this purpose within the scattering chamber, at about 47 cm from the target and mean angular position of about 5 degrees from the beam line (CH_2 target as vertex), the above mentioned Si $\Delta E/E$ telescope is placed. It consist of two different detectors by ORTEC [106], one behind the other. In the Si $\Delta E/E$ telescope, the loss of energy and the total energy of the incident particle are measured when particles with kinetic energy E_0 pass through the first thin detector ($20\,\mu$m) and are stopped in the second one ($200\,\mu\mathrm{m}^2$). The energy subdivision between the two detectors is different for different particles and different

[2] From September 2018 to improve energy resolution the thickness of the second one is $1000u$m.

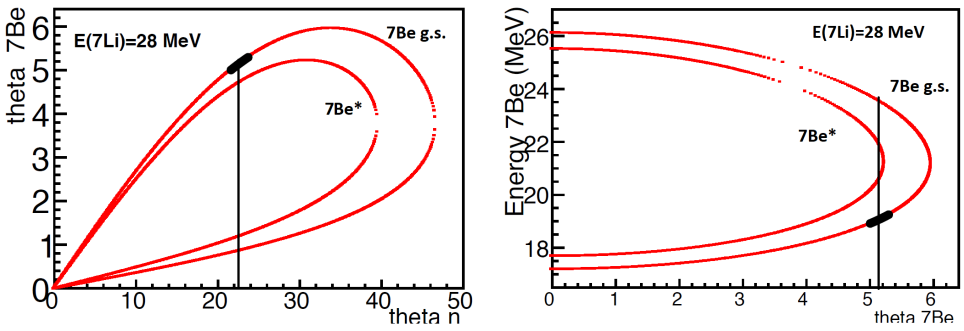

Fig. 3.4: Left Allowed kinematics $p(^7\mathrm{Li}, n)^7\mathrm{Be}$ reaction solutions for E_{Beam}= 28 MeV, with TPC angular position ($\theta_n \simeq 22.3°$), highlighted by the vertical line. *Right* Only one ^{7}Be g.s. *locus* has emerging neutrons with correct $\theta_n \simeq 22.3°$, while the other *locus* results as background for $\Delta E/E$ telescope, as also ^{7}Be*

energies, because of the different stopping power. Accordingly different particles and also same particles with different energies, will be able to populate different zones in the $(E; \Delta E)$ plane. This allows for particle identification or energy determination. Thus the $\Delta E/E$ telescope allows to discriminate the charged products of the beam-target reactions, i.e. the main ^{7}Li band due to elastic scattering on p and C in CH_2 target, the two ^{7}Be *loci* corresponding to the two solutions allowed by kinematics as also ^{7}Be*. In Fig. 3.4 (left side) it is shown the allowed kinematics $p(^7\mathrm{Li}, n)^7\mathrm{Be}$ reaction solutions for $E_{Beam} = 28$ MeV, with TPC angular position ($\theta_n \simeq 22.3°$) highlighted by the vertical line. As can be seen, the $\Delta E/E$ telescope at about 5° intercepts two ^{7}Be g.s. *loci* as also ^{7}Be*. Moreover by comparing the two images in Fig. 3.4, you can see that only one ^{7}Be g.s. *locus* has emerging neutrons with correct $\theta_n \simeq 22.3°$, while the other *locus* results as background for the TPC, as also ^{7}Be*.

In front of the $\Delta E/E$ telescope there is a 2 mm thick aluminium collimator with a 3 mm diameter hole, of a set prepared to tag emerging neutrons angle (see Fig.3.5 on the right). This last collimator is useful to reduce the rate on Si detector from particle that do not tag neutrons in TPC angular position, enabling for

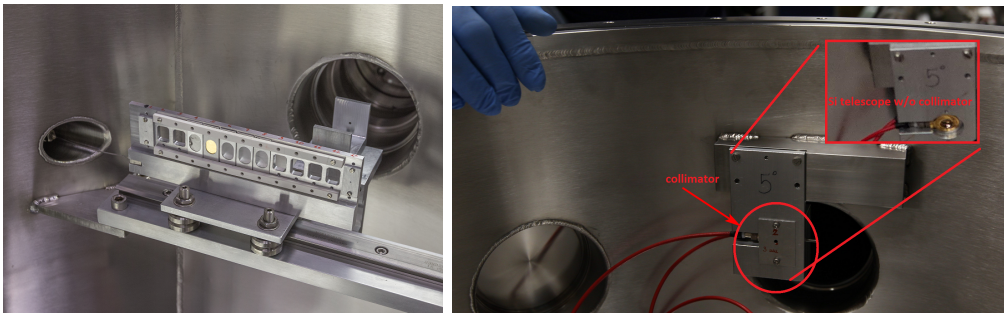

Fig. 3.5: Left The target holder that can be moved from outside without breaking the void. Different CH_2 targets can be seen as the gold target for elastic (^{7}Li,^{77}Au) scattering. *Right* The 2 mm aluminum thick (3 mm hole diameter) collimator in front of the $\Delta E/E$ telescope. In the insert the $\Delta E/E$ telescope without the mentioned collimator.

higher I_{Beam}(I_{Beam}intensity is limited by maximum rate that Si $\Delta E/E$ detectors can sustain). Conversely even a decimal angular misalignment of the collimator can determine a strong misalignment with respect to the TPC position in the tagged neutrons, resulting in a reduction in Si-TPC coincidence rate events. If we define:

- $\alpha :=$ ^{7}Be angular position (which corresponds to aluminum collimator angular position), and $T_{^7Be} :=$ ^{7}Be kinetic energy
- $\beta :=$ emerging neutrons angular position (which corresponds to TPC angular position), and $T_n :=$ neutron kinetic energy

where kinetic energies directly depend on ^{7}Li E_{Beam}, then we get (in the non relativistic limit):

$$\delta\beta \cos\beta \simeq \sqrt{\frac{m_{^7Be}\, T_{^7Be}}{m_n\, T_n}} \cos\alpha\, \delta\alpha \Longrightarrow \delta\beta \simeq 4.6\, \delta\alpha \tag{3.4}$$

where the value to the right is for E_{Beam}= 28 MeV, $\alpha = 5$ deg and $\beta = 22.3$ deg. Moreover using $D_{(CH_2|TPC)} = 150$ cm (the distance from CH_2 target to TPC), from the last result using $\delta\alpha = 0.1$ deg we get about 1.1 cm dislocation of emerging tagged neutrons, that can result in a misalignment for a TPC of only 5x5x5 cm^3

active volume.

3.3 The ReD TPC

The core detector of ReD is a small custom-made double phase LAr TPC designed and built by UCLA group. As said, inside the DarkSide Program ReD is also useful to do R&D for the DarkSide-20k experiment. So a lot of new features that will be adopted in DarkSide-20k are being tested in the ReD TPC. For example the TPC is a cuboid rather than a cylinder as usually used (the DarkSide-20k TPC will be in octagonal shape): the external dimensions are 9x9x9 cm^3 cube, while the inner part is a 5x5x6 cm^3 cuboid (5x5x5 cm^3 active volume). Moreover, as DarkSide-20k needs to get rid of the conventional PTFE-reflector (as said still in use in DarkSide-50), which would be the predominant source of neutron background and Cherenkov background due to the enormous mass required in DarkSide-20k, the Enhanced Specular Reflector (ESR) foil will be used as the TPC reflector for DarkSide-20k, and so for the ReD TPC. ESR is a thin layer foil which has reflectivity for 420 nm light, up to 98 %, with a thickness of only 65 μm. To hold the ESR foil in place and maintain its flatness during the operations, two pieces of UV-Transmitter acrylic sheets are needed to sandwich the ESR foil in the middle. Accordingly the ReD TPC inner part is laterally enclosed by vertical acrylic-ESR sandwich reflection panels on the four sides. Another detail shared with DarkSide-20k are acrylic windows on the top and bottom of the inner part instead of fused silica windows. These acrylic windows are coated on both side by 25 nm thick ITO: the side facing to the active LAr volume to work as anode on the top and cathode on the bottom, while the other sides to ground the surface near SiPMs and Front End Boards (FEBs). In order to maximize the TPC scintillation

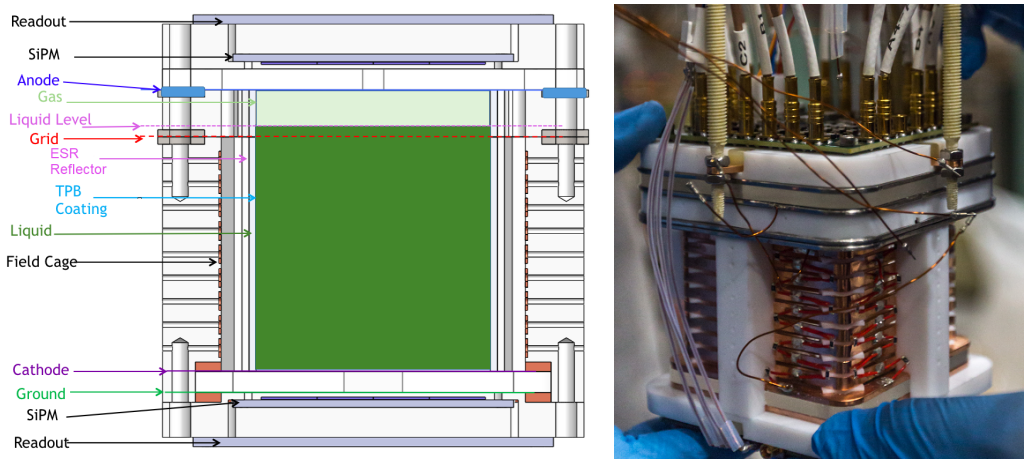

Fig. 3.6: Left: ReD TPC scheme. *Right*: ReD TPC picture take during assembly at LNS. You can see the field cage rings and on the top the 24-single-channel readout via the 24-channel FEB.

light yield (LY), the entire inner surface of the TPC is TPB coated, that is all the reflection panels (in both drift region and vapor region) and top and bottom windows (only on the surface facing to the active volume) are coated in a range from 160 $\mu g/cm^2$ up to 200$\mu g/cm^2$ of TPB.

The maximum drift length is 5 cm, delimited by the cathode and by a stainless steel grid, a hexagonal mesh etched from a 50 µm-thick stainless steel foil. It has an optical transparency of 95 % at normal incidence and is located 3 mm below the level of the liquid. The drift field is shaped by ten copper rings fixed on the Teflon pillars which make up the structure of the TPC. A 7 mm-thick gas pocket is formed by means of a "diving bell", which is located above the stainless steel grid and is closed on the top by the anode window. A separate "boiling chamber" is connected to the "diving bell" so that using a pt1000 as resistor, the gas pocket can be generated via joule effect. An hole on the other side with respect to the "boiling chamber", maintains the liquid level at the correct height. In Fig. 3.6 on the left a ReD TPC scheme is shown.

Another innovative feature implemented in ReD TPC that will be shared with

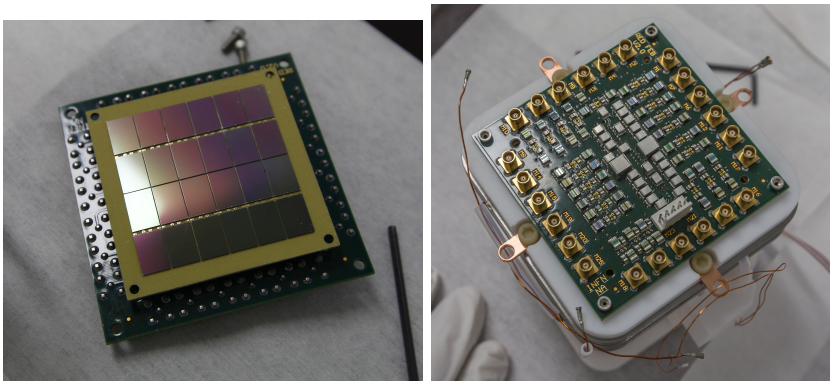

Fig. 3.7: Left A 24 SiPMs tile mounted on the 24-channels readout FEB. *Right* The 24 channels FEB designed and produced by INFN-Na in collaboration with INFN-Bo and LNGS, mounted on the TPC.

DarkSide-20k, is the optoelectronic readout based on Silicon Photomultipliers (SiPMs) developed by Fondazione Bruno Kessler (FBK [107]) and part of the cryogenic electronics. Two 5x5 cm^2 tiles are available from FBK, each made by 24 rectangular 11.7x7.9 mm^2 SiPMs. These SiPMs had never been tested before and have some minor differences from those that will be used in DS20k. In fact they have a cell pitch of 25 μm and a quenching resistor of 10 MΩ (@ 77 K, LN temperature), instead of 30 μm and 5 MΩ. Moreover the tile substrate is made by Arlon, which is a possible solution under study for DarkSide-20k. The tile on the top of the LAr TPC has a 24-single-channel readout, in order to improve the (x;y) sensitivity, while the bottom tile has a 4-summed-channel readout. For the top readout a dedicated 24-channel front end board (FEB - Fig. 3.7) has been designed and produced by INFN-Na in collaboration with INFN-Bo and LNGS. It is based on a recent work on the development of a very low-noise cryogenic pre-amplifier for large-area SiPM devices [108], to be directly coupled to the tile to deal out the HV supplies to SiPM's and to amplify one-by-one the 24 signal channels.

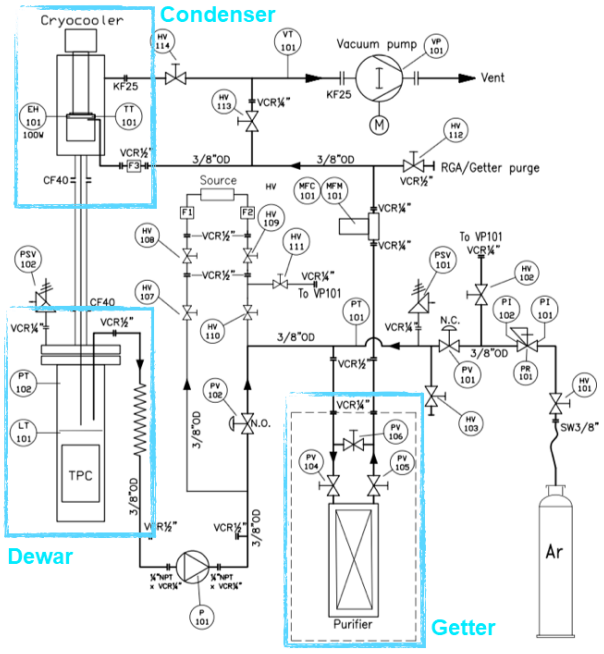

Fig. 3.8: Working scheme of the cryogenic system

3.3.1 Cryogenic system

The TPC is housed in a specially designed cryogenic system (Fig. 3.8), developed by the Criotec company [109], through which it is possible to liquefy, purify and recirculate the argon. The system is composed of a double wall cylindrical dewar to contain the TPC immersed in liquid argon and a condenser separated above the dewar capable of liquefying argon gas through a helium compressor made by CryoMech [110]. The whole structure was designed and built to minimize background neutron interactions, especially in stainless steel walls of the cylindrical dewar as in LAr around the TPC. Which is why the condenser is separated from the dewar. Always for the same reason the dewar inner diameter is only $\simeq 13\,\mathrm{cm}$ (the minimum necessary to accommodate the TPC), while the thickness of its two walls, where the TPC is inserted, is only $0.7\,\mathrm{mm}$.

The Cryomech compressor is connected to a pulse tube which in turn is coupled with a "CryoMech PT90" cold copper head. In filling mode the ultra-high purity

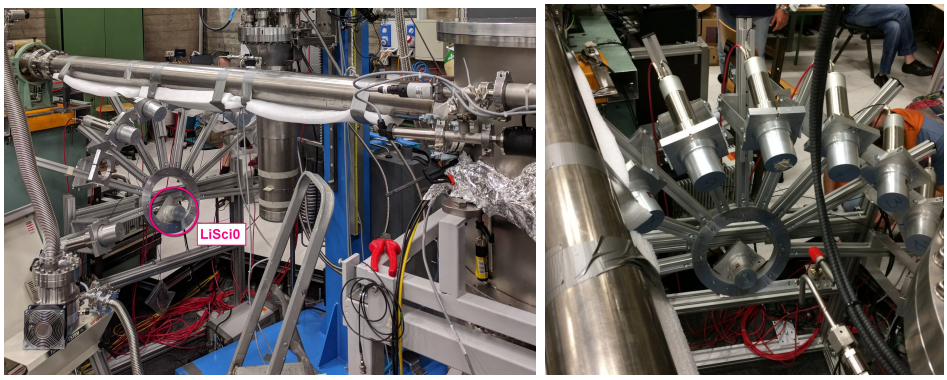

Fig. 3.9: The n-Spectrometer.

6.0 argon gas is gradually introduced into the system at room temperature, enters the condenser cell where it is cooled by contact with the cold head and is then passed by gravity into the dewar. In this way, by circulating gas at an increasing lower temperature, the whole system is cooled until the beginning of the actual liquefaction phase. Once the liquid dewar is filled, it is recycled: the argon gas boils and evaporates, the gas is collected and purified through a SAES getter [111], then liquefied again. This process takes place at equilibrium, whereby the level of liquid argon remains constant and so does the pressure inside the dewar.

3.4 The n-Spectrometer

A specially designed n-Spectrometer (Fig. 3.9), with nine 3"x3" EJ-309 organic liquid scintillators coupled with ET-9821B PMTs, is used to intercept diffused neutrons in the TPC. EJ-309 is commonly employed for fast neutron detection thanks to its high PSD capability and fast signal response ($\sim$ few ns), making it suitable for time of flight (TOF) measurements at nanosecond level.

Eight of the nine LiSCis (from now $\text{LiSCis}_{1/8}$) are located on a geometrical circumference, base of a right cone with vertex at the TPC geometrical center, axis target- to-TPC direction and opening angle twice the $\theta_3 = 36.8°$ scattering

Ar/$\mathcal{E}_{\text{drift}}$-angle θ_R [deg]	n-scattering angle θ_3 [deg]	LiSCi azimuthal angle ϕ_{LiSCi} [deg]	TPC-LiSCi distance $D_{(\text{TPC}\,\vert\,\text{LiSCi})}$ [cm]
90	36.8	83.6 276.4	80
60	36.8	116.4 (243.6 - not used)	80
40	36.8	137.7 222.3	80
20	36.8	158.9 201.1	80
0	36.8	180.0	80
LiSCi0	—	—	—
—	4.3	0.0	97

Tab. 3.2: LiSCis positions in the n-Spectrometer. See text for details.

angle. The axis of $\text{LiSCis}_{1/8}$ point to TPC center and, as said, the distance from $\text{LiSCis}_{1/8}$ to TPC is 80 cm (from center to center). So all eight $\text{LiSCis}_{1/8}$ scintillators intercept neutrons with the same $\theta_3 = 36.8°$ scattering angle, which means the same Ar recoil energy. On the other hand, each one of the eight $\text{LiSCis}_{1/8}$ tags a different θ_R, the nuclear recoil angle with respect to the drift field.

The ninth and final LiSCi (from now LiSCi0) intercepts neutrons with $\theta_3 = 4.3°$ geometrical scattering angle (TPC center to LiSCi center), then it tags low energy Ar recoiling nuclei (for more details see sec. 3.1), while the distance from TPC is at about 97 cm (center to center). For the LiSCi0 is useful to report that the angle target-LiSCi0 vs target-TPC is about 1.7 deg. As it will be more clear later, this means that LiSCi0 is inside the cone of neutrons tagged by Si-telescope, which have 2 deg angular diameter.

To tag Ar recoiling nuclei at specific recoil energy and specific recoil angles with respect to the drift field, the $\text{LiSCis}_{1/8}$ azimuthal angular positions must be

properly set (see sec.s 3.1 and 3.6.1 for more details). In Tab. 3.2 LiSCis angular positions, set in the n-Spectrometer for the different θ_Rs that we chose to test for LAr recoil directionality, are reported. The angular positions are azimuthal angles -ϕ_{LiSCi}- around target-TPC direction; $\phi_{LiSCi} == 0°$ corresponds to the lower position (that one closer to the floor) of the two possible positions in the vertical plane containing the target-TPC direction. Double solutions for ϕ_{LiSCi} come from left-right symmetry in the system geometry, although this two solutions overlap for $\theta_R = 0°$. We chose to use this symmetry using both solutions (with the exception for $\theta_R = 120°$) to disentangle systematics in the data.

3.5 Trigger and data acquisition

The optimal trigger condition to select Ar recoil directionality would require a triple coincidence between Si-telescope trigger, the TPC trigger and a trigger from one of eight $\text{LiSCis}_{1/8}$'s PMTs. Instead, two double coincidence trigger schemes have been applied so far: "Si-telescope AND TPC" (Si-TPC trigger) or "Si-telescope AND any PMT" (Si-PMT trigger). This choice comes also, but not only, from the necessity to better understand the response of detectors coupled two by two, particularly after the failure in rates as tested from the start of data acquisition at LNS in June (more in sec. 4.2). Moreover Si-PMT trigger scheme, which yields a large fraction of accidentals due to the large single rate of the PMTs (kHz), gives potential access to low-energy recoil in the TPC, events not seen by the TPC trigger (essentially no S1 scintillation is generated at energies $\sim \mathcal{O}(1\,\text{keV}_{\text{NR}})$). In addition to the coincidence events, we take runs with events triggered by one of the three detectors alone, the Si-telescope, the TPC and the PMTs, to make calibrations or take backgrounds.

The data acquisition system (DAQ) is based on three 16 ch, 14-bit resolution, $2\,V_{pp}$ input range, Flash ADC boards CAEN V1730 at 500 MHz sampling rate [112], which record waveforms from the Si-telescope, the TPC and the PMT coupled to LiSCis. When the TPC is operated without S2 production (i.e. with zero anode voltage), the digitizer records is set to 10 k samples ($20\,\mu$s) long including 3 k samples ($6\,\mu$s) before the hardware trigger (used to establish the baseline). When the TPC is operated with S2 production the length of the digitizer records is set 50 k samples ($100\,\mu$s) long including 5 k samples ($10\,\mu$s) before the hardware trigger (as before, used to establish the baseline). The data were recorded using the PadMe-ReD data acquisition system [113]. An on purpose made "red-daq-light" analysis software is used, which includes analysis modules to convert binary digitizer data to root [114] tree, apply single photo-electron response (SER) calibration, combines the waveforms of the top/bottom SiPMs channels into a single waveform, identifies the start time for S1 and S2 signals, evaluate f_{prompt} in the waveforms and so on.

3.6 Some preliminary estimates

3.6.1 Kinematics and energy uncertainty of n - ^{40}Ar scattering

Neutrons at LNS are generated by $p(^7\mathrm{Li}, n)^7\mathrm{Be}$ reaction. Even with ^{7}Li energy up to 35 MeV (the maximum E_{Beam} we plan to use), with the geometrical setup used at LNS, we get $E_n \leq 10\,\mathrm{MeV}$, beeing E_n the neutron energy (see Fig3.10 on the top). Furthermore with $E_n = 10\,\mathrm{MeV}$ you get $\beta = \frac{v_n(E_n=10\,\mathrm{MeV})}{c} \sim 1 \times 10^{-2}$, where v_n is the neutron velocity and c the light velocity respectively. The non relativistic limit is therefore applicable in kinematics calculations for the elastic

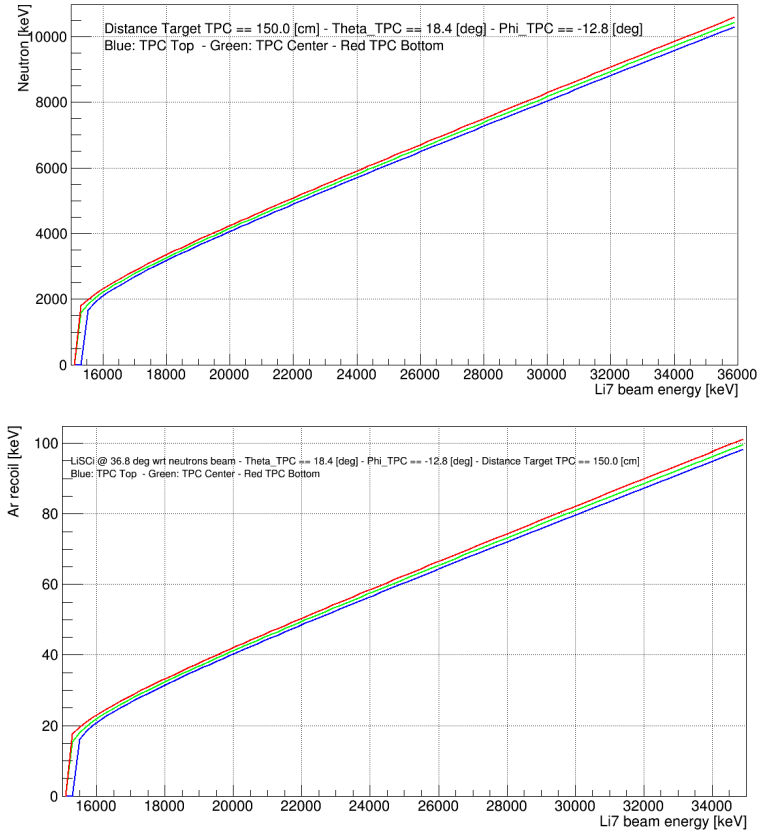

Fig. 3.10: Kinematics behaviors of neutron and ^{40}Ar vs ^{7}Li beam energy for $p(^{7}\mathrm{Li}, n)^{7}\mathrm{Be}$ reaction, calculated with geometric settings used at LNS in June and July runs. Different curves refers to Center (green), Top (blue) and Bottom (red) geometrical points in the TPC. *Top* Neutron energy E_n vs ^{7}Li beam energy. *Bottom* ^{40}Ar recoil energy vs ^{7}Li beam energy.

scattering:

$$n + {}^{40}\mathrm{Ar} \rightarrow \mathrm{n} + {}^{40}\mathrm{Ar} \qquad \text{(elastic)} \tag{3.5}$$

Using:

- $E_R :=$ recoil energy
- $\theta :=$ neutron scattering angle wrt incoming direction
- $A := \frac{M_{Ar}}{M_{neutron}} \simeq 40$
- $E_n :=$ incoming neutron energy

in this limit, we get:

$$E_R = E_n \cdot \frac{2}{(A+1)^2} \cdot (A + sin^2\theta - cos\theta\sqrt{A^2 - sin^2\theta}) \tag{3.6}$$

Thanks to $sin^2\theta/A \ll 1$ eq. 3.6 may be written:

$$E_R \simeq E_n \cdot \frac{2A}{(A+1)^2} \cdot (1 - cos\theta) \tag{3.7}$$

Anyway, if you put $\theta = 36.8°$ and $E_n \simeq 7.4\,\mathrm{MeV}$ in eq. 3.6, respectively the LiSci position angle and neutron energy at LNS during June and July run, we get:

$$E_R(\theta = 36.8°; E_n = 7.4\,\mathrm{MeV}) \simeq 73\,\mathrm{keV} \tag{3.8}$$

which is the kinematically expected nuclear recoil energy (see Fig3.10 on the bottom).

The finite size of the TPC and diameter of the external neutron counter will induce an uncertainty $\delta\theta$ in the scattering angle θ, which will induce an uncertainty in the measured recoil energy.

More in details, eq. 3.7 differentiated becomes[3]:

$$dE_R = E_n \cdot \frac{2A}{(A+1)^2} \cdot (sin\theta) \cdot d\theta \tag{3.9}$$

If we consider the uncertainty on the angle arising only from the angular

[3] For simplicity here I consider delta as a differential.

dimension of scintillators[4], with radius of 3" = 7.62/2 cm, you get

$$d\theta = \frac{7.62/2\text{cm}}{80\text{cm}} \simeq 5\% \tag{3.10}$$

where 80 cm is TPC center to LiSci center distance.

So using eq. 3.9 and eq. 3.10 we obtain:

$$\begin{aligned} dE_R &\simeq E_n \cdot \frac{2A}{(A+1)^2} \cdot (sin\theta) \cdot 5\% \\ &= 0.24\% \cdot (sin\theta) \cdot E_n \end{aligned} \tag{3.11}$$

Finally if we use $\theta = 36.8°$, which as said is the LiSci position angle of LNS June and July runs, we get:

$$dE_R \simeq 0.14\%\, E_n \tag{3.12}$$

Moreover for the ^{7}Li energy beam used in June and July runs, $E_{Beam} = 28\,\text{MeV}$, we get:

$$dE_R \simeq 0.14 \cdot 7\,\text{MeV} \simeq 10\,\text{keV} \tag{3.13}$$

Generally it is more indicative to consider the relative ^{40}Ar recoil energy uncertainty which, using 3.7 and 3.9, can be written:

$$\frac{dE_R}{E_R} = \frac{(sin\theta)}{(1-cos\theta)} \cdot d\theta = cotan(\frac{\theta}{2}) \cdot d\theta \tag{3.14}$$

If, as for absolute energy uncertainty, we consider $d\theta$ as constant, namely arising only from angular dimension of scintillators 3.10, it is possible to study relative uncertainty induced on the recoil energy as a consequence of the uncertainty in

[4] This is an underestimate, it should be consider the interactions position distribution in the TPC. However any in this simple way we can estimate orders of magnitude of energy uncertainty vs LiSCi angles.

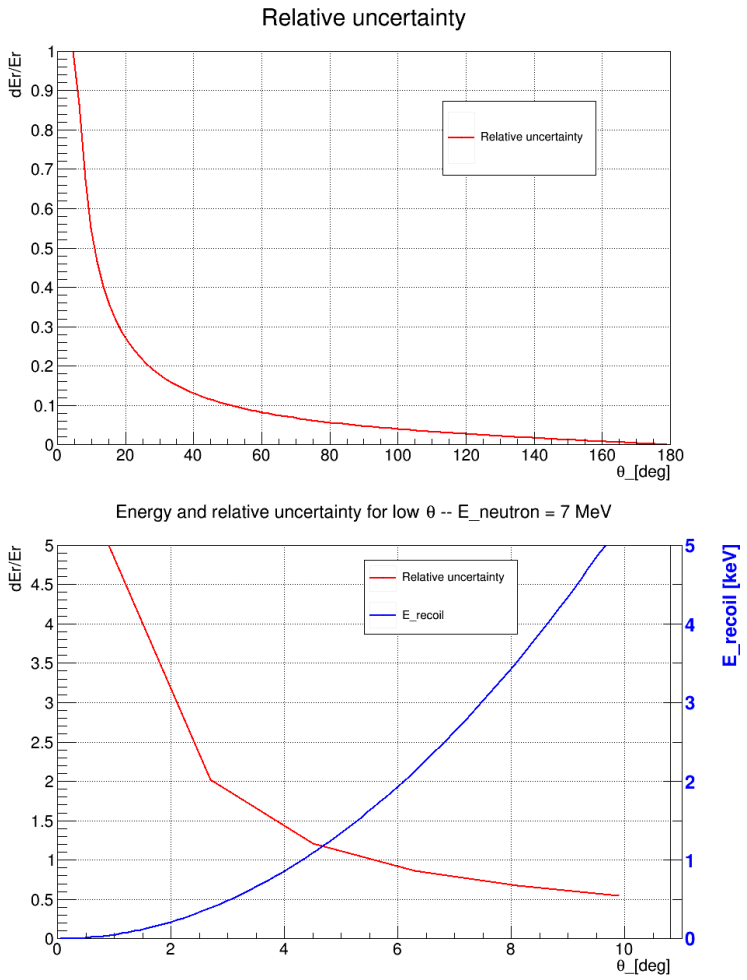

Fig. 3.11: Top Relative uncertainty induced on the recoil energy as a consequence of the uncertainty in the scattering angle θ. *Bottom* Relative recoil energy uncertainty and recoil energy for low neutron scattering angles and $E_n = 7\,\text{MeV}$ (compare this figure with Fig. A.3, where values are shown for $E_n = 2.5\,\text{MeV}$, neutrons mean energy of neutrons generated by the DD-neutron gun).

the scattering angle θ, as shown in Fig.3.11 on the top. It can be seen that the relative uncertainty becomes very large at small values of θ. Looking at eq. 3.7 this means that we are using a small percent of incoming neutron kinetic energy, or more specifically:

$$E_R \simeq E_n \frac{2A}{(A+1)^2} \cdot (1 - cos(36.8°)) \simeq 1\%\, E_n \tag{3.15}$$

Finally, as said in sec. 3.1 a low energy recoil measurement - at $E_R \sim 1\,\text{keV}$

- is in program. To reach this energy a very low scattering angle is required, which in LNS setup is $\theta_{LowEnergy} \simeq 4.3°$. In Fig. 3.11 on the bottom, the relative uncertainty and E_R vs low θ values are shown for $E_n = 7\,\mathrm{MeV}$.

3.6.2 Expected rates from calculations

In Fig. 3.2 we can see a simple sketch of the geometry of the experiment, from which it becomes clear that to estimate the neutron rate in a LiSCi (the "neutron detector") and neutron signal rate in a PMT as "triple" coincidence, we have to separate two interaction: first estimate the neutron rate in the TPC and then the neutron rate in LiSCi for neutrons coming from TPC.

So we study separately the rate (with correspondent solid angle) of reactions:

$$^{7}\mathrm{Li} + \mathrm{p} \rightarrow \mathrm{n} + ^{7}\mathrm{Be}, \tag{3.16}$$

and

$$n + ^{40}\mathrm{Ar} \rightarrow \mathrm{n} + ^{40}\mathrm{Ar} \qquad \text{(elastic)} \tag{3.17}$$

for the two interactions.

Rate of neutron arriving to the TPC

To calculate the rate of neutron arriving to the TPC we use:

$$\left.\frac{dN}{dt}\right|_{(n\,|\,\mathrm{TPC})} = \left.\frac{dN}{dt}\right|_{(^{7}\mathrm{Li}\,|\,\mathrm{CH_2})} \cdot \rho_{N(\mathrm{H}\,in\,\mathrm{CH_2})} \cdot d \cdot \left.\frac{d\sigma}{d\Omega}(E_{^{7}\mathrm{Li}}; \theta_n)\right|_{(n\,|\,\mathrm{TPC})} \cdot d\Omega(\mathrm{TPC}), \tag{3.18}$$

where:

- $\left.\frac{dN}{dt}\right|_{(n\,|\,\mathrm{TPC})}$ is the rate of neutrons emerging towards $d\Omega$(TPC), the TPC

solid angle with respect to the target,

- $\left.\frac{dN}{dt}\right|_{(^7\mathrm{Li}\,|\,\mathrm{CH_2})}$ is the rate of ^{7}Li impinging on solid CH_2 target, that we can write as:

$$\left.\frac{dN}{dt}\right|_{(^7\mathrm{Li}\,|\,\mathrm{CH_2})} = \frac{I_{beam}}{3e^-}, \tag{3.19}$$

  where I_{beam} is the beam current of ^{7}Li, 3 is Li atomic number (which corresponds the charge number of the accelerated ions) and e^- is the electron charge,

- $\rho_{N(\mathrm{H}\,in\,\mathrm{CH_2})}$ is the number density of H in the target,

- d is the target thickness,

- $\left.\frac{d\sigma}{d\Omega}(E_{^7\mathrm{Li}};\theta_n)\right|_{(n\,|\,\mathrm{TPC})}$ is the differential cross section for the reaction 3.16, with $E_{^7\mathrm{Li}}$energy of ^{7}Li impinging ions and θ_n the angle between the beam and the straight line joining target and TPC

- $d\Omega$(TPC) is the TPC solid angle with respect to the target, as said.

Moreover, targets are usually characterized by the *target surface density* ρ_{Surf} (Mass/Surface) so we can write:

$$\eta_N := \rho_{N(\mathrm{H}\,in\,\mathrm{CH_2})} \cdot d = \rho_{Surf} \cdot \frac{2 \cdot N_A}{\mathrm{M(CH_2)}}, \tag{3.20}$$

where η_N is the *superficial numerical density*, 2 comes from the number of H in CH_2 molecule, $\mathrm{N_A}$ is the Avogadro constant and $\mathrm{M(CH_2)}$ is the molar mass.

We can now introduce some values that will be the benchmarks for all calculations here presented (some definitions and values have been previously defined while some other will be introduced and used later):

- $E_{^7\mathrm{Li}}$= 28 MeV
- distance from CH_2 target to TPC: $D_{(\,CH_2\,|\,\mathrm{TPC})} = 150\,\mathrm{cm}$
- distance from TPC to LiSCi: $D_{(\mathrm{TPC}\,|\,\mathrm{LiSCi})} = 80\,\mathrm{cm}$
- angle at which is TPC wrt ^{7}Li beam direction: $\theta_n \simeq 22.3^\circ$
- scattering angle of neutron on ^{40}Ar: θ_3= $36.8^\circ(\simeq 37^\circ)$

  (that is the angle at which LiSCi are wrt target-to-TPC direction, see Fig.3.2)
- ^{7}Li electric beam current: $I_{beam} = 1\,\mathrm{nA}$
- target surface density: $\rho_{Surf} = 244\mu g/cm^2$
- $\frac{d\sigma}{d\Omega}(E_{^7\mathrm{Li}} = 28\,\mathrm{MeV}; \theta_n = 22.3^\circ)\Big|_{(n\,|\,\mathrm{TPC})} \simeq 100$ mb/sr
- $\frac{d\sigma}{d\Omega}(E_n = 7\,\mathrm{MeV}; \theta_3 = 36.8^\circ)\Big|_{(n\,|\,\mathrm{LiSCi})} \simeq 0.7$ b/sr

To evaluate $\frac{d\sigma}{d\Omega}(E_{^7\mathrm{Li}} = 28\,\mathrm{MeV}; \theta_n = 22.3^\circ)\Big|_{(n\,|\,\mathrm{TPC})}$ we extract data from Figs. 3.12. In particular we assume that aware of edges in the neutrons cone, the differential cross section is almost flat, as indicated in Fig. 3.12 on the right. Note that the $E_{^7\mathrm{Li}}$ is different (15 MeV vs 28 MeV), but we are confident that the behaviour could be approximately the same. So we can use the value for $\theta_n = 0^\circ$ as reported by Drosg [115], in the figure on the left, and get:

$$\frac{d\sigma}{d\Omega}(28\,\mathrm{MeV}, 22.3^\circ)\Big|_{(n\,|\,\mathrm{TPC})} \simeq \frac{d\sigma}{d\Omega}(28\,\mathrm{MeV}, 0^\circ)\Big|_{(n\,|\,\mathrm{TPC})} \simeq 100\,\mathrm{mb/sr}, \quad (3.21)$$

as written.

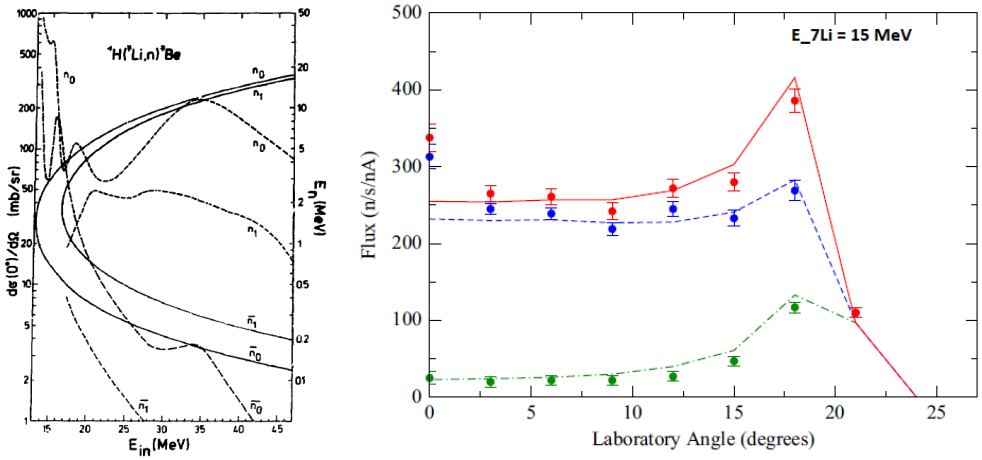

Fig. 3.12: *Left* Cross section (dashed curve) at 0° and neutron energies (solid curves) in the laboratory system for the reaction $^1H(^7\mathrm{Li},\mathrm{n})^7\mathrm{Be}$ vs incoming energy (From [115]). *Right* Angular distribution of the principal peak (blue dashed line) and the satellite peak (green dashed-dotted line) vs laboratory angle for the neutron emission (red continuous line is the sum of the two) for $E_{^7\mathrm{Li}} = 15\,\mathrm{MeV}$ (From [105]).

From the above reported values and definitions, we have:

$$\left.\frac{dN}{dt}\right|_{(^7\mathrm{Li}\,|\,\mathrm{CH_2})} = \frac{1\mathrm{nA}}{3\cdot e^-} \simeq 2.08\times10^9\,\mathrm{s}^{-1}\Big|_{(I_{Beam}=1\,\mathrm{nA})}, \tag{3.22}$$

$$\eta_N \simeq 2.1\times10^{19}\,\mathrm{cm}^{-2}\Big|_{(\rho_{Surf}=244\mu g/cm^2)}, \tag{3.23}$$

and[5]

$$d\Omega(\mathrm{TPC}) \simeq \frac{5\mathrm{x}5\,\mathrm{cm}^2}{(150\,\mathrm{cm})^2} = \frac{1}{900}\,\mathrm{sr}. \tag{3.24}$$

Putting previous results in eq. 3.18, finally for the neutron rate in TPC we obtain:

$$\begin{aligned}\left.\frac{dN}{dt}\right|_{(n\,|\,\mathrm{TPC})} &\simeq 2.08\times10^9\,\mathrm{s}^{-1}\cdot 2.1\times10^{19}\,\mathrm{cm}^{-2}\cdot 100\,\mathrm{mb/sr}\cdot\frac{1}{900}\,\mathrm{sr}\\ &\simeq 4.9\,\mathrm{Hz}\Big|_{(1\,\mathrm{nA};244\mu g/cm^2;100\,\mathrm{mb/sr})}\end{aligned} \tag{3.25}$$

[5] The active LAr in the TPC has a lateral surface of $5\mathrm{x}5\,\mathrm{cm}^2$.

Rate of neutrons arriving to one LiSCi

In the same way, to calculate the rate of neutrons arriving to one LiSCi we use:

$$\left.\frac{dN}{dt}\right|_{(n\,|\,\mathrm{LiSCi})} = \left.\frac{dN}{dt}\right|_{(n\,|\,\mathrm{TPC})} \cdot \rho_{N\,(^{40}\,\mathrm{Ar}\,in\,\mathrm{LAr})} \cdot d_{LAr} \cdot \left.\frac{d\sigma}{d\Omega}(E_n;\theta_3)\right|_{(n\,|\,\mathrm{LiSCi})} \cdot d\Omega(\mathrm{LiSCi}), \tag{3.26}$$

where:

- $\left.\frac{dN}{dt}\right|_{(n\,|\,\mathrm{LiSCi})}$ is the rate of neutrons emerging from TPC towards $d\Omega$(LiSCi), the LiSCi solid angle with respect to the TPC
- $\left.\frac{dN}{dt}\right|_{(n\,|\,\mathrm{TPC})}$ is the rate of neutrons impinging on TPC (as previously evaluated, eq 3.25)
- $\rho_{N\,(^{40}\,\mathrm{Ar}\,in\,\mathrm{LAr})}$ is the number density of LAr
- d_{LAr} is the distance that a neutron must cross in active LAr, that for this purpose we can consider $d_{LAr} \simeq 5\,\mathrm{cm}$
- E_n is the energy of neutron emerging from the TPC, that for this purpose we can consider $E_n \simeq 7\,\mathrm{MeV}\Big|_{(E_{Beam}=28\,\mathrm{MeV})}$, and θ_3 angle between beam of neutrons impinging the TPC an the straight line joining TPC and LiSCi
- $\left.\frac{d\sigma}{d\Omega}(E_n;\theta_3)\right|_{(n\,|\,\mathrm{LiSCi})}$ is the differential cross section for the elastic scattering $n + {}^{40}\mathrm{Ar} \rightarrow \mathrm{n} + {}^{40}\mathrm{Ar}$
- $d\Omega$(LiSCi) is the LiSCi solid angle with respect to the TPC, as said.

To evaluate $\left.\frac{d\sigma}{d\Omega}(E_n;\theta_3)\right|_{(n\,|\,\mathrm{LiSCi})}$ we need the neutron energy E_n emerging from the $p({}^7\mathrm{Li}, n){}^7\mathrm{Be}$ reaction. As you can see in Fig. 3.10 on top, where neutron energy vs ^{7}Li beam energy is reported, for $I_{Beam} = 28\,\mathrm{MeV}$ we have $E_n \sim 7\,\mathrm{MeV}$[6].

[6] The geometrical value of E_n, i.e. using θ_n value, is $E_n = 7387\,\mathrm{keV}$. However if you take into account the neutrons energy distribution on TPC this value is only an indication.

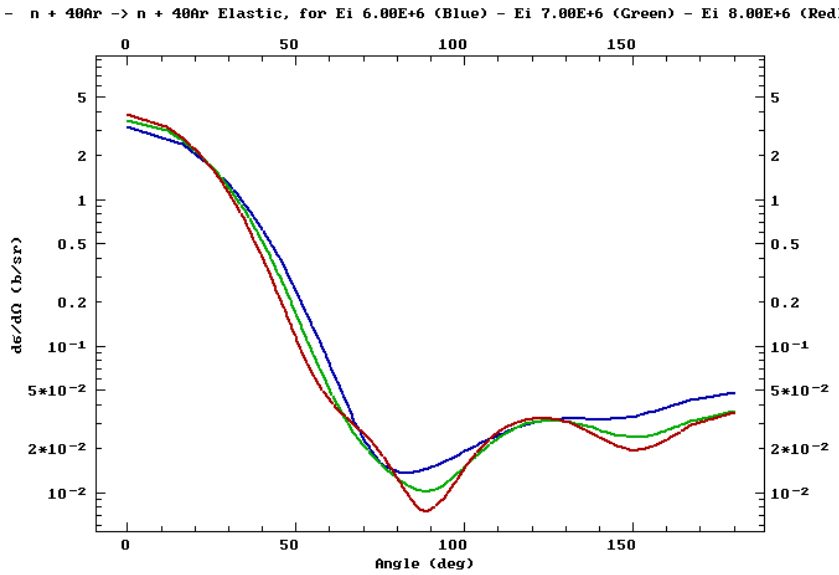

Fig. 3.13: Differential cross section for the impinging neutron of energy 6-7-8 MeV. As we can see the cross section for $\theta_3 \simeq 37°$ can be considered about constant. Plot from [116]

Using data from Evaluated Nuclear Data File (ENDF) [116], we find for elastic scattering $\frac{d\sigma}{d\Omega}(E_n = 7\,\text{MeV}; \theta_3 = 36.8°)\Big|_{(n\,|\,\text{LiSCi})} \simeq 0.7$ b/sr. In Fig. 3.13 on the right a plot of the differential cross section for impinging neutron energy of 6-7-8 MeV is shown. As we can see the cross section for $\theta_3 \simeq 37°$ can be considered about constant for this energies.

After straightforward calculations, putting results in eq. 3.26, finally for the neutron rate impinging one LiSCi we get:

$$\begin{aligned}\frac{dN}{dt}\Big|_{(n\,|\,\text{LiSCi})} &\simeq 4.9\,\text{Hz} \cdot 2.11 \times 10^{22}\,\text{cm}^{-3} \cdot 5\,\text{cm} \cdot 0.7\,\text{b}\,\text{sr}^{-1} \cdot 7.13 \times 10^{-3}\,\text{sr} \\ &\simeq 2.58 \times 10^{-3}\,\text{Hz}\Big|_{(1\,\text{nA};244\mu g/cm^2;100\,\text{mb/sr})}\end{aligned} \tag{3.27}$$

"Triple" events rate

If we consider the detection efficiency of the liquid scintillator EJ-309, which for $E_n \sim 7\,\text{MeV}$ is about 30% [117], the rate of interactions in one LiSCi, the so-called

"triple" events, is:

$$\frac{dEvents}{dt}\Big|_{(\mathrm{PMT})} \simeq 7.74 \times 10^{-4}\,\mathrm{Hz}\Big|_{(1\mathrm{PMT};1\,\mathrm{nA};244\mu g/cm^2;100\,\mathrm{mb/sr})} \tag{3.28}$$

or

$$\frac{dEvents}{dt}\Big|_{(\mathrm{PMT})} \simeq 2.7\,\mathrm{cph}\Big|_{(1\mathrm{PMT};1\,\mathrm{nA};244\mu g/cm^2;100\,\mathrm{mb/sr})} \tag{3.29}$$

or

$$\frac{dEvents}{dt}\Big|_{(\mathrm{PMT})} \simeq 67.0\,\mathrm{cpd}\Big|_{(1\mathrm{PMT};1\,\mathrm{nA};244\mu g/cm^2;100\,\mathrm{mb/sr})} \tag{3.30}$$

Those values are really consistent with Monte Carlo simulations but not with data taken until now. From analysis of data taken in July 2018 it can be said that (sec. 4.2):

$$\frac{\Delta Events}{\Delta t}\Big|_{(\mathrm{PMT})} \leq 0.26\,\mathrm{cph}\Big|_{(1\mathrm{PMT};1\,\mathrm{nA};244\mu g/cm^2)} \tag{3.31}$$

about a factor of ten less with respect to calculations and MC simulations.

It is important to recall that a -strong- assumption in this calculations is the "flatness" of the differential cross section for the reaction 3.16 (see eq. 3.21).

It is worth noticing that this assumption is shared with Monte Carlo simulations.

POST SCRIPTUM after the last week of September 2018 beam time

Preliminarily results from data taken during the last days of the last week of September 2018, i.e. at the time of writing, confirm the assumption on the values on $p(^7\mathrm{Li}, n)^7\mathrm{Be}$ cross section (eq. 3.21), used for the above reported calculations.

4. RED @ “LNS": COMMISSIONING AND PRELIMINARY RESULTS

In this chapter we report some preliminary results from data acquired during ReD commissioning at LNS. First one week test beam was done in June-July, 2018, and one more week beam time is scheduled at the end of September 2018.

Before the tests at LNS in Catania, a partial commissioning of the actual optimized cryogenic-and-TPC setup was done at Naples ”Federico II” University. Indeed the first integration of the cryosystem, LAr TPC and SiPMs occurred only on May 21, 2018. Anyway a lot of work was done in Naples University to commissioning ReD[1], and preliminary data were taken also with neutrons emitted from a DD-neutron gun ($E_n \simeq 2.5\,\mathrm{MeV}$). Neutron rate from DD-gun is too low to do the directional experiment in a closed kinematics approach (but other approaches could be thought), while it can be useful to study for example low energy nuclear recoil (more on the DD-neutron gun and its experimental potentialities in app. A). Even if partial, the commissioning of the system at Naples allowed for a first characterization of the LAr TPC, operated in single and double phase, with new SiPMs and for an integrated test of: operating procedures, DAQ, a new LabVIEW-based slow control, data handling and reconstruction algorithms. These preliminary test showed a promising light yield of about 11 phe/keVee at null field (from ^{241}Am $60\,\mathrm{keV}\,\gamma$s). The partial commissioning and characterization of the system in Naples opened the way for the deployment of the system at

[1] Also with another setup, before the optimized setup described in this work was adopted; e.g. a different TPC with different SiPMs (SensL's -C/J Series or FBK 1x1 cm^2) was commissioned and operated in single and double phase during last two years.

the beamline of LNS: the "Naples setup" was shipped to LNS on June 13, 2018. It was installed and integrated with the n-Spectrometer and the scattering chamber and globally aligned from June 18 to June 21, so that first beam-time was able to start on June 22, 2018.

Data taking campaigns at LNS, which include calibrations on the three detectors (Si-$\Delta E/E$, TPC, LiSCis-PMTs), were done in June and July[2]. In June, beam availability was on 22 to 24, wile in July on 5 to 11, 2018.

It is worth noting that June and July beam time at the beginning are dedicated to "technical runs", particularly to allow calibrations, to check on correct system alignment and to "characterize" the beam.

Next sections contain some data analysis on calibration data of the three detectors and a preliminary data analysis of data collected with the neutron beam in Si-PMT configuration trigger, during the last days of the beam time in July, 2018.

Some issues emerged during test beams are also reported, particularly to direct attention on issues that could have implications for DarkSide-20k, e.g. a strong ITO and/or TPB deterioration on acrylic after only one cooling cycles.

4.1 Calibrations

Every detector has been singularly calibrated prior to the integrated use in the system. In this section some results of the three detectors calibration are reported.

Radionuclide	α Energy [MeV] - principal lines	Intensity [%]
^{239}Pu	5.105	11.5
	5.143	15.1
	5.155	73.4
^{241}Am	5.388	1.4
	5.443	12.8
	5.486	85.2
^{244}Cm	5.763	23.3
	5.805	76.7

Tab. 4.1: α-emitters used for the Si telescope calibration. Only principal lines are reported.

4.1.1 Si-$\Delta E/E$ calibration

Silicon $\Delta E/E$-telescope calibration is useful for identification and energy determination of impinging particles. However the main role is to trigger the DAQ so that it can be possible to use ToF technique, which obviously becomes more successful with particle identification.

To calibrate the $\Delta E/E$ -telescope we use a composite α-source made by singles ^{239}Pu, ^{241}Am and ^{244}Cm α-sources with α-energies from about 5.1 MeV up to about 5.8 MeV. In Tab. 4.1 α-energies principal lines are reported, while in Fig.4.1 on the left the composite α-source spectrum is shown.

Even if α-energies are not in the energy range of impinging particles, which at $E_{Beam} = 28$ MeV start at about 18 MeV for lowest energy ^{7}Be *locus* up to E_{Beam}, which corresponds to ^{7}Li elastic scattering on C in the target, linearity in the composite range can be supposed. It is worth noting that this α-calibration is also useful just to simply check the detector.

ΔE - E Si detectors scatter plot is displayed in Fig. 4.1 on the right: it shows the ability of the telescope to discriminate the charged products of the beam-

[2] As mentioned, another data taking campaign is now ongoing at LNS (last week of September 2018). Time constraints prevent to add this new data in this work.

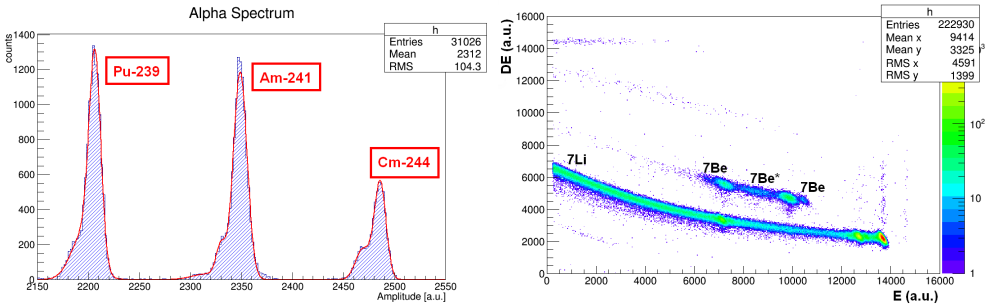

Fig. 4.1: Left E detector composite α-source spectrum. From the left ^{239}Pu, ^{241}Am and ^{244}Cm α-sources are flagged. *Right* Scatter plot of the amplitudes of the ΔE and E Si detectors, placed at 5 deg with respect to the beam axis.

target reactions, i.e. the main ^{7}Li band due to elastic scattering, the two ^{7}Be *loci* corresponding to the two solutions allowed by kinematics as also ^{7}Be* (see sec. 3.2, particularly Fig. 3.4 on the right).

4.1.2 LiSCi PMTs calibration

Tests and calibrations on LiSCi-PMTs were done at LNS to commission the n-spectrometer, e.g. energy calibration with 511 keV γ from ^{22}Na source and, more important for the experiment, test on timing performance and PSD capability[3].

In Fig. 4.2 we can see LiSCi PSD vs keVee, from data collected with a ^{252}Cf source located near the LiSCi0 and illuminating all the LiSCi cells, where LiSCi PSD is defined here as:

$$\mathrm{PSD}_{\mathrm{LiSCi}} = 1 - \frac{t_{short}}{t_{long}} \tag{4.1}$$

with $t_{short} = 60$ ns and $t_{long} = 700$ ns, long enough to contain the whole waveform.

Furthermore, defined Figure of Merit (FOM) as:

$$\mathrm{FOM} = \frac{\mu_n + \mu_\gamma}{\sqrt{\sigma_n^2 + \sigma_\gamma^2}} \tag{4.2}$$

[3] More accurate energy calibration had preliminary done on LiSCi-PMTs, see [118]

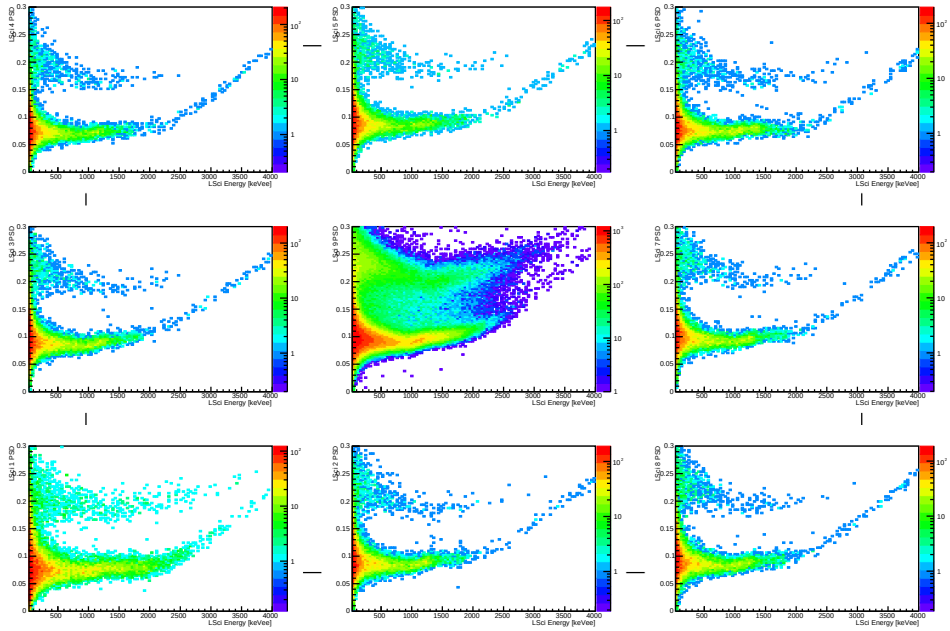

Fig. 4.2: LiSCi PSD vs keVee, from data collected with a ^{252}Cf source located near the LiSCi0 and illuminating all LiSCis cells.

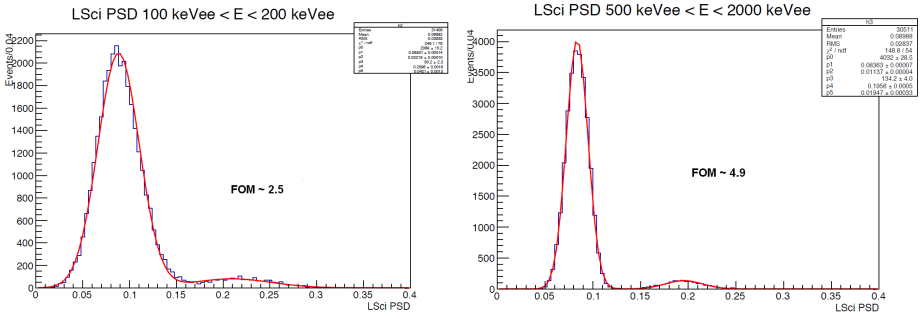

Fig. 4.3: FOM for two different LiSCi keVee energy ranges.

in Fig. 4.3 we can see as FOM varies with respect to deposited energy, for two different LiSCi keVee energy ranges.

Using a β^+ ^{22}Na source, thanks on the two 511 keV γs emerging back to back from para-positronium decay, it is also possible to make a test on LiSCi-PMTs timing performance. In Fig. 4.4 on the left we can see the difference in time of signals formation from 511 keV γ in two neighboring ($\sim$ 30 cm) LiSCi, triggered in coincidence. The absolute values is about 3 ns, allowing for the ToF technique.

With the same ^{22}Na source data it is also possible study LiSCi-PMTs trigger

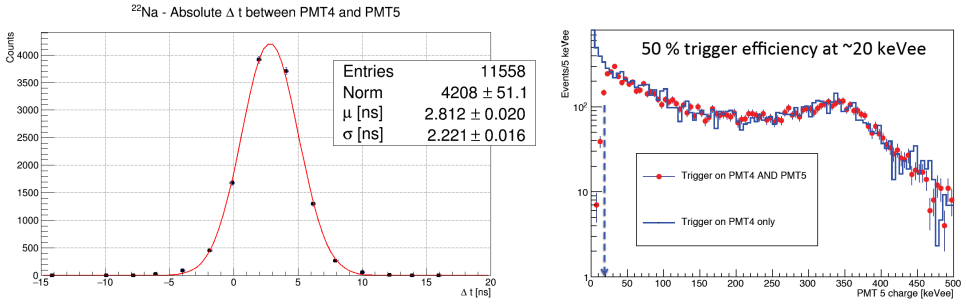

Fig. 4.4: Left Difference in time of signals formation from β^+/β^- back to back 511 keV γ in two neighboring ($\sim$ 30 cm) LiSCi, triggered in coincidence. *Right* LiSCi-PMTs trigger efficiency, which is about 50% at $\sim$ 20 keVee to 100% at $\sim$ 40 keVee.

efficiency, which is about 50% at $\sim$ 20 keVee to 100% at $\sim$ 40 keVee, as can be seen in Fig. 4.4 on the right.

4.1.3 TPC monitoring and calibration

To ensure LAr-TPC work condition stability, thermodynamics parameters where continuously monitored via the LabVIEW monitoring system: in particular cryostat absolute pressure (maintained at (1.11 ± 0.01) bar), liquid argon level and temperature. Temperature and level of LAr were kept constant through a heater block attached to the PT-90 cryocooler cold-head. Along with the resistance temperature detector (RTD) on the cold-head and a Lake Shore Model 336 cryogenic temperature controller, they formed a closed-loop temperature control operating in proportional-integral-derivative (PID) mode. Two additional PT1000 RTDs, at a distance of about 1.5 cm each other, were installed in the dewar at about 18 cm above the top of the TPC, to monitor temperature and verify liquid level data, which has been maintained between the two RTDs. In this way we can have access to absolute pressure value in the gas pocket.

The TPC was operated principally in two configurations, one at zero fields and no gas pocket while the other, from now the "standard" configuration, with gas pocket and nominal fields at $E_{drift} = 200V/cm$, $E_{extr}, = 2.8kV/cm$ and

Configuration	**Anode** (V)	**First ring** (V)	**Cathode** (V)
Standard	+3780	+85	-815
Run 544	+3780	+340	-3260
Run 554	+5670	+85	-815
—	$\mathbf{E_{drift}}$ (V/cm)	$\mathbf{E_{extr}}$ (kV/cm)	$\mathbf{E_{elect}}$ (kV/cm)
Standard	200	(2.8)	(4.2)
Run 544	(800)	(2.8)	(4.2)
Run 554	(200)	(4.2)	(6.3)

Tab. 4.2: Principal used potentials/fields configurations. More in text.

$E_{elect} = 4.2kV/cm$. These values were chosen to be the same of DarkSide-50. In Table 4.2 the main potentials applied to TPC and nominal electric fields so obtained are reported. The grid has always been kept at ground, so its value is not reported. In standard configuration cathode and first ring potentials were selected, by COMSOL simulation software [119], to obtain homogeneous $E_{drift} = 200V/cm$ in the active volume. Electric field values in brackets refer to values not yet simulated. These values are simply deducted for E_{drift} by using cathode potentials ratio as multiplication factor, or for E_{extr} and E_{elect} by using equation 2.21. For this reason electric fields are reported as "nominal" in text.

Finally, during data taking, SiPMs V_{bias} was at 34 V, about 7 V of over voltage with respect to $V_{breakdown}$.

Single photoelectron calibration

As said, while on the top there is a 24-single-channel readout via a 24-channel FEB, on the bottom the 24 SiMPs are summed six to six to form 4 channels, in a 2-Series 3-Parallel way. The single photoelectron response (SER) of each of 24 channels on the top plus the 4 channels on the bottom was monitored

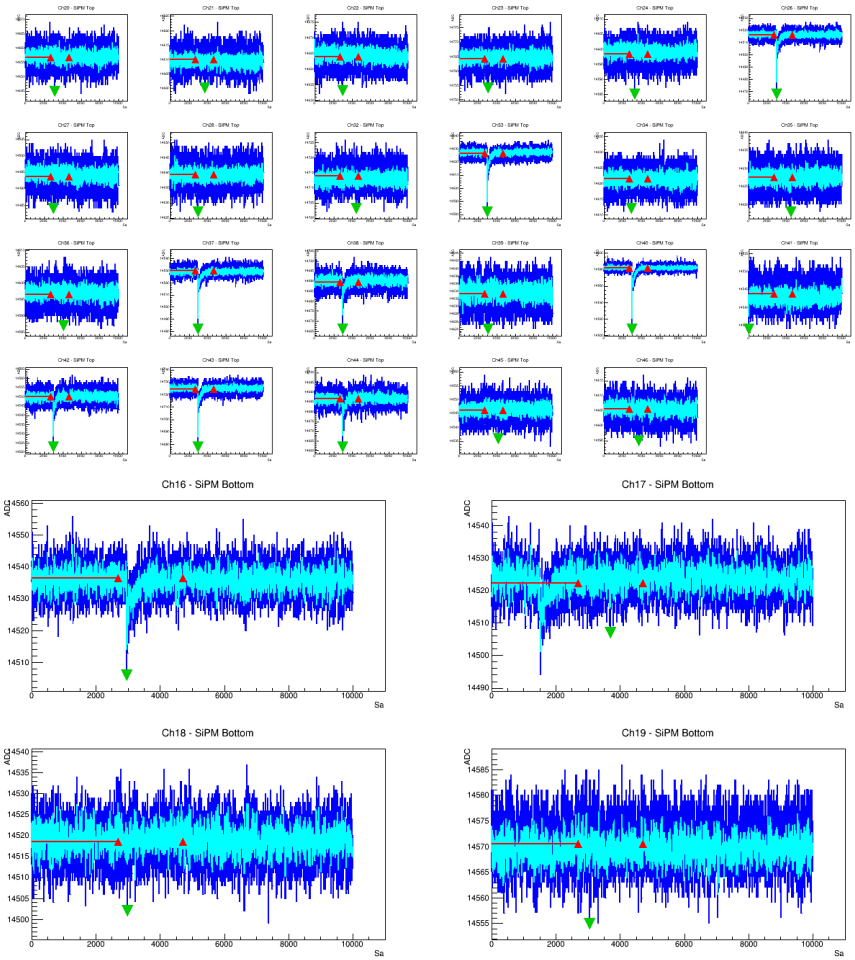

Fig. 4.5: Some single photoelectron waveforms from the same laser controller triggered event. Markers are explained in the text. *Top* Single photoelectron waveforms in some of 23 of 24 channels of the top FEB. *Bottom* In the 4 channels of the bottom FEB only one single photoelectron waveform in time with the trigger signal is visible.

by injecting, in the cryostat, light pulses of 403 nm wavelength, 50 ps pulse duration, from a PLP-10 laser diode by Hamamatsu [120], attenuated to meet the correct (low) channels occupancy. To record the corresponding waveforms, simultaneously with light pulses, a trigger signal was sent from the laser controller to the data acquisition system. We took about one calibration "laser run" every five "physical runs", each of at least 100 k events.

In Fig. 4.5 it is shown an example of SiPMs single photoelectron waveforms from the same laser controller triggered event. On top single photoelectron waveforms of some of 23 of 24 channels of the top FEB may be identified (the 24th

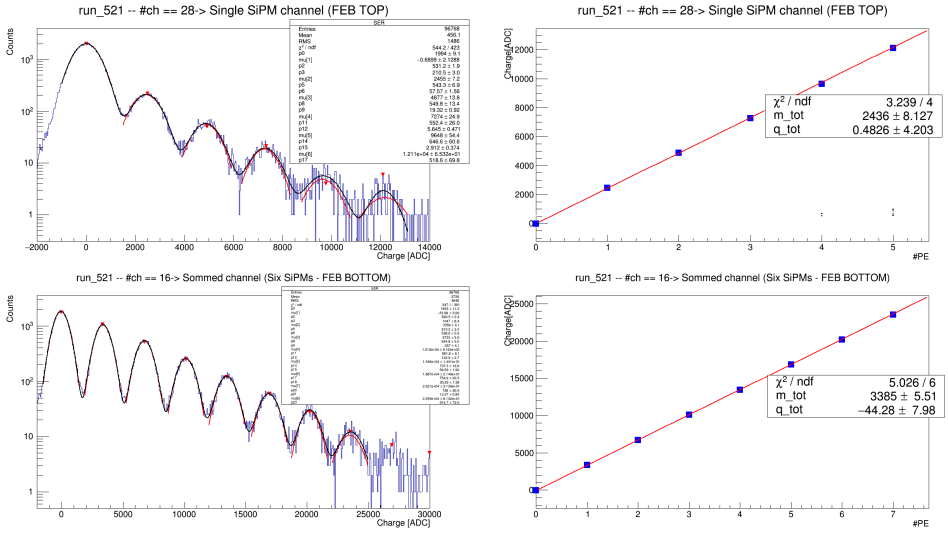

Fig. 4.6: Left SERs of one top channel and of one bottom channel readouts. *Right* We consider the angular coefficient of the straight line as the correct SER value. More in the text.

channel did not work during last data taken on July week. It seems that some soldering of an at cold operating operational amplifier did breaks.). On bottom the 4 waveforms of the 4 channels of the bottom FEB: only one single photoelectron waveform is visible in time with the trigger signal. In the plots the raw waveforms are blue, while the light blue are the reconstructed waveforms after that a Sensitive Nonlinear Iterative Peak (SNIP) filtering is applied. Finally, the red straight segment shows the range on which the baseline is calculated, red triangular markers show the extremes of the range on which the charge integral is calculated, while the green triangular marker tags the absolute waveform maximum value in the charge integral range (result of the peak finder analysis module).

A fit on superimposed single photon electron waveforms returns $\tau_{recov} \sim 0.5\,\mu$s as recovery time of SiPM single cell, consistent with the quenching resistance of $10\,\mathrm{M}\Omega$ and the cell capacitance of the order of a few tens of femto-Farad. A τ_{recov} of the order of only about one quarter of LAr τ_T scintillation, has to be taken into account in the t_{prompt} estimation to maximizes the separation among ERs

and NRs distributions (see sec. 2.2.2). More in sec. 4.1.3.

In Fig. 4.6 on the left SERs spectra of one top channel and of one bottom channel readouts are displayed. Comparison of the two left plots shows the difference in occupancy, mainly due to the different exposed area. The global fit function superimposed (in black) is obtained by the sum of an appropriate number of Gaussian functions (in red) describing the single photo-electron (first peak after the pedestal) and multiple photo-electron distributions. On the right the corresponding fit, in which the points are the mean values of the overlapping distributions, obtained from the global fit. We consider the angular coefficient of the straight line as the correct SER value.

S1 light yield calibration

To evaluate and monitor the LAr TPC S1 scintillation LY, which depends both on LAr absolute light yield and on TPC constructive characteristic, we used an ^{241}Am source, which has a dominant γ-line of 59.5 keV able to cross the dewar walls and reach the active LAr, placed on the outside surface of the dewar.

We get that the sum of top and bottom readout LY, in July was about 10 PE/keV at zero drift field [$\mathrm{LY_{top}} = (5.1 \pm 0.7)\,\mathrm{PE/keV}$ and $\mathrm{LY_{bottom}} = (4.9 \pm 0.6)\,\mathrm{PE/keV}$], while a nominal drift field of 200 V/cm introduce a global quenching factor of about 10% [$\mathrm{LY_{top}} = (4.3 \pm 0.6)\,\mathrm{PE/keV}$ and $\mathrm{LY_{bottom}} = (4.6 \pm 0.6)\,\mathrm{PE/keV}$ at $E_{drift} = 200\,\mathrm{V/cm}$ nominal]. Fig. 4.7 on top shows LY distributions separately obtained from top and bottom readout at zero drift field; on bottom same distributions at 200 V/cm nominal drift field are shown. Thin difference between mean values in top and bottom readout can be due to optical factors, e.g. non perfectly equidistant source position.

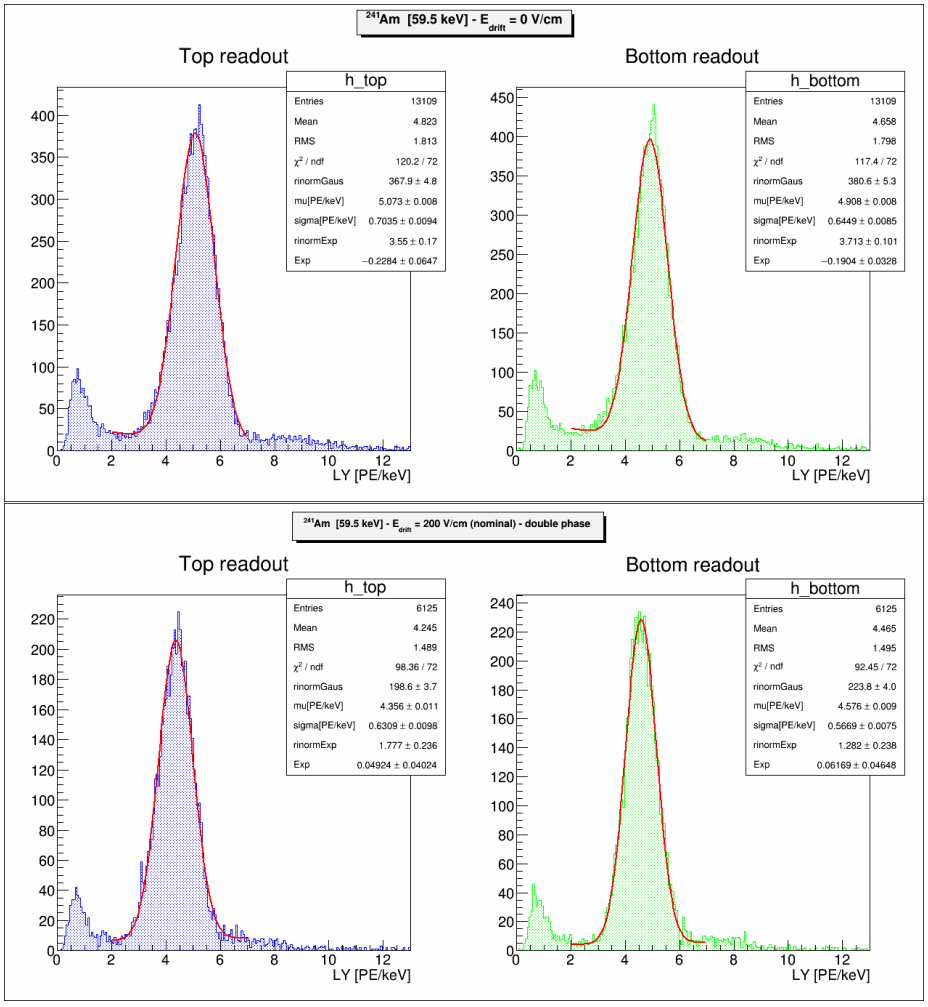

Fig. 4.7: S1 light yield calibration from ^{241}Am source. More in the text.

During commissioning tests made in Naples, for LY (even from ^{241}Am) at zero drift field we obtained about 11 PE/keV. We related this loss of LY to the degradation of the TPB deposition on acrylic substrate, on top an bottom windows and lateral walls. It seams that this effect became worse and worse at every temperature cooling-heating cycle.

In Fig. 4.8 two photos taken during a visual inspection at LNS clean room show a strong TPB degradation on top window, even with little TPB flakes on the grid. It is not clear if even the ITO on top and bottom windows, which unlike the TPB is transparent, has suffered a similar degradation.

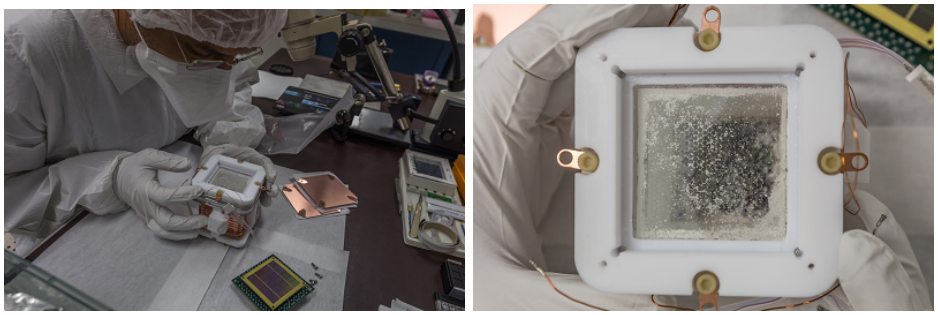

Fig. 4.8: Degradation of the TPB deposition on acrylic substrate. It can be seen the strong TPB degradation on top window, even with little TPB flakes on the grid.

f_{prompt} optimization via ^{252}Cf neutron source

As said, a fit on superimposed single photon electron waveforms shows $\tau_{recov} \sim 0.5\,\mu$s as recovery time of SiPMs single cell. This recovery time, comparable to LAr triplet lifetime ($\tau_T \simeq 1.6\,\mu$s), decrees the giving up of f_{90}, with a change on t_{prompt} which can only be an increase (see sec. 2.2.2). A simple analytical model in which the single photo-electron is modeled with an exponential, convoluted with the LAr response function, shows that if $\tau_{recov} = 0.5\,\mu$s then $t_{prompt} \sim 850\,$ns should be used to optimize ERs and NRs separation, that results in about 0.4-0.6 mean value bands for ERs and NRs respectively.

The t_{prompt} optimization is still under study; nevertheless using an empirical approach on data collected with a ^{252}Cf neutron source, we get that $t_{prompt} \sim 700\,$ns, with a corresponding separation of about 0.25-0.55 bands, is up to now the best choice for actual TPC configuration.

Fig. 4.9 shows ($S1$[keVee]; $f_{700\,\mathrm{ns}}$) scatter plots and $f_{700\,\mathrm{ns}}$ distributions from ^{252}Cf neutron source data, on top at zero electric fields and without gas pocket, while on bottom with electric field at "standard" values as reported in the introduction of this section 4.1.3 (so $E_{drift} = 200V/cm$), and gas pocket on. The $f_{700\,\mathrm{ns}}$ distributions are for E $\in [11, 26]$ keVee range; FOM as defined in eq. 4.2 are also

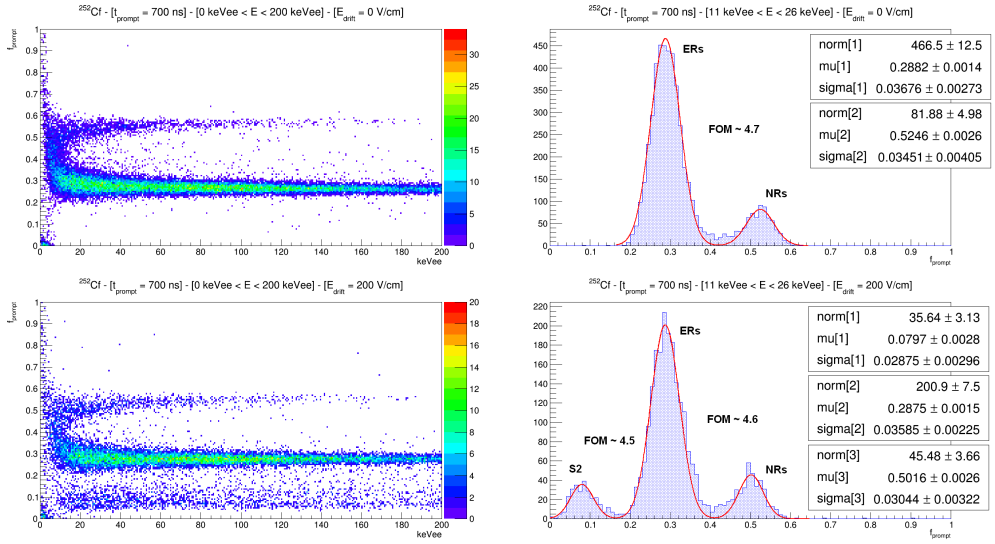

Fig. 4.9: (S1;f_{700}) scatter plots and f_{700} distributions for single phase and double phase ^{252}Cf runs. More in text.

reported. This energy range has been chosen considering neutron induced ^{40}Ar nuclear recoil energy at energy and geometrical conditions we operated in July at LNS, as well considering the nuclear recoil quenching factor (see sec. 2.2.3). As can be seen, both at zero field and $E_{drift} = 200V/cm$ NR and ER distributions are well distinguishable. Furthermore in double-phase setup, S2 events distribution is also well distinguishable in $f_{prompt} < 0.2$ region.

Electrons lifetime

To check for e^- lifetime when the TPC is running we plan to use a ^{83m}Kr source, as DarkSide-50 does. ^{83m}Kr has a half life of 1.82 hours and decays in two sequential conversion electrons with energies of 9.4 and 32.1 keV and a mean separation of 222 ns [121]. Because scintillation signals in LAr last for several microseconds (sec. 2.2.1) and electrons mean tracks in LAr are negligible at these energies, the two decays can be treated as a single event of 41.5 keV for both S1 and S2. As Kr is a noble gas, ^{83m}Kr isotope stays spread all over the Ar volume. However, during LNS operations we didn't use ^{83m}Kr source but, as

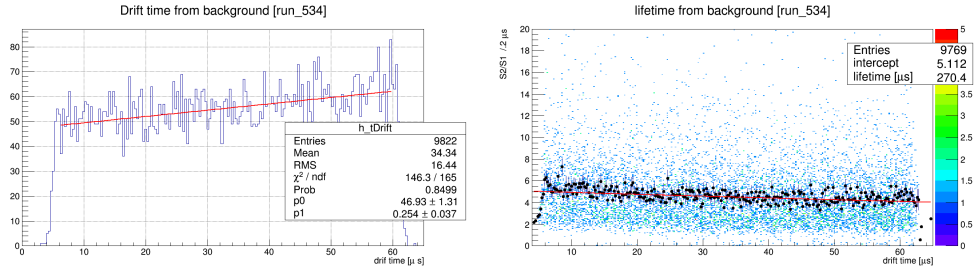

Fig. 4.10: Distributions from background data (run 534). *Left* Drift time distribution. See text for more details. *Right* S2/S1 and S2/S1 mean ratio drift time distributions. The lifetime after one week of argon recirculation results about $\tau_l \simeq 270\,\mu$s.

backup solution, we used background events, which in general we expect to be evenly spread throughout the detector, leading to a flat drift time distribution. Figure 4.10 on the left shows the drift time distribution of background events from run 534 ("standard" fields), operated after one week of argon recirculation, which instead is peaked towards longer drift times. One possible explanation for this bias is that, because the trigger is formed solely by the 4 bottom channels, we trigger more favorably on events closer to the bottom of the detector. This seems unlikely because the applied software threshold (5 keV $\sim$ 50 PE) is significantly higher than the trigger threshold, and even at upper software thresholds the behavior does not change. An alternative explanation is that, as the bottom of the TPC is at only about one cm from bottom of the dewar, while the top of the TPC has some tens of cm of LAr above, this bias could come out from LAr auto shielding capability. Anyway to evaluate e^- lifetime we use S2/S1 mean ratio versus drift time distribution, which should allow to avoid systematics. Although there is a large spread in S2/S1 ratio over a population of events, the mean value of S2/S1 measured as a function of drift time should follow the same trend as a S2 distribution from events of a diffused source[4]. Figure 4.10 on the right

[4] Although a S1 intensity top-bottom asymmetry is always present in double phase TPCs, due on partial light reflection at liquid-vapor interface, the systematic is on the order of some percents. So at first order this correction can be omitted.

shows S2/S1 and S2/S1 mean ratio drift time distributions, still from run 534. By an exponential fit on S2/S1 mean ratio, the lifetime, as defined in section 2.2.8, results in about $\tau_l \simeq 270\,\mu$s. It can be seen also that the maximum drift time at standard fields (e.g. $E_{drift} = 200\,\mathrm{V/cm}$ nominal), is about $62\,\mu$s, so that the lifetime is more than four times the maximum drift time, or better that $N_e(\,\mathrm{t_{drift}}_{Max}) \simeq 0.8 N_e(0)$, good enough for commissioning runs.

With above values we get $v_{drift} \sim 0.8\,\mathrm{mm}/\mu$s. It must be stressed that this value is not in agreement with that found in literature [122], and also as measured at same E_{drift} in DarkSide-50, which is $v_{drift}\Big|_{(DS-50)} \simeq (0.93 \pm 0.01)\,\mathrm{mm}/\mu$s ([64]). This discrepancy is still under investigation.

S2 light yield calibration

In TPC technology S2 light yield calibration is performed at the same time as S1 light yield calibration. As said in sec. 2.2.4, even (anti)-correlation between S1 and S2 is expected. Moreover "central limit theorem" can be usually applied here, so that S1 and S2 distributions may be described with Gaussian PDFs, while S1 and S2 joint distribution $P(S1;S2)$ may be modelled as a bivariate Gaussian:

$$P(S1;S2) = \frac{C}{2\pi\sigma_{S1}\sigma_{S2}\sqrt{1-\rho^2}} \exp\left[\frac{r}{1-\rho^2}\right]$$

$$\text{where} \tag{4.3}$$

$$r = \frac{(S1-\mu_{S1})^2}{\sigma_{S1}^2} + \frac{(S2-\mu_{S2})^2}{\sigma_{S2}^2} - \frac{2\rho(S1-\mu_{S1})(S2-\mu_{S2})}{\sigma_{S1}\sigma_{S2}}$$

and μ_{S1}, σ_{S1}, μ_{S2}, σ_{S2} are respectively the mean and sigma of S1 and S2 Gaussian distributions, while ρ is the correlation factor between S1 and S2. This is a standard approach in calibration data analysis to achieve higher energy resolution, although Gaussian fitting on S1 and S2 separately is still a correct approach.

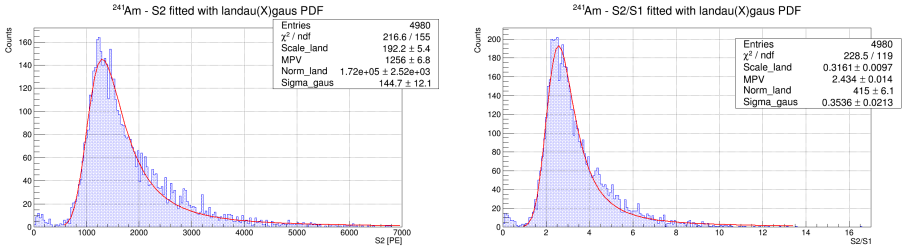

(a) run 537 - Standard nominal potentials and fields

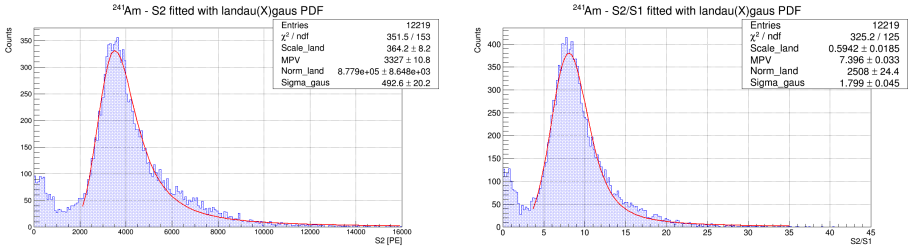

(b) run 544 - Potentials at cathode and first ring four times wrt run 537

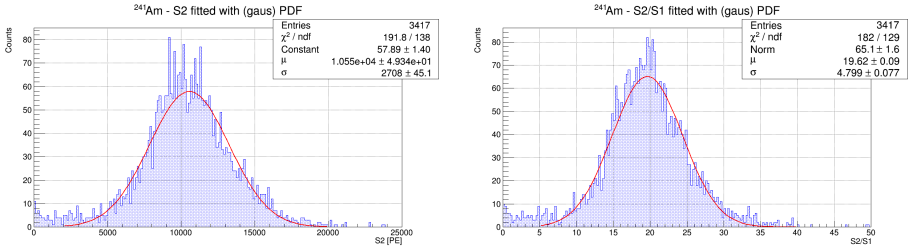

(c) run 554 - Potential at anode two times wrt run 537

Fig. 4.11: S2 and S2/S1 shape and S2 LY from ^{241}Am γ-source (59.5 keV). For potentials and nominal electric fields refers to Tab. 4.2. More in text.

Actually this was used here to evaluate S1 LY (sec. 4.1.3), as the bivariate one was not applicable because of a non Gaussian S2 shape (more later).

As said to evaluate S1 and S2 LY, up to now we used an ^{241}Am γ-source (59.5 keV). Figure 4.11 shows S2 (left) and S2/S1 (right) distributions at different potentials configurations. From top to bottom: data in run 537 were collected in "standard" configuration, data in run 544 were collected with potentials at cathode and first ring four times higher with respect to run 537 and data in run 554 were collected with potential at anode two times higher with respect to run 537 (potentials and nominal electric fields for different configurations are reported in Tab. 4.2). Same simple cuts have been applied on different data: events with only two signals; the first signal in S1 ER f_{prompt} distribution ($0.2 < f_{prompt} < 0.4$);

the second signal in S2 f_{prompt} distribution ($f_{prompt} < 0.2$); S1 energy near ^{241}Am γ energy ($45\,\text{keVee} < S1 < 75\,\text{keVee}$). As can be seen, S2 spectra shapes for data collected in "standard" configuration (run 537) and data from run 544 are far away to be Gaussian like, while are well fitted by a Landau PDF convoluted with a Gaussian distribution (to take into account various smearing sources). S2 spectra need also to be related to S2/S1 most probable values, which are only about 2.4 in "standard" configuration, and rise at only about 7.4 by multiplying by four cathode and first ring potentials.

Just for reference, in DarkSide-50 at standard nominal electric fields configuration (i.e. $E_{drift} = 200\,\text{V/cm}$, $E_{extr} = 2.8\,\text{kV/cm}$, $E_{elect} = 4.2\,\text{kV/cm}$), the same as in run 537, about $\text{S1} \simeq 300\,\text{PE}$ and $\text{S2} \simeq 8890\,\text{PE}$ respectively from ^{83m}Kr line (41.5 keVee) are achieved (see ref. [123] for more details), so that $\text{S2/S1} \sim 30$ (mean values). DarkSide-50 S2/S1 ratio is a benchmark, even if it must be taken into account that we didn't use ^{83m}Kr but ^{241}Am and N_{e^-} may vary with energy (but not so much from roughly 40 to 60 keVee), ReD TPC "diving bell" holds 0.7 cm-thick vapor layer (H_{elect}) instead of 1.0 cm-thick and the optical response is clearly different between the two detectors. By the way, one would expect even with ReD TPC an S2/S1 ratio not so far from DarkSide-50.

It seems like that in these configurations not all e^- surviving recombination are able to be collected at the anode, as if several e^- remained trapped at the liquid-vapor interface or at the grid. This can explain even S2 Gaussian spectra shape and the strong increase of the S2/S1 ratio, up to about 20, from data collected in the last listed configuration (run 554), where nominal E_{extr} and E_{elect} are instead only twice with respect to "standard" one. The relative increase of S2/S1 ratio, more than eight times with respect to that at standard fields

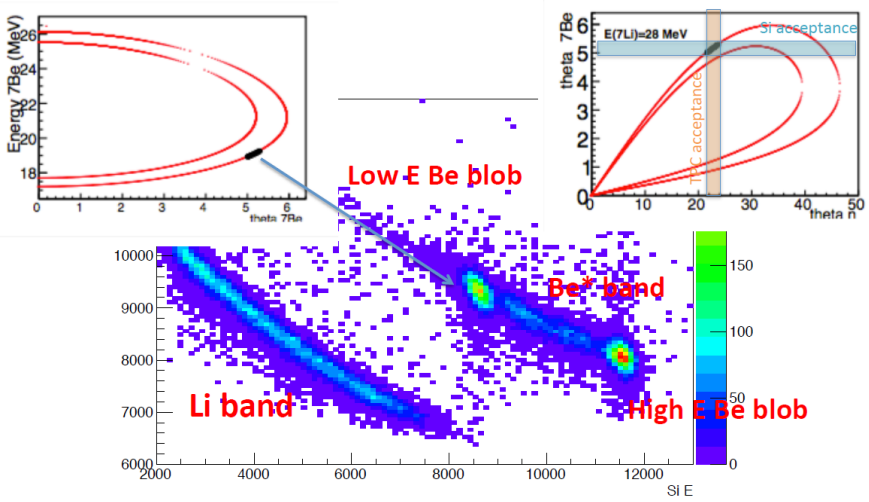

Fig. 4.12: $\Delta E/E$ scatter plot - data from run 526, 527, 528, 530, 531, 532, which correspond to approx 12.5 h livetime.

can't be explained only with secondary scintillation increase, which has a linear dependence with respect to E_{elect} (sec. 2.2.7). Only an increase on the number of electrons that reach the gas pocket can take in to account for a similar increase in S2/S1 ratio. Anyway, this unexpected behavior is still under investigation and these speculations are precisely only speculations.

4.2 Preliminary Results

In this section I present the analysis on data taken with LNS neutron beam in the "Si-telescope AND any PMT" trigger configuration. The trigger was based on $\Delta E/E$ Si telescope, with $\Delta E - E$ detectors in AND logic among them, and thresholds to collect only events in ^{7}Be *loci* plus part of the ^{7}Li band (Fig. 4.12). Signals from Si-telescope was in turn in AND logic with any LSci PMTs within 200 ns trigger window.

Data analyzed are from run 526, 527, 528, 530, 531, 532 (that have all been acquired in same conditions, during the last day of July beam-time). This correspond to approx 12.5 h livetime. The run configuration was: target $CH_2 = 244\ \mu g/cm^2$

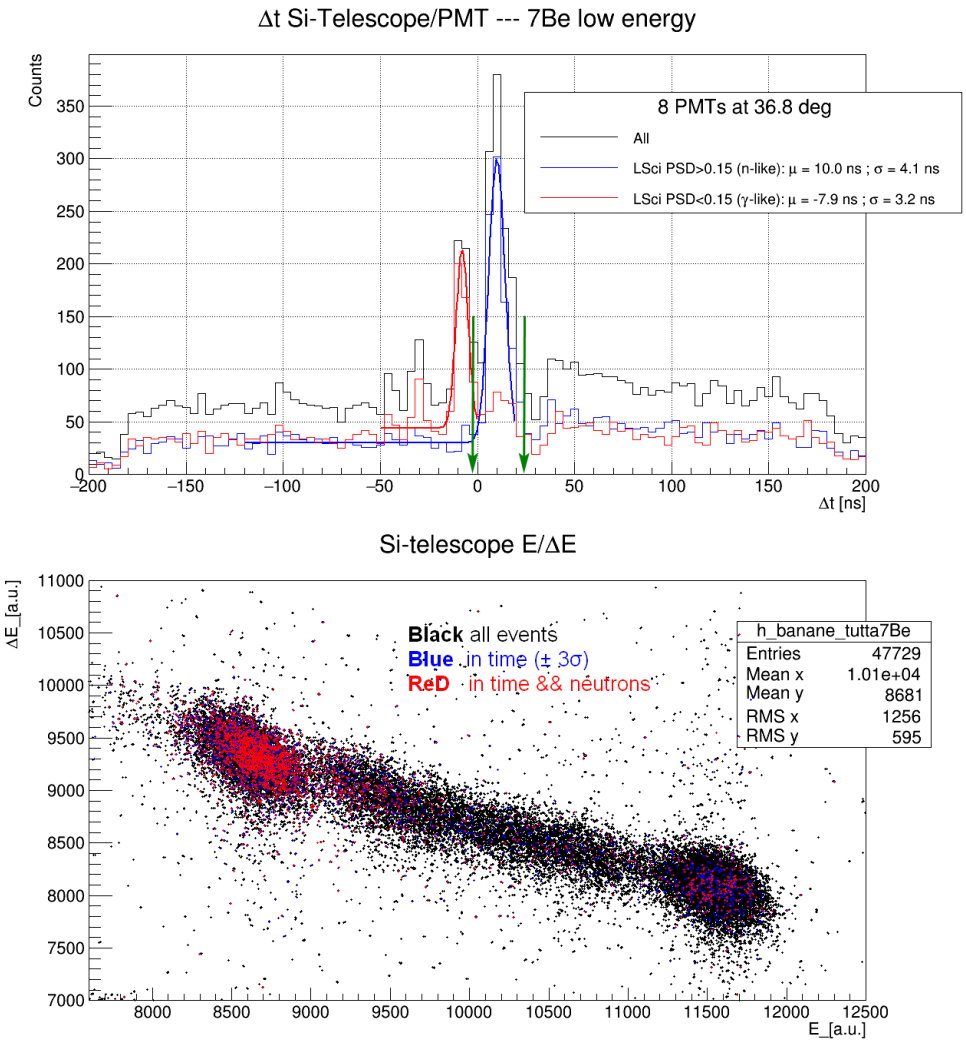

Fig. 4.13: Top Δt calculated as "LiSci start time" - "Si start time" for all eight $\text{LiSCis}_{1/8}$. Neutron-like events have Δt Si-PMT $\simeq 10$ ns. Green arrows point to time cuts for "triple" events selection. More in text. *Bottom* Events on $\Delta E/E$ scatter plot tagged by LiSci PSD and Δt Si-PMT.

and $E_{Beam} = 28$ MeV, so that neutron energy was about $E_n \simeq 7.4$ MeV. As said (sec. 3.6.1, eq. 3.8), at this neutron energy we expect, by kinematics, that the energy of nuclear scattering tagged by the eight $\text{LiSCis}_{1/8}$ was spread around 73 keV. The beam current measured in the Faraday cup during data taken was oscillating: $I_{beam} \in (1; 12)$ nA. The weighted average of I_{beam} calculated using the number of events for every run and the reported I_{beam} is about $\overline{I_{beam}} \simeq 6$ nA. This uncertainty on the beam current is the major obstacle to understand real

neutron rate on the TPC.

The LiSci PMT thresholds were roughly 20 keVee, while as said the TPC (in double-phase "standard" configuration) was in slave mode (also to look for very small recoil signals offline).

In Fig. 4.13 on top, Δt calculated as "LiSci start time" - "Si start time" for all eight $\text{LiSCis}_{1/8}$. Two time-correlated peaks are well distinguishable. The more populated peak has LiSci PSD > 0.15, which means that they are neutron-like events, while the other peak has LiSci PSD < 0.15, which means that they are γ-like events. The time difference of about 20 ns is consistent with γs from inelastic n/Ar scattering. On bottom, events on $\Delta E/E$ scatter plot tagged by LiSci PSD and by Δt Si-PMT.

In Fig. 4.14 Δt as "TPC start time" - "Si start time". Only events in low energy ^{7}Be *locus* and in NRs f_{700} band (i.e. $f_{700} \in (0.4; 0.7)$, see par. 4.1.3) are plotted. The time spectrum has two time-correlated peaks, one of which seems due to a misalignment of 2 trigger clock (8 ns/clock) in the two DAQ boards in which the 28 channels are collected. Under this explanation even these events are to be taken into account for "triple" events counting, as I do here below (green arrows in figures point to time cuts for "triple" events selection).

To select "triple" events, cuts on events collected are needed; below those here chose for this analysis:

- events in ^{7}Be low energy *locus* (to select the correct kinematically solution)
- events in all of 8 $\text{LiSCis}_{1/8}$
- energy in LiSCi > 10 keVee (to avoid events from pedestal)
- n-like events in LiSCi (i.e. LiSCi PSD > 0.15)

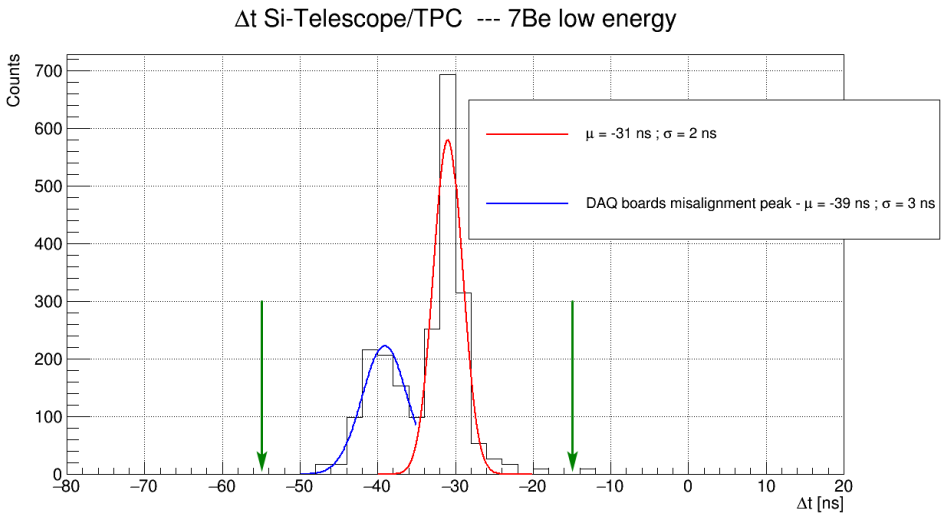

Fig. 4.14: Δt calculated as "TPC start time" - "Si start time". Peak at around -39 ns seems due to misalignment in DAQ boards. Green arrows point to time cuts for "triple" events selection. More in text.

- events with energy E_{TPC} deposed in the TPC so that $E_{TPC} \in (1; 200)$ KeVee (the energy range of interest)
- events in the TPC with only two pulses (to select events with presumably S1 and S2)
- events in the TPC with fist pulse in n-like band (i.e. $f_{700} \in (0.4; 0.7)$)
- events "in time" with respect to "LiSci start time" - "Si start time" (i.e. between green arrows in Fig. 4.13)
- events "in time" with respect to "TPC start time" - "Si start time" (i.e. between green arrows in Fig. 4.14).

Only 26 events survive cuts (on about 67k). Fig. 4.15 shows a Gauss plus Exp likelihood fit on the histogram of these cuts-survived events. Roughly speaking, considering a nuclear quenching factor of about 0.3 (see sec 2.2.3), the peak found is consistent with the expected ~ 70 keVnr nuclear energy recoil.

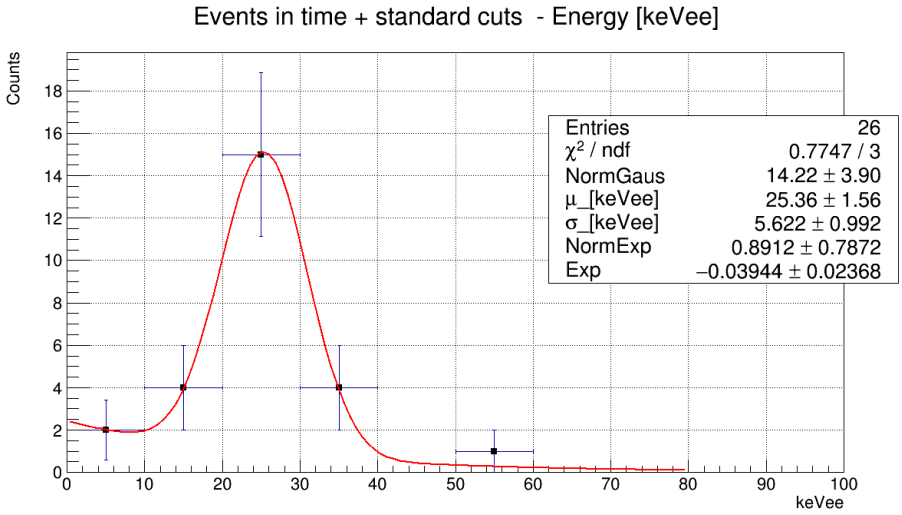

Fig. 4.15: Spectrum of events surviving the background rejection cuts (more in text). Considering a nuclear quenching factor around at 0.3, the peak found with a Gauss plus Exp likelihood is roughly consistent with the expected ~ 70 keVnr.

Even considering the 26 events all "triple" neutron scattering events and $I_{beam} = 1$ nA, for the "triple" rate we get (#events/(8 LiSCis)/(12.5 h)):

$$\frac{\Delta Events}{\Delta t}\Big|_{(\mathrm{PMT})} \leq 0.26\,\mathrm{cph}\Big|_{(1\mathrm{PMT};1\,\mathrm{nA};244\mu g/cm^2)} \tag{4.4}$$

about a factor ten less with respect to calculations (eq. 3.29) and MC simulations. A plausible motivation is a misalignment of the Si-telescope collimator (as said in sec. 3.2).

Even with the "correct" (i.e. predicted) rate, the experiment needs almost one week of data taken for every nuclear recoil energy point, to have a sufficient statistic. Therefore we need to solve this low rate problem to go on with the directional experiment. Anyway, the three detectors system is working and we are confident to have had identified the causes of rate failure, as also to fix them before 2019 beam-time data taken.

CONCLUSIONS

Within the DarkSide Program, the Recoil Directionality (ReD) experiment first aims to reveal directionality signature in nuclear recoils, in the energy range of the order of that one expected in WIMP-Ar scattering recoils. This signature would be a very highly desirable capability for a direct dark matter detection experiment, especially at the exposure, and beyond, at which the onset of ν-induced nuclear recoils has to be considered, as is the case of next DarkSide Program step, the DarkSide-20k experiment (see sec. 2.1).

In order to have a directional experiment with controlled recoil energy, it is necessary the use of low energy and as mono-energetic as possible neutrons in a closed kinematics approach. Moreover an optimized TPC-Cryogenic setup is necessary to avoid neutron multi scattering in Argon as in materials all around the TPC. To this aim, during last three years, different setup have been adopted and different neutron sources have been evaluated and used, as the DD neutron generator described in appendix. At last, ReD is now installed (and running at the moment of writing) at Laboratori Nazionali del Sud (LNS) in Catania, Italy, where neutrons are produced via $p(^7\mathrm{Li}, n)^7\mathrm{Be}$ reaction using their Tandem accelerator. In this thesis I decided to describe this final operating setup and ongoing results.

ReD is a complex experiment made by three detectors (the Si-telescope, the TPC and the n-spectrometer), more in the commissioning that in the data taking

phase (or better in the transition phase between the two phases), so results here reported are long away from being final ones (not only for the reduced measured “triple" rate with respect to predicted - see sec. 4.2). Furthermore in this work, among other things, I reported results on TPC characterization and calibration (and issues founded during this commissioning phase), taking in mind that ReD is also R&D for the DarkSide20k experiment (e.g. ReD double-phase TPC is the first one with only SiPMs as photomultipliers, with consequence e.g. on pulse shape discrimination parameter f_{prompt}, as reported in sec. 4.1.3).

Anyway, as here reported, some problems have arisen during the first data taking phase, in 2018, but now we are confident to have identified origins of these problems and we are now working to be ready to finally do the “directional measure" during next physical beam-times, in 2019.

APPENDIX

A. THE DD NEUTRON GUN

As neutron source at Naples we used a commercially available "Thermo Fischer Scientific" API-120 Deuteron-Deuteron (DD) generator [124]. The API-120 is a system that in standard configuration provides individually time- and direction-tagged, almost-monoenergetic continuous neutrons at very high intensity ($\sim 10^7$ n/s in 4π steradians), almost isotropically. Being the final destination of the DD-generator as calibration source for DarkSide Program detectors, the API-120 DD-generator at Naples is a custom version developed by "Thermo Fischer Scientific" with neutron flux limited to 10^4 n/s in 4π steradians, in order to meet the local approval by LNGS radiation safety regulations. The standard commercialized configuration was also modified to allow the device to fit through the DarkSide-50 source older. In Fig.A.1 on top a picture of DD-generator as arrived at Naples, on bottom a schematic DD-generator side view.

In the API-120 generator DD reaction neutrons are produced via the reaction

$$d + d \rightarrow n + {}^3\mathrm{He} \tag{A.1}$$

with an average energy of about 2.5 MeV . This reaction produces no penetrating radiation in coincidence with the neutrons. The tagging can be accomplished by detecting the ^{3}He from the neutron production reaction as it strikes an internal scintillator screen, using an external multi-anode MCP-PMT closely coupled

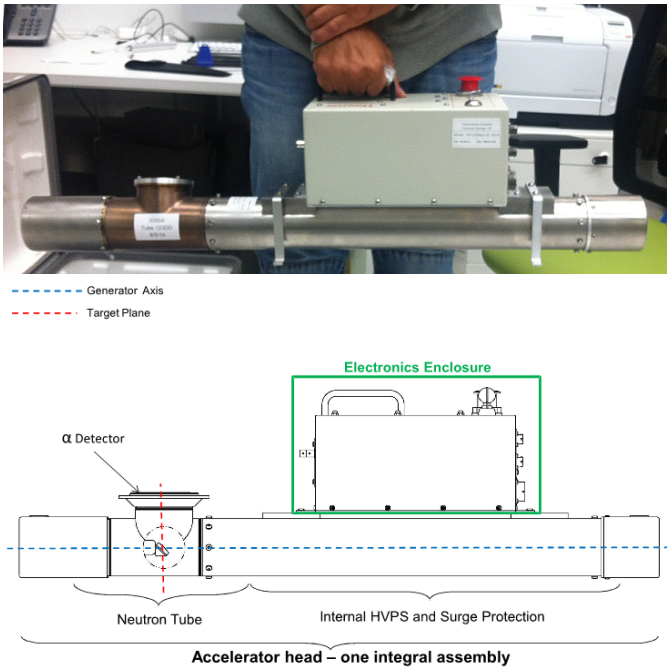

Fig. A.1: Top A picture of "Thermo Fischer Scientific" API-120 DD-generator as arrived at Naples. *Bottom* A schematic side view.

through a sapphire window. A complete description of the API-120 DD-generator can be found in ref. [125].

The generator was operated at deuteron energy of 50 keV and with deuterium beam current of 35 μA, the max setting value that have been setup by the factory to limit neutron flux to 10^4 n/s in 4π, as said.

For non-relativistic deuterons (up to $E_d \sim 20\,\mathrm{MeV}$), the energy of neutrons emitted in the $^2\mathrm{H}(d,n)^3\mathrm{He}$ reaction is given by:

$$E_n{}^{1/2} = \frac{(m_d m_n E_d)^{1/2}}{m_{^3\mathrm{He}} + m_n} \cos\varphi + \\ + \frac{\left\{m_d m_n E_d \cos^2\varphi + (m_{^3\mathrm{He}} + m_n)\left[m_{^3\mathrm{He}} Q + (m_{^3\mathrm{He}} - m_d) E_d\right]\right\}^{1/2}}{m_{^3\mathrm{He}} + m_n} \tag{A.2}$$

where m_d and $m_{^3\mathrm{He}}$ are the deuteron and ^{3}He nucleus masses, respectively, Q is the Q-value of the reaction, and φ is the neutron emission angle with respect

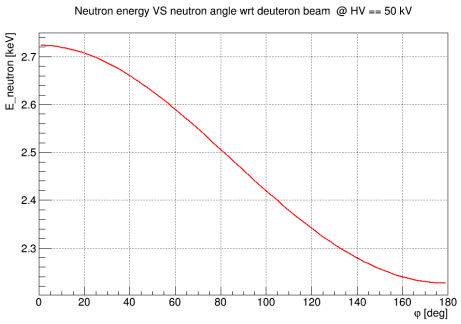

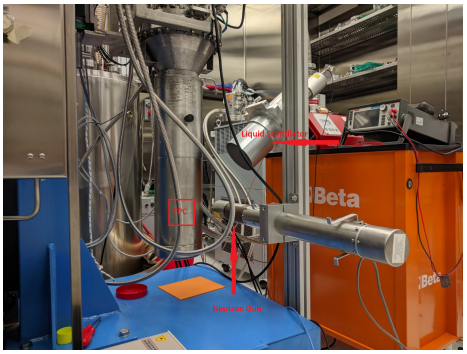

Fig. A.2: Left Energy of API-120 emitted neutrons vs neutron angle with respect to deuteron beam (or gun principal axis), for deuteron energy of 50 keV. *Right* The neutron generator during a data taken in the clean room of the Università degli Studi di Napoli Federico II, Physics Department "Ettore Pancini", Naples. You can see also the 5" liquid scintillator used to collect data and the dewar containing the LAr TPC.

to the deuteron beam. At small and large emission angles the neutron energy depends significantly on the deuteron energy. However, there is a minimum in both $\partial E_n/\partial\varphi$ and $\partial E_n/\partial E_d$ at $\varphi \sim 90°$, and consequently the energy spread of neutrons produced is minimal near this angle (see Fig. A.2 on the left). For this reason, during runs the neutron generator was operated in a configuration where deuterons are accelerated with a direction such that neutrons incident on LAr TPC are those produced at $\varphi = \frac{\pi}{2}$.

A.1 ReD with Neutron Gun: rough calculation of the magnitude of the expected events rate in the scintillators

IF:

- Y_{NG} := neutron yield in the Neutron Gun
  (==10^4 n/s in 4π – MAX!);
- D_{NG-TPC} := distance between Neutron Gun and TPC
  (==100 cm);
- $D_{TPC-SCI}$:= distance between TPC and SCIntillator

(==100 cm);

- S_{TPC} := surface of the vertical section of the TPC

  (with $h = 11.755$ cm and $d_{iameter} =$ 4.6 cm);

- S_{SCI} := surface of the scintillator face that " looks " the TPC

  (with $r_{adius} = \frac{1}{2} \cdot 3" = 3.81$ cm, if scintillator of 3");

- $S_{sphere(D_{NG-TPC})}$:= surface of the sphere with radius the distance between Neutron Gun and TPC;

- $S_{sphere(D_{TPC-SCI})}$:= surface of the sphere with radius the distance between TPC and SCIntillator;

- $P_{int(n-LAr)}$:= probability to have a useful interaction in a layer of LAr of 5 cm thick (roughly $\simeq 0.2$ from MC simulations);

- ϵ_{SCI} := scintillator/PMT global efficiency (roughly $\simeq 0.3$);

- R_{SCI} := neutron event rates in scintillator/PMT from Ar scattering;

THEN

$$R_{SCI} = Y_{NG} \cdot \frac{S_{TPC}}{S_{sphere(D_{NG-TPC})}} \cdot P_{int(n-LAr)} \cdot \frac{S_{SCI}}{S_{sphere(D_{TPC-SCI})}} \cdot \epsilon_{SCI}. \quad \text{(A.3)}$$

With the above values we get:

$$R_{SCI}(Y_{NG} == 10^4 \text{ n/s}) \simeq 10^{-4} \text{ n/s} \simeq 0.4 \text{ n/h}. \quad \text{(A.4)}$$

More generally:

$$R_{SCI}(Y_{NG}\text{whatever}) \simeq 10^{-8} \cdot Y_{NG}. \quad \text{(A.5)}$$

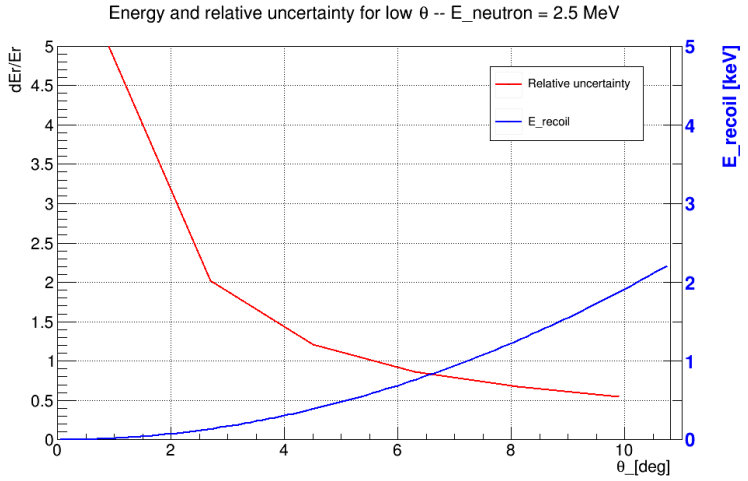

Fig. A.3: Relative recoil energy uncertainty and recoil energy for low neutron scattering angles and $E_n = 2.5\,\text{MeV}$. Compare this figure with Fig. 3.11 on the bottom, where values are shown for $E_n = 7\,\text{MeV}$, about standard neutron energy at LNS.

A.1.1 Low Energy recoil with DD Gun

As said a low energy recoil measurement - $E_R \sim 1\,\text{keV}$ - is in program. To reach this energy a very low scattering angle and ideally low neutron energy is required, which in LNS setup are $\theta_{LowEnergy} \simeq 4.3°$ and $E_n = 7\,\text{MeV}$, respectively. In Fig. A.3 relative uncertainty and E_R vs low θ values are shown for $E_n = 2.5\,\text{MeV}$. Compare this figure with Fig. 3.11 on the right, where relative uncertainty and E_R vs low θ values are shown for $E_n = 7\,\text{MeV}$, about "standard" neutron energy at LNS.

BIBLIOGRAPHY

[1] J. G. de Swart, G. Bertone, and J. van Dongen. "How dark matter came to matter". In: *Nature Astronomy* (2017). DOI: 10.1038/s41550-017-0059.

[2] Bernard Carr. "Baryonic Dark Matter". In: *Annual Review of Astronomy and Astrophysics* 32.1 (1994), pp. 531–590. DOI: 10.1146/annurev.aa.32.090194.002531.

[3] C. Alcock *et al.* "Experimental Limits on the Dark Matter Halo of the Galaxy from Gravitational Microlensing". In: *Phys. Rev. Lett.* 74 (15 1995), pp. 2867–2871. DOI: 10.1103/PhysRevLett.74.2867.

[4] Planck Collaboration. "Planck 2018 results. VI. Cosmological parameters". In: *Submitted to A&A* (2018). eprint: https://arxiv.org/pdf/1807.06209v1.pdf.

[5] M. Milgrom. "A modification of the Newtonian dynamics as a possible alternative to the hidden mass hypothesis". In: *Astrophys. J.* 270 (July 1983), pp. 365–370. DOI: 10.1086/161130.

[6] J. Zuntz *et al.* "Vector field models of modified gravity and the dark sector". In: *Phys. Rev. D* 81.10 (Feb. 2010), p. 104015. DOI: 10.1103/physrevd.81.104015. arXiv: 1002.0849.

[7] J. D. Lewin and P. F. Smith. "Review of mathematics, numerical factors, and corrections for dark matter experiments based on elastic nuclear re-

coil". In: *Astropart. Phys.* 6 (1996), pp. 87–112. DOI: 10.1016/S0927-6505(96)00047-3.

[8] F. Zwicky. "Die Rotverschiebung von extragalaktischen Nebeln". In: *Helvetica Physica Acta* 6 (1933), pp. 110–127.

[9] Vera C. Rubin and W. Kent Ford Jr. "Rotation of the Andromeda Nebula from a Spectroscopic Survey of Emission Regions". In: *Astrophys. J.* 159 (1970), pp. 379–403. DOI: 10.1086/150317.

[10] T. S. van Albada *et al.* "Distribution of dark matter in the spiral galaxy NGC 3198". In: *The Astrophysical Journal* 295 (Aug. 1985), pp. 305–313. DOI: 10.1086/163375.

[11] G. Bertone *et al. Particle Dark Matter: Observations, Models and Searches.* Cambridge Univ. Press, 2010. DOI: 10.1017/CBO9780511770739.

[12] W. Tucker *et al.* "1E 0657–56: A Contender for the Hottest Known Cluster of Galaxies". In: *The Astrophysical Journal Letters* 496.1 (1998), p. L5. URL: http://stacks.iop.org/1538-4357/496/i=1/a=L5.

[13] Douglas Clowe *et al.* "A Direct Empirical Proof of the Existence of Dark Matter". In: *The Astrophysical Journal Letters* 648.2 (2006), p. L109. URL: http://stacks.iop.org/1538-4357/648/i=2/a=L109.

[14] Edward W. Kolb and Michael S. Turner. *The Early Universe.* Reading, Massachusetts: Addison-Wesley, Feb. 1990. Chap. 9.

[15] George R. Blumenthal *et al.* "Formation of galaxies and large-scale structure with cold dark matter". In: *Nature* 311.5986 (Oct. 1984), pp. 517–525. DOI: 10.1038/311517a0.

[16] Volker Springel *et al.* "Simulations of the formation, evolution and clustering of galaxies and quasars". In: *Nature* 435.7042 (June 2005), pp. 629–636. ISSN: 0028-0836. DOI: 10.1038/nature03597. eprint: astro-ph/0504097.

[17] M. Vogelsberger *et al.* "Properties of galaxies reproduced by a hydrodynamic simulation". In: *Nature* 509.7499 (May 2014), pp. 177–182. DOI: 10.1038/nature13316. arXiv: 1405.1418.

[18] Pol Mollitor, Emmanuel Nezri, and Romain Teyssier. "Baryonic and dark matter distribution in cosmological simulations of spiral galaxies". In: (May 2014). arXiv: 1405.4318.

[19] David Tytler *et al.* "Review of Big Bang Nucleosynthesis and Primordial Abundances". In: *Physica Scripta* T85.1 (Jan. 2000), pp. 12+. DOI: 10.1238/physica.topical.085a00012. eprint: astro-ph/0001318.

[20] Brian Fields and Subir Sarkar. "Big-Bang nucleosynthesis (Particle Data Group mini-review)". In: *J. Phys. G.* 33.1 (Oct. 2006), pp. 1–1232. ISSN: 0954-3899. DOI: 10.1088/0954-3899/33/1/001. eprint: astro-ph/0601514.

[21] Michele Maggiore. "Gravitational Wave Experiments and Early Universe Cosmology". In: *Phys. Rep.* 331.6 (Feb. 2000), pp. 283–367. ISSN: 03701573. DOI: 10.1016/s0370-1573(99)00102-7. eprint: gr-qc/9909001.

[22] Richard H. Cyburt *et al.* "New BBN limits on Physics Beyond the Standard Model from He4". In: *J. Astropart. Phys.* 23.3 (Aug. 2005), pp. 313–323. DOI: 10.1016/j.astropartphys.2005.01.005. eprint: astro-ph/0408033.

[23] Karsten Jedamzik. "Big Bang Nucleosynthesis Constraints on Hadronically and Electromagnetically Decaying Relic Neutral Particles". In: *Phys. Rev. D* 74.10 (Nov. 2006), p. 103509. ISSN: 1550-7998. DOI: 10.1103/physrevd.74.103509. eprint: hep-ph/0604251.

[24] Mark W. Goodman and Edward Witten. "Detectability of certain dark-matter candidates". In: *Phys. Rev. D* 31.12 (June 1985), pp. 3059–3063. ISSN: 0556-2821. DOI: 10.1103/PhysRevD.31.3059.

[25] Andrzej K. Drukier, Katherine Freese, and David N. Spergel. "Detecting cold dark-matter candidates". In: *Phys. Rev. D* 33.12 (June 1986), pp. 3495–3508. DOI: 10.1103/PhysRevD.33.3495.

[26] P. Agnes *et al.* "Constraints on Sub-GeV Dark-Matter–Electron Scattering from the DarkSide-50 Experiment". In: *Phys. Rev. Lett.* 121 (11 2018), p. 111303. DOI: 10.1103/PhysRevLett.121.111303. URL: https://link.aps.org/doi/10.1103/PhysRevLett.121.111303.

[27] Teresa Marrodan Undagoitia and Ludwig Rauch. "Dark matter direct-detection experiments". In: *Journal of Physics G: Nuclear and Particle Physics* 43 (Sept. 2015).

[28] J I Read. "The local dark matter density". In: *Journal of Physics G: Nuclear and Particle Physics* 41.6 (2014), p. 063101. URL: http://stacks.iop.org/0954-3899/41/i=6/a=063101.

[29] Anne M Green. "Astrophysical uncertainties on the local dark matter distribution and direct detection experiments". In: *Journal of Physics G: Nuclear and Particle Physics* 44.8 (2017), p. 084001. URL: http://stacks.iop.org/0954-3899/44/i=8/a=084001.

[30] F. J. Kerr and Donald Lynden-Bell. "Review of galactic constants". In: *Mon. Not. Roy. Astron. Soc.* 221 (1986), p. 1023.

[31] Anne M. Green. "Astrophysical uncertainties on direct detection experiments". In: *Mod. Phys. Lett.* A27 (2012), p. 1230004. DOI: 10.1142/S0217732312300042. arXiv: 1112.0524 [astro-ph.CO].

[32] Martin C. Smith *et al.* "The RAVE Survey: Constraining the Local Galactic Escape Speed". In: *Mon. Not. Roy. Astron. Soc.* 379 (2007), pp. 755–772. DOI: 10.1111/j.1365-2966.2007.11964.x. arXiv: astro-ph/0611671 [astro-ph].

[33] Christopher Savage, Katherine Freese, and Paolo Gondolo. "Annual Modulation of Dark Matter in the Presence of Streams". In: *Phys. Rev.* D74 (2006), p. 043531. DOI: 10.1103/PhysRevD.74.043531. arXiv: astro-ph/0607121 [astro-ph].

[34] Carlos E. Yaguna. "Isospin-violating dark matter in the light of recent data". In: *Phys. Rev. D* 95 (5 2017), p. 055015. DOI: 10.1103/PhysRevD.95.055015. URL: https://link.aps.org/doi/10.1103/PhysRevD.95.055015.

[35] V. Chepel and H. Araujo. "Liquid noble gas detectors for low energy particle physics". In: *JINST* 8 (2013), R04001. DOI: 10.1088/1748-0221/8/04/R04001. arXiv: 1207.2292 [physics.ins-det].

[36] A. K. Drukier, Katherine Freese, and D. N. Spergel. "Detecting Cold Dark Matter Candidates". In: *Phys. Rev.* D33 (1986), pp. 3495–3508. DOI: 10.1103/PhysRevD.33.3495.

[37] Katherine Freese, Mariangela Lisanti, and Christopher Savage. *Colloquium: Annual modulation of dark matter*. Vol. 85. 4. American Physical Society, 2013, pp. 1561–1581. DOI: 10.1103/RevModPhys.85.1561. URL: http://link.aps.org/doi/10.1103/RevModPhys.85.1561.

[38] R. Bernabei *et al.* "The DAMA/LIBRA apparatus". In: *Nucl. Instrum. Meth.* A592 (2008), pp. 297–315. DOI: 10.1016/j.nima.2008.04.082. arXiv: 0804.2738 [astro-ph].

[39] R. Bernabei *et. al.* "First model independent results from DAMA/LIBRA-phase2". In: arXiv:1805.10486v1 [hep-ex] (May 2018). URL: https://arxiv.org/abs/1805.10486v1.

[40] David N. Spergel. "Motion of the Earth and the detection of weakly interacting massive particles". In: *Phys. Rev. D* 37 (6 1988), pp. 1353–1355. DOI: 10.1103/PhysRevD.37.1353. URL: https://link.aps.org/doi/10.1103/PhysRevD.37.1353.

[41] D. P. Snowden-Ifft, C. J. Martoff, and J. M. Burwell. "Low pressure negative ion time projection chamber for dark matter search". In: *Phys. Rev. D* 61 (10 2000), p. 101301. DOI: 10.1103/PhysRevD.61.101301. URL: https://link.aps.org/doi/10.1103/PhysRevD.61.101301.

[42] Daniel Z. Freedman. "Coherent neutrino nucleus scattering as a probe of the weak neutral current". In: *Phys. Rev.* D9 (1974), pp. 1389–1392. DOI: 10.1103/PhysRevD.9.1389.

[43] Blas Cabrera, Lawrence M. Krauss, and Frank Wilczek. "Bolometric Detection of Neutrinos". In: *Phys. Rev. Lett.* 55 (1985), p. 25. DOI: 10.1103/PhysRevLett.55.25.

[44] J. Billard, L. Strigari, and E. Figueroa-Feliciano. "Implication of neutrino backgrounds on the reach of next generation dark matter direct detection experiments". In: *Phys. Rev.* D89.2 (2014), p. 023524. DOI: 10.1103/PhysRevD.89.023524. arXiv: 1307.5458 [hep-ph].

[45] R. Bernabei *et al.* "Final model independent result of DAMA/LIBRA-phase1". In: *Eur. Phys. J.* C73 (2013), p. 2648. DOI: 10.1140/epjc/s10052-013-2648-7. arXiv: 1308.5109 [astro-ph.GA].

[46] S. C. Kim *et al.* "New Limits on Interactions between Weakly Interacting Massive Particles and Nucleons Obtained with CsI(Tl) Crystal Detectors". In: *Phys. Rev. Lett.* 108 (2012), p. 181301. DOI: 10.1103/PhysRevLett.108.181301. arXiv: 1204.2646 [astro-ph.CO].

[47] B. Ahmed *et al.* "The NAIAD experiment for WIMP searches at Boulby mine and recent results". In: *Astropart. Phys.* 19 (2003), pp. 691–702. DOI: 10.1016/S0927-6505(03)00115-4. arXiv: hep-ex/0301039 [hep-ex].

[48] C. E. Aalseth *et al.* "DarkSide-20k: A 20 tonne two-phase LAr TPC for direct dark matter detection at LNGS". In: *Eur. Phys. J. Plus* 133.3 (2018), p. 131. DOI: 10.1140/epjp/i2018-11973-4. URL: https://doi.org/10.1140/epjp/i2018-11973-4.

[49] Z. Ahmed *et al.* "Dark Matter Search Results from the CDMS II Experiment". In: *Science* 327 (2010), pp. 1619–1621. DOI: 10.1126/science.1186112. arXiv: 0912.3592 [astro-ph.CO].

[50] G. Angloher *et al.* "Results from 730 kg days of the CRESST-II Dark Matter Search". In: *Eur. Phys. J.* C72 (2012), p. 1971. DOI: 10.1140/epjc/s10052-012-1971-8. arXiv: 1109.0702 [astro-ph.CO].

[51] C. E. Aalseth *et al.* "CoGeNT: A Search for Low-Mass Dark Matter using p-type Point Contact Germanium Detectors". In: *Phys. Rev.* D88 (2013), p. 012002. DOI: 10.1103/PhysRevD.88.012002. arXiv: 1208.5737 [astro-ph.CO].

[52] C. E. Aalseth *et al.* "Search for An Annual Modulation in Three Years of CoGeNT Dark Matter Detector Data". In: (2014). arXiv: 1401.3295 [astro-ph.CO].

[53] E. Armengaud *et al.* "Performance of the EDELWEISS-III experiment for direct dark matter searches". In: *JINST* 12.08 (2017), P08010. DOI: 10.1088/1748-0221/12/08/P08010. arXiv: 1706.01070 [physics.ins-det].

[54] E. Aprile *et al.* "The XENON1T Dark Matter Experiment". In: (2017). arXiv: 1708.07051 [astro-ph.IM].

[55] Daniel S Akerib *et al. First Results from the LUX Dark Matter Experiment at the Sanford Underground Research Facility.* Vol. 112. 9. 2014, p. 091303. DOI: 10.1103/PhysRevLett.112.091303. URL: http://link.aps.org/doi/10.1103/PhysRevLett.112.091303.

[56] Xiangyi Cui *et al.* "Dark Matter Results From 54-Ton-Day Exposure of PandaX-II Experiment". In: (2017). arXiv: 1708.06917 [astro-ph.CO].

[57] P. Benetti *et al.* "First results from a Dark Matter search with liquid Argon at 87 K in the Gran Sasso Underground Laboratory". In: *Astropart. Phys.* 28 (2008), pp. 495–507. DOI: 10.1016/j.astropartphys.2007.08.002. arXiv: astro-ph/0701286 [astro-ph].

[58] E. Behnke *et al.* "First Dark Matter Search Results from a 4-kg CF_3I Bubble Chamber Operated in a Deep Underground Site". In: *Phys. Rev.* D86.5 (2012). [Erratum: Phys. Rev.D90,no.7,079902(2014)], p. 052001. DOI: 10.

1103/PhysRevD.86.052001, 10.1103/PhysRevD.90.079902. arXiv: 1204.3094 [astro-ph.CO].

[59] M. Felizardo *et al.* "The SIMPLE Phase II Dark Matter Search". In: *Phys. Rev.* D89.7 (2014), p. 072013. DOI: 10.1103/PhysRevD.89.072013. arXiv: 1404.4309 [hep-ph].

[60] S. Archambault *et al.* "Constraints on Low-Mass WIMP Interactions on ^{19}F from PICASSO". In: *Phys. Lett.* B711 (2012), pp. 153–161. DOI: 10.1016/j.physletb.2012.03.078. arXiv: 1202.1240 [hep-ex].

[61] George Jaffé. *Zur Theorie der Ionisation in Kolonnen. II.* Vol. 393. 7. WILEY-VCH Verlag, 1929, pp. 977–1008. DOI: 10.1002/andp.19293930706. URL: http://doi.wiley.com/10.1002/andp.19293930706.

[62] G. Bellini *et al.* "Cosmogenic Backgrounds in Borexino at 3800 m water-equivalent depth". In: *Journal of Cosmology and Astroparticle Physics* 2013.08 (2013), p. 049. URL: http://stacks.iop.org/1475-7516/2013/i=08/a=049.

[63] T. Alexander *et al.* "Light Yield in DarkSide-10: A Prototype Two-Phase Argon TPC for Dark Matter Searches". In: *Astropart. Phys.* 49 (2013), pp. 44–51. DOI: 10.1016/j.astropartphys.2013.08.004. arXiv: 1204.6218 [astro-ph.IM].

[64] P. Agnes *et al.* "First results from the DarkSide-50 dark matter experiment at Laboratori Nazionali del Gran Sasso". In: *Physics Letters B* 743 (2015), pp. 456 –466. ISSN: 0370-2693. DOI: https://doi.org/10.1016/j.physletb.2015.03.012. URL: http://www.sciencedirect.com/science/article/pii/S0370269315001756.

[65] P. Agnes *et al.* "DarkSide-50 532-day Dark Matter Search with Low-Radioactivity Argon". In: (2018). arXiv: 1802.07198 [astro-ph.CO].

[66] Matteo Cadeddu. "DarkSide-20k sensitivity, directional dark matter detection and the role of coherent elastic neutrino-nucleus scattering background". In: *PhD thesis - University of Cagliari* (Mar. 2018).

[67] J. Billard. "Comparing readout strategies to directly detect dark matter". In: *Phys. Rev. D* 91 (2 2015), p. 023513. DOI: 10.1103/PhysRevD.91.023513. URL: https://link.aps.org/doi/10.1103/PhysRevD.91.023513.

[68] Jingke Xu. "Study of Argon from Underground Sources for Direct Dark Matter Detection". In: *PhD thesis - Princeton University* (Jan. 2013). URL: http://inspirehep.net/record/1466658.

[69] Authur A Maryott and Edgar R Smith. "Table of dielectric constants of pure liquids". In: *National Bureau of Standards* Circular 514 (1951). URL: http://www.dtic.mil/dtic/tr/fulltext/u2/a278956.pdf.

[70] E Aprile *et al. Noble Gas Detectors*. Dec. 2006, pp. 1–345.

[71] Shinzou Kubota *et al.* "Dynamical behavior of free electrons in the recombination process in liquid argon, krypton, and xenon". In: *Phys. Rev. B* 20 (8 1979), pp. 3486–3496. DOI: 10.1103/PhysRevB.20.3486. URL: https://link.aps.org/doi/10.1103/PhysRevB.20.3486.

[72] Akira Hitachi *et al.* "Effect of ionization density on the time dependence of luminescence from liquid argon and xenon". In: *Phys. Rev. B* 27 (9 1983), pp. 5279–5285. DOI: 10.1103/PhysRevB.27.5279. URL: https://link.aps.org/doi/10.1103/PhysRevB.27.5279.

[73] M. Wojcik. "Electron recombination in low-energy nuclear recoils tracks in liquid argon". In: *Journal of Instrumentation* 11.02 (2016), P02005. URL: http://stacks.iop.org/1748-0221/11/i=02/a=P02005.

[74] R. M. Woods and B. J. Spence. "The Infrared Spectrum of Argon". In: *Phys. Rev.* 45 (10 1934), pp. 669–670. DOI: 10.1103/PhysRev.45.669. URL: https://link.aps.org/doi/10.1103/PhysRev.45.669.

[75] Tadayoshi Doke *et al.* "Absolute Scintillation Yields in Liquid Argon and Xenon for Various Particles". In: *Japanese Journal of Applied Physics* 41.3R (2002), p. 1538. URL: http://stacks.iop.org/1347-4065/41/i=3R/a=1538.

[76] P. Moutard *et al.* "Pressure effects on kinetics and decay processes in argon under selective photoexcitation". In: *The Journal of Chemical Physics* 87.8 (1987), pp. 4576–4588. DOI: 10.1063/1.452869. eprint: https://doi.org/10.1063/1.452869. URL: https://doi.org/10.1063/1.452869.

[77] W. Krötz *et al.* "Third excimer continuum of argon excited by a heavy-ion beam". In: *Phys. Rev. A* 43 (11 1991), pp. 6089–6094. DOI: 10.1103/PhysRevA.43.6089. URL: https://link.aps.org/doi/10.1103/PhysRevA.43.6089.

[78] Mark G Boulay and Andrew Hime. "Technique for direct detection of weakly interacting massive particles using scintillation time discrimination in liquid argon". In: *Astropart. Phys.* 25.3 (2006), pp. 179–182. DOI: 10.1016/j.astropartphys.2005.12.009. URL: http://linkinghub.elsevier.com/retrieve/pii/S0927650505001830.

[79] W. H. Lippincott *et al.* "Scintillation time dependence and pulse shape discrimination in liquid argon". In: *Phys. Rev. C* 78 (3 2008), p. 035801. DOI: 10.1103/PhysRevC.78.035801. URL: https://link.aps.org/doi/10.1103/PhysRevC.78.035801.

[80] Claudio Savarese. "A novel light detector for DarkSide-20k". In: *PhD thesis - Gran Sasso Science Institute (GSSI)* (2017).

[81] Paolo Agnes *et al.* "Results from the first use of low radioactivity argon in a dark matter search". In: *Phys. Rev. D* 93.8 (2016), p. 081101. DOI: 10.1103/PhysRevD.93.081101. URL: http://link.aps.org/doi/10.1103/PhysRevD.93.081101.

[82] T. Alexander *et al. Observation of the dependence on drift field of scintillation from nuclear recoils in liquid argon.* Vol. 88. American Physical Society, 2013, p. 092006. DOI: 10.1103/PhysRevD.88.092006. URL: https://link.aps.org/doi/10.1103/PhysRevD.88.092006.

[83] E. Segreto *et al.* "Delayed light emission of Tetraphenyl-butadiene excited by liquid argon scintillation light. Current status and future plans". In: *Journal of Instrumentation* 11.02 (2016), p. C02010. URL: http://stacks.iop.org/1748-0221/11/i=02/a=C02010.

[84] P. Agnes *et al.* "The electronics, trigger and data acquisition system for the liquid argon time projection chamber of the DarkSide-50 search for dark matter". In: *Journal of Instrumentation* 12.12 (2017), P12011. URL: http://stacks.iop.org/1748-0221/12/i=12/a=P12011.

[85] Huajie Cao *et al. Measurement of scintillation and ionization yield and scintillation pulse shape from nuclear recoils in liquid argon.* Vol. 91. 9.

2015, p. 092007. DOI: 10.1103/PhysRevD.91.092007. URL: http://link.aps.org/doi/10.1103/PhysRevD.91.092007.

[86] D.-M. Mei *et al.* "A model of nuclear recoil scintillation efficiency in noble liquids". In: *Astroparticle Physics* 30.1 (2008), pp. 12 –17. ISSN: 0927-6505. DOI: https://doi.org/10.1016/j.astropartphys.2008.06.001. URL: http://www.sciencedirect.com/science/article/pii/S0927650508000765.

[87] Lindhard J. and Scharff M. In: *Phys. Rev.* 124 (1961), p. 128.

[88] J B Birks and F A Black. "Deterioration of Anthracene under α-Particle Irradiation". In: *Proceedings of the Physical Society. Section A* 64.5 (1951), p. 511. URL: http://stacks.iop.org/0370-1298/64/i=5/a=112.

[89] P. Agnes *et al.* "Low-Mass Dark Matter Search with the DarkSide-50 Experiment". In: *Phys. Rev. Lett.* 121 (8 2018), p. 081307. DOI: 10.1103/PhysRevLett.121.081307. URL: https://link.aps.org/doi/10.1103/PhysRevLett.121.081307.

[90] J. Ziegler. *Stopping and Range of Ions in Matter*. 2013. URL: www.srim.org.

[91] V. Cataudella *et al.* "Directional modulation of electron-ion pairs recombination in liquid argon". In: *JINST* 12.12 (2017), P12002. DOI: 10.1088/1748-0221/12/12/P12002.

[92] R. Acciarri *et al.* "A study of electron recombination using highly ionizing particles in the ArgoNeuT Liquid Argon TPC". In: *JINST* 8 (2013), P08005. DOI: 10.1088/1748-0221/8/08/P08005. arXiv: 1306.1712 [physics.ins-det].

[93] D R Nygren. "Columnar recombination: a tool for nuclear recoil directional sensitivity in a xenon-based direct detection WIMP search". In: *Journal of Physics: Conference Series* 460.1 (2013), p. 012006. URL: http://stacks.iop.org/1742-6596/460/i=1/a=012006.

[94] D W Swan. "Ionization of liquid argon by α particles". In: *Proceedings of the Physical Society* 85.6 (1965), p. 1297. URL: http://stacks.iop.org/0370-1328/85/i=6/a=328.

[95] R Acciarri *et al.* "A study of electron recombination using highly ionizing particles in the ArgoNeuT Liquid Argon TPC". In: *Journal of Instrumentation* 8.08 (2013), P08005. URL: http://stacks.iop.org/1748-0221/8/i=08/a=P08005.

[96] G. W. Hutchinson. "Ionization in Liquid and Solid Argon". In: *Nature* 162 (1942), pp. 610–611. DOI: 10.1038/162610a0. URL: http://dx.doi.org/10.1038/162610a0.

[97] A.I. Bolozdynya. "Two-phase emission detectors and their applications". In: *Nuclear Instruments and Methods in Physics Research Section A: Accelerators, Spectrometers, Detectors and Associated Equipment* 422.1 (1999), pp. 314 –320. ISSN: 0168-9002. DOI: https://doi.org/10.1016/S0168-9002(98)00965-6. URL: http://www.sciencedirect.com/science/article/pii/S0168900298009656.

[98] A. A. Kruglov E. M. Gushchin and I. M. Obodovskii. "Emission of "hot" electrons from liquid and solid argon and xenon". In: *Sov. Phys. JETP* 55.5 (1982), pp. 860–862. URL: http://www.jetp.ac.ru/cgi-bin/dn/e_055_05_0860.pdf.

[99] A.F. Borghesani *et al.* "Electron transmission through the Ar liquid-vapor interface". In: *Physics Letters A* 149.9 (1990), pp. 481 –484. ISSN: 0375-9601. DOI: https://doi.org/10.1016/0375-9601(90)90221-9. URL: http://www.sciencedirect.com/science/article/pii/0375960190902219.

[100] C. A. N. Conde, L. R. Ferreira, and M. F. A. Ferreira. "The Secondary Scintillation Output of Xenon in a Uniform Field Gas Proportional Scintillation Counter". In: *IEEE Transactions on Nuclear Science* 24.1 (1977), pp. 221–224. ISSN: 0018-9499. DOI: 10.1109/TNS.1977.4328674.

[101] C.M.B. Monteiro *et al.* "Secondary scintillation yield in pure argon". In: *Physics Letters B* 668.3 (2008), pp. 167 –170. ISSN: 0370-2693. DOI: https://doi.org/10.1016/j.physletb.2008.08.030. URL: http://www.sciencedirect.com/science/article/pii/S0370269308010435.

[102] U.S Department of Commerce. *National Institute of Standard and Technology*. URL: https://www.nist.gov/.

[103] Alden Fan. "Results from the DarkSide-50 Dark Matter Experiment". In: *PhD thesis - University of California (UCLA)* (Jan. 2016). DOI: 10.2172/1341802.

[104] R. Acciarri *et al.* "Liquid argon dielectric breakdown studies with the MicroBooNE purification system". In: *Journal of Instrumentation* 9.11 (2014), P11001. URL: http://stacks.iop.org/1748-0221/9/i=11/a=P11001.

[105] M. Lebois *et al.* "Development of a kinematically focused neutron source with the $p(^7\mathrm{Li}, n)^7\mathrm{Be}$ inverse reaction". In: *Nuclear Instruments and Methods in Physics Research Section A: Accelerators, Spectrometers, Detectors and Associated Equipment* 735 (2014), pp. 145 –151. ISSN: 0168-9002. DOI:

https://doi.org/10.1016/j.nima.2013.07.061. URL: http://www.sciencedirect.com/science/article/pii/S0168900213010735.

[106] *ORTEC Technologies*. URL: https://www.ortec-online.com/products/radiation-detectors/silicon-charged-particle-radiation-detectors.

[107] *Fondazione Bruno Kessler*. URL: https://www.fbk.eu/en/.

[108] M. D'Incecco *et al.* "Development of a Very Low-Noise Cryogenic Preamplifier for Large-Area SiPM Devices". In: *IEEE Transactions on Nuclear Science* 65.4 (2018), pp. 1005–1011. ISSN: 0018-9499. DOI: 10.1109/TNS.2018.2799325.

[109] *Criotec impianti S.p.A.* URL: https://www.criotec.com/.

[110] *Cryomech, Inc.* URL: http://www.cryomech.com/.

[111] *SAES Getters S.p.A.* URL: www.saesgetters.com.

[112] *CAEN S.p.A.* URL: http://www.caen.it/.

[113] *Padme Collaboration DAQ*. URL: https://github.com/PADME-Experiment/padme-fw/wiki.

[114] *ROOT - An Object Oriented Data Analysis Framework*. URL: https://root.cern.ch/.

[115] M Drosg. "The $^{1}H(^{7}\mathrm{Li}, \mathrm{n})^{7}\mathrm{Be}$ Reaction as a Neutron Source in the MeV Range". In: *Technical Report* Los Alamos National Laboratory (1981). URL: https://inis.iaea.org/collection/NCLCollectionStore/_Public/12/640/12640448.pdf.

[116] *Evaluated Nuclear Data File*. 2018. URL: http://www.nndc.bnl.gov/exfor/endf00.jsp (visited on 09/08/2018).

[117] F. Pino *et al.* "The light output and the detection efficiency of the liquid scintillator EJ-309". In: *Applied Radiation and Isotopes* 89 (2014), pp. 79 –84. ISSN: 0969-8043. DOI: https://doi.org/10.1016/j.apradiso.2014.02.016. URL: http://www.sciencedirect.com/science/article/pii/S0969804314000682.

[118] Valerio Di Cicco. "Studio e calibrazione dello spettrometro per neutroni dell'esperimento ReD per lo studio di scattering di neutroni su argon liquido". MA thesis. Master Thesis - Università "La Sapienza" - Roma, 2017.

[119] *COMSOL Multhiphysics by COMSOL INC.* URL: https://www.comsol.com/.

[120] *Hamamatsu Photonics K.K.* URL: https://www.hamamatsu.com/jp/en/index.html.

[121] W. H. Lippincott *et al.* "Calibration of liquid argon and neon detectors with $^{83}Kr^{m}$". In: *Phys. Rev. C* 81 (4 2010), p. 045803. DOI: 10.1103/PhysRevC.81.045803. URL: https://link.aps.org/doi/10.1103/PhysRevC.81.045803.

[122] *LAr @ Brookhaven National Laboratory.* URL: https://lar.bnl.gov/properties/.

[123] Luca Pagani. "Direct dark matter detection with the DarkSide-50 experiment". In: *PhD thesis - University of Genova* (Apr. 2017).

[124] *Thermo Fischer Scientific S.p.A.* URL: https://www.thermofisher.com/order/catalog/product/151762A.

[125] D.L. Chichester, M. Lemchak, and J.D. Simpson. "The API 120: A portable neutron generator for the associated particle technique". In: *Nuclear Instru-*

ments and Methods in Physics Research Section B: Beam Interactions with Materials and Atoms 241.1 (2005). The Application of Accelerators in Research and Industry, pp. 753 –758. ISSN: 0168-583X. DOI: https://doi.org/10.1016/j.nimb.2005.07.128. URL: http://www.sciencedirect.com/science/article/pii/S0168583X05013170.

[126] *Berthold Technologies GmbH & Co. KG.* URL: https://www.berthold.com/en/neutron-probe-lb-6411.